

# POLITECNICO DI TORINO

Master's Degree in Aerospace Engineering



Master's Degree Thesis

## Plug-and-Play in Orbit: A Practical Radiation Hardness Assurance Framework for New Space Servicing Missions

Supervisors

Prof. Fabrizio STESINA

Ing. Luca MALVASIO

Ing. Simone RIPANDELLI

Candidate

VINCENZO CICERO

July 2025

## Abstract

In the context of the rapidly evolving New Space economy, this thesis was developed in collaboration with Kurs Orbital, a startup whose mission is to develop a modular, plug-and-play payload for servicing satellites through proximity operations and autonomous capture. The payload, known as ARCap, integrates robotic manipulators and a suite of relative navigation sensors, including vision-based and radar technologies, relying heavily on commercial off-the-shelf (COTS) and automotive-grade components. This approach promises faster development cycles and cost-efficiency, drastically reduces cost and development time, but introduces critical vulnerabilities with respect to radiation.

The goal of this work is to define and consolidate a structured, end-to-end framework for Radiation Hardness Assurance (RHA) specifically tailored to COTS-based architectures. From first principles of particle-matter interaction to the modeling of complex space radiation environments and from the analysis of degradation mechanisms (TID, SEE, DDD) to the selection of test methods and qualification thresholds, the thesis constructs a unified body of knowledge aimed at guiding future component choices and system-level risk assessments within the company. Inspired by the "Careful COTS" methodology, the thesis proposes a pragmatic RHA flow that integrates radiation environment modeling, component selection, radiation testing and system-level mitigation strategies.

This thesis combines those insights with ECSS-compliant RHA processes, including environment definition (ECSS-E-ST-10-04), dose and LET spectrum modeling (via SHIELDOSE and CREME) and radiation test planning (e.g., Co-60, X-rays screening).

Ultimately, this thesis demonstrates that with a disciplined, evidence-driven approach, COTS technologies can be effectively harnessed to deliver high-performance, radiation-tolerant space systems. ARCap becomes a case study for how the agility and innovation of the terrestrial tech sector, particularly automotive and industrial electronics, can be safely and systematically transferred into the domain of orbital robotics, unlocking new paradigms for satellite servicing, debris removal and on-orbit autonomy.

The outcome is not limited to the analysis of a single mission case, but provides the foundation for a generalized RHA reference architecture, an internal standard, flexible and scalable, to be used across current and future Kurs missions.





## ACKNOWLEDGMENTS

*“A testa tra li stiddi,  
i pieri 'nterra  
e lu cori ca voli spaccari  
u scuru ri lu spaziu”*

Un caloroso ringraziamento a tutte le persone che hanno contribuito, direttamente e indirettamente, in modo diverso alla realizzazione del mio lavoro di tesi. Alcuni hanno condiviso con me questo percorso da vicino, altri da lontano; alcuni sono ancora al mio fianco, altri hanno lasciato un vuoto, ma restano nel mio ricordo.

Un grazie speciale al mio relatore, Fabrizio Stesina, per la disponibilità, la pazienza e i consigli preziosi durante tutto il percorso. Ringrazio anche Kurs Orbital per avermi dato l'opportunità di lavorare su un progetto stimolante e di crescere professionalmente e umanamente.



# Table of Contents

<b>List of Tables</b>	IX
<b>List of Figures</b>	XI
<b>Acronyms</b>	XV
<b>1 Introduction to Space Radiation</b>	6
1.1 Natural Space Radiation Environment . . . . .	7
1.2 Galactic Cosmic Rays (GCRs) . . . . .	8
1.3 Solar Particle Events (SPEs) . . . . .	11
1.4 Trapped Radiation Belts . . . . .	14
<b>2 Interaction of Radiation with Matter</b>	24
2.1 Photon Interactions . . . . .	29
2.2 Electron Interactions . . . . .	31
2.3 Nucleons and Nuclear Reactions . . . . .	36
2.4 Ion Interactions . . . . .	40
2.5 Summary of Radiation Effects . . . . .	43
<b>3 Synthetic Worst-Case Orbit Definition for Radiation Environment Analysis</b>	45
3.1 Methodology and Considerations . . . . .	47
3.1.1 Low Earth Orbit (LEO) . . . . .	48
3.1.2 Medium Earth Orbit (MEO) . . . . .	49
3.1.3 Highly Elliptical Orbit (HEO) . . . . .	49
3.1.4 Geostationary Orbit (GEO) . . . . .	50
3.1.5 Summary of Selected Orbits . . . . .	51
<b>4 Modeling of the Space Radiation Environment</b>	53
4.1 Environment – Trapped Particles . . . . .	53
4.1.1 LEO and MEO . . . . .	53

4.1.2	GEO . . . . .	53
4.2	Environment – Solar Particles . . . . .	54
4.2.1	Average Statistical Models . . . . .	54
4.2.2	Solar Particle Peak Flux During a Solar Flare . . . . .	54
4.3	Environment – Galactic Cosmic Rays (GCR) . . . . .	56
4.4	Total Ionizing Dose (TID) and Total Non-Ionizing Dose (TNID) . .	56
4.4.1	TID Evaluation . . . . .	56
4.4.2	Displacement Damage Dose (DDD) . . . . .	57
4.5	Shielded Fluxes . . . . .	57
<b>5</b>	<b>Synthetic Orbit and Worst-Case Scenario</b>	<b>58</b>
5.1	TID and TNID Environment . . . . .	58
5.1.1	Protons Incident Fluence versus Energy Spectra . . . . .	59
5.1.2	Electrons Incident Fluence versus Energy Spectra . . . . .	62
5.1.3	Total dose curve . . . . .	67
5.1.4	On the "100 krad(Si)" Threshold as a Reference for TID Tolerance . . . . .	69
5.1.5	Total non-ionizing dose . . . . .	71
5.2	SEE Environment . . . . .	76
5.2.1	GCR fluxes versus LET spectrum calculated for an Alu- minium shield thickness of 3 mm . . . . .	76
5.2.2	Solar particle event fluxes versus LET spectrum for a given Aluminium shield thickness of 3 mm . . . . .	80
5.2.3	Trapped and solar protons shielded fluxes versus energy spec- tra behind 3 mm of Aluminium . . . . .	85
<b>6</b>	<b>Radiation Hardness Assurance Across Space Agency Development Phases</b>	<b>90</b>
6.1	Introduction . . . . .	90
6.2	RHA Methodology and Process Overview . . . . .	90
6.3	Phase 0/A: Mission Analysis and Feasibility . . . . .	91
6.4	Phase B: Preliminary Definition . . . . .	92
6.5	Phase C: Detailed Definition . . . . .	92
6.6	The NASA Programmatic Approach . . . . .	92
6.6.1	Defining the Radiation Hazard . . . . .	93
6.6.2	Evaluating the Hazard . . . . .	94
6.6.3	Defining Mission Requirements from the Hazard . . . . .	94
6.6.4	Evaluating Device Usage . . . . .	95
6.6.5	Engineering Collaboration and Design Iteration . . . . .	96
6.7	Risk Assessment in Radiation Hardness Assurance . . . . .	97
6.8	Outlook and Transition to Radiation Effects Characterization . . .	99



<b>7</b>	<b>Total Ionizing Dose</b>	<b>101</b>
7.1	Overview . . . . .	101
7.1.1	Relevant Environment . . . . .	101
7.1.2	Technologies Sensitive to TID . . . . .	102
7.1.3	Impacts on Technology . . . . .	104
7.1.4	TID Requirements . . . . .	105
7.1.5	Material Selection and Shielding Configuration Strategies . .	108
7.1.6	Radiation-Hardened and Radiation-Tolerant Component Op- tions: The Case of Texas Instruments . . . . .	114
7.1.7	Assessment of Shielding Strategies and Component Surviv- ability . . . . .	116
7.1.8	Advanced Modelling of Shielding for the Synthetic Orbit . .	121
7.1.9	Conclusion: Defining a Feasible TID Requirement for the Synthetic Orbit . . . . .	124
<b>8</b>	<b>Displacement Damage</b>	<b>126</b>
8.0.1	Relevant Environment . . . . .	127
8.0.2	Technologies Susceptible to Displacement Damage . . . . .	128
8.0.3	10.3 Displacement Damage: Phenomenology and Observation	131
8.0.4	10.4 Non-Ionizing Energy Loss (NIEL) Mechanisms . . . . .	132
8.0.5	Impact of DD on Electrical Properties . . . . .	134
8.0.6	Radiation Damage Evaluation Strategy . . . . .	134
8.0.7	TNID Hardness Assurance Strategy . . . . .	135
8.0.8	Displacement Damage Assurance Strategy for ARCap . . . .	137
<b>9</b>	<b>Single Event Effects</b>	<b>140</b>
9.1	Introduction . . . . .	140
9.1.1	Linear Energy Transfer (LET) . . . . .	141
9.1.2	Cross Section . . . . .	141
9.1.3	Sensitive Volume . . . . .	141
9.2	Destructive and Non-Destructive Single-Event Effects . . . . .	143
9.3	Energy Deposition and Charge Transport Mechanisms . . . . .	144
9.4	Relevant Environment . . . . .	145
9.5	Technologies Susceptible to Single Event Effects . . . . .	146
9.6	Prediction and Analysis of Single Event Effects in Electronic Com- ponents for Space Applications . . . . .	149
9.7	SEE Hardness Assurance . . . . .	151
<b>10</b>	<b>Design Trade-offs and Evolution of Radiation Requirements</b>	<b>155</b>
10.1	From Ambition to Realism: Refocusing on a LEO Mission Profile .	155
10.2	Radiation Environment Requirements for a 5-Year LEO Mission .	157

10.2.1	Component Radiation Requirements and Selection Strategy	157
10.2.2	Total Ionizing Dose (TID) Requirements . . . . .	157
10.2.3	Driven Screening Philosophy . . . . .	159
10.3	Comparison of Gamma and X-Ray Sources for TID Testing . . . . .	161
10.3.1	Gamma Rays vs. X-Rays . . . . .	161
10.3.2	Low-Energy X-Rays vs. High-Energy X-Rays . . . . .	162
10.3.3	Test Outcome Classification . . . . .	164
10.3.4	Final Technical Considerations for SEE Risk Assessment and Mitigation in COTS-Based ARCap Subsystems . . . . .	165
<b>11</b>	<b>Design-Centered Radiation Hardness Assurance Strategy</b>	<b>171</b>
11.1	Radiation-Tolerant Design Flow Embedded in Conceptual Design .	171
11.1.1	Designing to Preserve the Conceptual Architecture . . . . .	172
11.1.2	C0/C1/C2 Classification: A Guiding Framework . . . . .	172
11.1.3	Radiation Testing as a Filter, Not a Detonator . . . . .	173
11.1.4	Lessons from CERN's Radiation-Tolerant Developments . .	173
11.2	Risk Assessment of Radar Front-End Components . . . . .	173
11.2.1	Risk Assessment Methodology: DC, FC and RDM . . . . .	174

# List of Tables

3.1	Contribution of each environment to different radiation effects . . .	47
3.2	Summary of selected orbits . . . . .	51
4.1	Models for trapped particles in LEO and MEO environments . . . .	54
4.2	Models for trapped particles in GEO environment . . . . .	54
4.3	Models for solar energetic particles (average statistical models) . . .	55
4.4	Models for solar particle peak flux during a solar flare . . . . .	55
4.5	Models for galactic cosmic rays (GCR) . . . . .	56
4.6	Models for TID evaluation . . . . .	56
4.7	Models for the Displacement Damage Dose (DDD) . . . . .	57
4.8	Models for shielded fluxes calculation . . . . .	57
5.1	OMERE – Trapped Proton Integral Fluence for a 5-year mission . .	60
5.2	SPENVIS – Trapped Proton Integral Fluence for a 5-year mission .	61
5.3	OMERE – Trapped Electron Integral Fluence for a 5-year mission in LEO, MEO and Molniya orbits . . . . .	63
5.4	OMERE – Trapped Electron Integral Fluence for a 5-year mission in GEO orbit . . . . .	63
5.5	OMERE – Trapped Electron Integral Fluence for a 5-year mission in the Synthetic orbit . . . . .	64
5.6	SPENVIS – Trapped Proton Integral Fluence for a 5-year mission .	65
5.7	OMERE – TID results for a 5-year mission . . . . .	67
5.8	SPENVIS – TID results for a 5-year mission . . . . .	68
5.9	OMERE – displacement damage dose for Silicon for a 5-year mission	71
5.10	SPENVIS – displacement damage dose for Silicon for a 5-year mission	72
5.11	OMERE – displacement damage dose for Gallium Arsenide (GaAs) for a 5-year mission . . . . .	73
5.12	SPENVIS – displacement damage dose for Gallium Arsenide (GaAs) for a 5-year mission . . . . .	74
5.13	OMERE – GCR integral fluxes . . . . .	77
5.14	SPENVIS – GCR integral fluxes . . . . .	77

5.15	OMERE – solar energetic particle (SEP) integral fluxes . . . . .	80
5.16	SPENVIS – solar energetic particle (SEP) integral fluxes . . . . .	81
5.17	OMERE – Solar Particle Worst-Case 5-Minute Integral Flux . . . . .	82
5.18	SPENVIS – Solar Particle Worst-Case 5-Minute Integral Flux . . . . .	82
5.19	OMERE – shielded proton integral flux . . . . .	86
5.20	SPENVIS – shielded proton integral flux . . . . .	87
7.1	Technologies susceptible to TID effects . . . . .	103
7.2	EEE part families potentially sensitive to TID (adapted from ECSS-Q-ST-60-15C) [30] . . . . .	107
7.3	Energy deposition values under proton radiation at 3000 km altitude	111
7.4	TID ratings for selected TI space components [35] . . . . .	115
7.5	Dose deposition in silicon for 20 mm aluminum shielding (3000 km orbit) . . . . .	122
7.6	Dose results for 10 mm aluminum + 5 mm polypropylene configuration	122
7.7	Dose results for 10 mm aluminum + 3 mm polypropylene configuration	124
8.1	Typical Displacement Damage Effects by Technology . . . . .	129
8.2	Component families potentially sensitive to TNID [30] . . . . .	136
9.1	Radiation environment to be assessed based on LET <sub>th</sub> [4] . . . . .	152
9.2	SEE types to be considered in accordance with ECSS-Q-ST-60-15C [4] and [30] . . . . .	153
10.1	Total ionizing dose versus aluminum thickness for a 5-year LEO mission . . . . .	157
11.1	Component Classification with Design & Functional Criticality . . . . .	178

# List of Figures

1.1	Structure of Earth's magnetosphere, showing the interaction with the solar wind, the bow shock, the magnetopause, the Van Allen radiation belts, the plasmasphere and the plasma sheet extending into the magnetotail [11]. . . . .	13
2.1	Diagram illustrating the possible outcomes when particle radiation strikes a thin slab of material [6]. . . . .	26
2.2	The three primary mechanisms by which photons lose energy when interacting with matter: the photoelectric effect, Compton scattering and pair production [6]. . . . .	30
2.3	Plot of the total mass attenuation coefficient as a function of photon energy, highlighting the contributions from the three main energy absorption mechanisms: the photoelectric effect, Compton scattering and pair production [6]. . . . .	32
2.4	Diagram of the three primary mechanisms for electrons interacting with matter: elastic electron-electron, inelastic electron electron and inelastic electron-nucleus scattering [6]. . . . .	33
2.5	Electron range as a function of energy in silicon (blue curve) and tungsten (red curve). Due to tungsten's higher density and greater atomic number ( $Z$ ) compared to silicon, electrons have a significantly shorter range in tungsten [6]. . . . .	35
2.6	Elastic (top) and inelastic (bottom) nuclear reactions between an energetic neutron and a silicon target nucleus. In an elastic collision, the neutron "bounces" off the nucleus without being absorbed, transferring some energy and creating a recoil nucleus. In an inelastic collision, the neutron is absorbed by the nucleus, leaving it in a highly excited state [6] . . . . .	37
2.7	Immediately following an inelastic nuclear reaction, the nucleus remains in a highly excited state. It subsequently releases its excess energy through one of four possible pathways [6] . . . . .	38

2.8	Linear energy transfer (LET) of a Xenon ion in silicon as a function of ion energy, illustrating the two distinct energy-loss mechanisms: electronic stopping (at higher energies) and nuclear stopping (at lower energies) [6]. . . . .	41
2.9	Comparison of the linear charge generated per distance traveled ( $dQ/dx$ ) by various radiation types in silicon as a function of the incident particle energy. Note that heavier ions are orders of magnitude more disruptive than other particles [6]. . . . .	42
3.1	Solar Cycle 25 progression as reported by NOAA Space Weather Prediction Center. The plot shows the observed and predicted monthly sunspot numbers, highlighting the current solar maximum phase expected to peak in 2025, followed by a gradual decline toward the next solar minimum around 2030, as reported in [24]. . . . .	52
5.1	Schematic representation of the evaluation path for the characterization of the space radiation environment. . . . .	59
5.2	Trapped proton environment: results from OMERE are shown on the left, while SPENVIS results are shown on the right . . . . .	61
5.3	Trapped electron environment: results from OMERE are shown on the left, while SPENVIS results are shown on the right . . . . .	66
5.4	Dose depth curve: results from OMERE are shown on the left, while SPENVIS results are shown on the right . . . . .	68
5.5	Non-ionizing dose depth curve for Silicon target material: results from OMERE are shown on the left, while SPENVIS results are shown on the right . . . . .	72
5.6	Non-ionizing dose depth curve for GaAs target material: results from OMERE are shown on the left, while SPENVIS results are shown on the right . . . . .	74
5.7	GCR Fluxes: results from OMERE are shown on the left, while SPENVIS results are shown on the right . . . . .	78
5.8	SEP Fluxes: results from OMERE are shown on the left, while SPENVIS results are shown on the right . . . . .	81
5.9	SEP Fluxes in the worst-case 5-minutes condition: results from OMERE are shown on the left, while SPENVIS results are shown on the right . . . . .	83
5.10	Shielded proton fluxes: results from OMERE are shown on the left, while SPENVIS results are shown on the right . . . . .	88
6.1	RHA process overview [4]. . . . .	91

7.1	Energy deposition and pulse-height analysis for 5 mm layer of Aluminum . . . . .	111
7.2	Energy deposition and pulse-height analysis for 10 mm layer of Aluminum . . . . .	112
7.3	Energy deposition and pulse-height analysis for 5 mm layer of Polyethylene . . . . .	112
7.4	Energy deposition and pulse-height analysis for 10 mm layer of Polyethylene . . . . .	112
7.5	Energy deposition and pulse-height analysis for 5 mm layer of Polypropylene . . . . .	113
7.6	Energy deposition and pulse-height analysis for 10 mm layer of Polypropylene . . . . .	113
7.7	MULASSIS - Results for 10 mm Polyethylene layer + 150 mm Silicon layer in a spherical geometry . . . . .	118
7.8	MULASSIS - Configuration of particle environment and geometry .	122
7.9	MULASSIS - Shielding geometry with a hybrid configuration . . . .	123
8.1	Schematic illustration of a vacancy (light gray) and an interstitial atom (dark gray) formed in a silicon lattice after an energetic particle strike [6]. . . . .	127
8.2	Voltage response of a PNP transistor to gamma-ray exposure (TID) vs. proton-induced displacement damage [6]. . . . .	130
8.3	NIEL rate in silicon for protons, electrons and neutrons as a function of particle energy [2]. . . . .	133
9.1	SEE cross section versus LET [2]. . . . .	142
9.2	Direct and indirect ionization mechanisms for heavy ions, protons and neutrons [2]. . . . .	144
9.3	SEE susceptibility as a function of component technology and device family [2]. . . . .	146
10.1	Comparison of the photon spectrum of the used X-ray generator and 60-Co source with the relative importance of the photoelectric effect, Compton scattering and pair production [49]. . . . .	162





# Acronyms

**ADC**

Analog-to-Digital Converter

**APS**

Active Pixel Sensor

**BJT**

Bipolar Junction Transistor

**BLDC**

Brushless Direct Current

**CCD**

Charge-Coupled Device

**CDR**

Critical Design Review

**CME**

Coronal Mass Ejection

**CMOS**

Complementary Metal-Oxide-Semiconductor

**CONOPS**

Concept of Operations

**COTS**

Commercial Off-The-Shelf

**CRRES**

Combined Release and Radiation Effect Satellite

**CTE**

Coefficient of Thermal Expansion

**DC**

Design Criticality

**DDD**

Displacement Damage Dose

**DDEF**

Displacement Damage Equivalent Fluence

**DPU**

Data Processing Unit

**DRAM**

Dynamic Random-Access Memory

**DUT**

Device Under Test

**ECSS**

European Cooperation for Space Standardization

**EDAC**

Error Detection and Correction

**EEE**

Electrical, Electronic and Electromechanical

**ELDRS**

Enhanced Low-Dose Rate Susceptibility

**ELDR**

Enhanced Low-Dose Rate

**EM**

Engineering Model

**EMI**

Electromagnetic Interference

**EOL**

End Of Life

**ESA**

European Space Agency

**ESCC**

European Cooperation for Space Standardization

**ESCIES**

European Space Components Information Exchange System

**ESD**

Electrostatic Discharge

**ESP**

Energetic Solar Particle

**FC**

Functional Criticality

**FM**

Flight Model

**FMECA**

Failure Mode, Effects and Criticality Analysis

**GCR**

Galactic Cosmic Ray

**GEO**

Geostationary Orbit

**GNSS**

Global Navigation Satellite System

**GPS**

Global Positioning System

**GSO**

Geosynchronous Orbit

**HDR**

High Dose Rate

**HEO**

Highly Elliptical Orbit

**IC**

Integrated Circuit

**IGBT**

Insulated-Gate Bipolar Transistor

**IRPP**

Integrated Rectangular Parallelepiped

**ISS**

International Space Station

**JFET**

Junction Field-Effect Transistor

**KP**

Kennel-Petschek

**LDC**

Lot Date Code

**LDR**

Low Dose Rate

**LEO**

Low Earth Orbit

**LET**

Linear Energy Transfer

**LHC**

Large Hadron Collider

**MCU**

Microcontroller Unit

**MEAL**

Mission, Environment, Application and Lifetime

**MEMS**

Micro-Electro-Mechanical Systems

**MEO**

Medium Earth Orbit

**MOSFET**

Metal-Oxide-Semiconductor Field-Effect Transistor

**MOS**

Metal-Oxide-Semiconductor

**MRDM**

Minimum Radiation Design Margin

**MTBF**

Mean Time Between Failures

**NIEL**

Non-Ionizing Energy Loss

**NMOS**

N-type Metal-Oxide-Semiconductor

**NOAA**

National Oceanic and Atmospheric Administration

**NPN**

Negative-Positive-Negative (Transistor)

**OOS**

On-Orbit Servicing

**PEM**

Plastic Encapsulated Microcircuit

**PKA**

Primary Knock-on Atom

**PMOS**

P-type Metal-Oxide-Semiconductor

**PNP**

Positive-Negative-Positive (Transistor)

**QPL**

Qualified Part List

**RDM**

Radiation Design Margin

**RF**

Radio Frequency

**RHA**

Radiation Hardness Assurance

**RLAT**

Radiation Lot Acceptance Testing

**RPOC**

Rendezvous, Proximity Operations and Capture

**RPP**

Rectangular Parallelepiped

**RVT**

Radiation Verification Testing

**SAA**

South Atlantic Anomaly

**SDRAM**

Synchronous Dynamic Random-Access Memory

**SEB**

Single Event Breakdown

**SED**

Single Event Dis turb

**SEDR**

Single Event Dielectric Rupture

**SEECA**

Single Event Effect Criticality Analysis

**SEE**

Single Event Effects

**SEFI**

Single Event Functional Interrupt

**SEGR**

Single Event Gate Rupture

**SEHE**

Single Event Hard Error

**SEL**

Single Event Latchup

**SEP**

Solar Energetic Particle

**SESB**

Single Event Snapback

**SET**

Single Event Transient

**SEU**

Single Event Upset

**SMU**

Single Word Multiple-Bit Upset

**SOA**

Safe Operating Area

**SOI**

Silicon On Insulator

**SOS**

Silicon On Sapphire

**SOTA**

State Of The Art

**SOTP**

State Of The Practice

**SPE**

Solar Particle Event

**SRR**

System Requirements Review

**SSO**

Sun Synchronous Orbit

**SWPC**

Space Weather Prediction Center

**TIDL**

Total Ionizing Dose Level

**TIDS**

Total Ionizing Dose Susceptibility

**TID**

Total Ionizing Dose

**TMR**

Triple Modular Redundancy

**TNIDL**

Total Non-Ionizing Dose Level



**TNIDS**

Total Non-Ionizing Dose Susceptibility

**TNID**

Total Non-Ionizing Dose

**WCA**

Worst Case Analysis

# Objectives and Scope

## ARCap System Overview and Radiation Hardness Assurance Framework

ARCap is an advanced payload module under development by Kurs Orbital to enable fully autonomous Rendezvous, Proximity Operations and Capture (RPOC) of non-cooperative or tumbling targets in orbit. Designed as a key enabler for On-Orbit Servicing (OOS), debris mitigation and satellite life extension missions, ARCap integrates a suite of high-performance sensors and robotic systems to execute proximity operations with minimal ground intervention.

The ARCap payload includes the following core subsystems:

- **X-Band Radar:** used for long-range target acquisition and relative navigation during early-phase rendezvous.
- **W-Band Radar Array:** a cluster of high-resolution short-range radars optimized for close proximity sensing, target characterization and situational awareness.
- **LiDAR-Based and Optical-Based Machine Vision System:** provides tracking and target recognition from raw data such as point clouds and images.
- **Robotic Arms (x3):** each arm is approximately 2 meters in length and is used for mechanical capture or servicing actions.
- **Distributed Data Processing Architecture:** post-processing of sensor data is performed within each sensor subsystem via dedicated Data Processing Units (DPUs).

The module supports modular integration and scalability, allowing it to be tailored to specific mission architectures and servicing objectives.

## Radiation Context and Motivation

As the concept of ARCap is to support autonomous rendezvous and capture in increasingly complex orbital scenarios, including operations in harsh radiation environments, it is crucial to ensure that all parties, involved in the design, deployment and operation of the system, are cognizant of the risks posed by the requirements derived from mission, environment, application and lifetime factors. Based on the need to develop and implement timely and application-specific guidelines to ensure that threats from the natural space radiation environment do not compromise the operational reliability of the ARCap system, this thesis defines a methodology for deriving Radiation Hardness Assurance (RHA) requirements. The objective is to support the evaluation of avionics and sensor subsystems in terms of Total Ionizing Dose (TID), Total Non-Ionizing Dose (TNID) and Single Event Effects (SEE).

## Objectives and Contributions

The thesis surveys existing standards and methodologies with the aim of outlining a theoretical and practical framework for Radiation Hardness Assurance (RHA). The work draws from established literature, best practices and standards to define a structured qualification process that starts at the subsystem design phase. The objective is to build an Engineering Model (EM) with the awareness that its electronic components are destined for space operation. This approach aims to reduce the gap between Engineering Models (EM) made with COTS components and the final Flight Models (FM), accelerating the qualification timeline and minimizing the risk of unexpected failures. By integrating radiation considerations from the earliest stages of design, components are selected with criteria aligned to their end-use environment, promoting a more robust and predictable qualification process. This thesis does not propose new technical standards or impose predefined qualification flows; rather, it aims to serve as a practical and theory-grounded guideline for implementing Radiation Hardness Assurance (RHA), in the context of a space startup developing payloads under tight development timelines and investor funding, in which there is a strong imperative to accelerate the path to flight. With a mission planned within just a few years, the design approach must integrate radiation assurance considerations from the outset to mitigate technical risk and ensure timely qualification. The motivation behind this effort stems from the need to enable true modularity in space systems, designing a payload that can adapt seamlessly to a wide range of missions and orbital environments. This vision, captured in the thesis title through the concept of *"Plug-and-Play in Orbit"*, requires a structured approach to radiation assurance that goes beyond single-mission tailoring. Instead, it demands a generalized, scalable methodology capable of guiding component selection, system design and qualification across different operational

scenarios from the outset and in conditions where radiation exposure becomes a critical design factor from the earliest phases. Unlike institutional programs, where heritage and conservative margins often dominate component selection, commercial space servicing platforms are under pressure to reduce development time and cost. This creates a gap between the state of the practice (SOTP), what has flown and is fully qualified and the state of the art (SOTA), which includes emerging COTS-based solutions with promising performance but limited radiation flight heritage. This work acknowledges that much of the know-how in the space radiation assurance field is still highly experience-based and concentrated in a limited number of experts. Therefore, a central goal is to aggregate, structure and translate that knowledge into an accessible methodology for subsystem designers. The proposed framework spans the primary radiation effects while also discussing interaction particles-matter, shielding strategies, real effects on electronics, testing approaches and early-phase screening of commercial components. Ultimately, the thesis promotes a design-for-qualification mindset: building Engineering Models (EMs) with radiation constraints already embedded in the design and part selection process, accelerating the transition from development to deployment for space-based subsystems.

## **Intended Use and Broader Impact**

The goal of this technical memorandum is to document the state of NASA and ESA's current RHA best practices and making them accessible through a clear, application-driven framework across a logical entry point and a coherent methodology, to Kurs Orbital colleagues, so that engineers and system designers can navigate the qualification process with clarity and purpose from the very first design decisions. It is hoped that this document will serve not only as an aid and a reference, but also as a body of knowledge to educate and inform to the challenges of radiation assurance and methods to understand, mitigate and manage radiation effects in avionics systems.

# Expected Outcomes

This thesis is intended to support the Phase 0/A feasibility assessment of the ARCAP module by providing a comprehensive, physics-based methodology for evaluating radiation effects on spacecraft electronics in the context of a worst-case orbital environment. The work will be structured in order to combine theoretical analysis of radiation-matter interaction mechanisms with a practical implementation of environment modeling, requirement derivation and design evaluation. Particular attention is given to the application of Radiation Hardness Assurance (RHA) principles, including the derivation of critical parameters for Total Ionizing Dose (TID), Displacement Damage Dose (DDD/TNID) and Single Event Effects (SEE), as well as to the definition of early screening strategies for Commercial-Off-The-Shelf (COTS) components. A key expected outcome is the development of a radiation analysis workflow, where environmental particle fluxes will be derived in order to characterize and specify the operative environment. This approach aims to estimate radiation levels and threat to support both requirement definition and design optimization. As such, the thesis promotes the use of fidelity-appropriate simulation tools tailored to the goal of the characterization of the environment under specific conditions and high-level definition of the radiation effects. Furthermore, the study aims to demonstrate that radiation is not merely a compliance constraint but a fundamental design driver. The presence of increasingly integrated COTS technologies introduces significant uncertainty and risk in long-duration or harsh radiation environments. Therefore, the thesis is expected to provide not only technical input to the ARCAP project but also a reusable methodology for early-phase radiation engineering, integrating environment definition, parts screening, transport simulation and design feasibility assessment into a coherent and traceable framework. In addition, the feasibility assessment, performed under conservative assumptions, is expected to rely on the extraction of a mission-integrated accumulated dose value, the Total Ionizing Dose Level (TIDL) at end-of-life. This reference dose, when compared with the radiation tolerance specifications of known rad-hard technologies, allows identifying the minimum required hardness level and technology class. At the same time, it defines a screening threshold for COTS components: those intended for use must be tested at least up to this TIDL value.

This dose threshold, together with the analysis of TID, TNID and SEE risks, enables a conservative but practical definition of the feasibility boundary, consistent with the available analysis tools, test facilities and programmatic constraints. Finally, the study is also expected to explore shielding-based mitigation strategies by assessing the impact of material configurations and placement on radiation dose levels at sensitive component locations. However, for Displacement Damage (DD) and Single Event Effects (SEE), the scope remains limited to the accurate characterization of the environmental particle fluxes and the qualitative evaluation of their expected impact on microelectronics. No device-level modeling of such effects is foreseen at this stage, in line with the early-phase objective of system-level feasibility assessment rather than detailed component qualification.

# Chapter 1

## Introduction to Space Radiation

The impact and severity of radiation on electronic components are primarily determined by the specific characteristics of the devices and the radiation environment in which they operate. This chapter provides an overview of the main radiation sources found in space, particularly those encountered beyond the Earth's atmospheric shield. The subsequent chapters will explore how different types of radiation affect various electronic devices.

### Introduction to the Chapter

The information presented in this chapter has been adapted, reformulated and summarized primarily from the *Radiation Handbook for Electronics* [6], the ECSS standard *ECSS-E-ST-10-04C – Space Environment* [3] and the technical documentation available for the SPENVIS [8] and OMERE [8] environmental modeling tools. These sources provide the reference framework for describing the main space radiation environments and the interaction mechanisms with the materials and electronic technologies used onboard spacecraft.

The durability and reliability of microelectronic devices operating in the space radiation environment is primarily influenced by the cumulative effects of ionizing radiation and displacement damage, along with the occurrence of frequent single-event effects. The level of radiation encountered by onboard electronics depends on several factors: the spacecraft's orbital path, the duration of the mission, the thickness and material of protective shielding and the intensity and frequency of solar disturbances such as flares and coronal mass ejections (CMEs). The protective influence of Earth's magnetic field against space radiation also varies based on the

specific orbit.

Low Earth Orbits (LEOs), situated at relatively low altitudes, require less energy to reach and maintain, making them cost-effective. These orbits offer minimal signal latency, short communication paths and high-resolution Earth observations. Medium Earth Orbit (MEO), located between LEO and Geostationary Orbit (GEO) at an altitude of 35,786 km, is commonly utilized for applications like global navigation systems (e.g., GPS), communication services and scientific monitoring. Both GEO and Geosynchronous Orbit (GSO) match Earth's rotation, resulting in a 24-hour orbital period. While GEO satellites maintain a constant position above the equator, those in GSO may oscillate north and south due to orbital inclination. Any satellite positioned above GEO is classified as operating in Highly Elliptical Orbit (HEO).

LEO missions, especially those near the equator, benefit most from the geomagnetic shielding provided by the Earth, effectively reducing radiation exposure. Conversely, spacecraft in higher orbits such as GEO or those with highly inclined or polar trajectories experience weaker magnetic protection or missions in MEO, passing through regions of the Van Allen belts, see a concentration of high-energy particle fluxes significantly elevated. This leads to missions with a greater vulnerability to energetic particles and, as consequence, a greater risk of radiation-induced disturbances.

## 1.1 Natural Space Radiation Environment

On February 1st, 1958, following the launch of Explorer 1, scientific instruments onboard the satellite detected the existence of high-energy charged particles, including electrons and protons, trapped by Earth's magnetic field. This discovery marked the first recorded observation of radiation in space, a region now recognized as the Van Allen radiation belts [9].

In the context of space environments, radiation refers specifically to the energetic charged particles, such as electrons, protons and heavy ions, that pose a risk to spacecraft. These particles originate from three principal sources:

- Galactic Cosmic Rays (GCRs): these are highly energetic protons (approximately 89%) and heavier ions (roughly 11%) that originate from outside our solar system and arrive in a nearly uniform manner, as isotropic flux, from all directions, according to [6].
- Radiation Belts: these consist of particles captured by the magnetic fields surrounding planets, forming toroidal-shaped regions densely populated with trapped particles.



- Solar Energetic Particles (SEPs): these are intense bursts of high-energy particles generated during solar events, such as solar flares and coronal mass ejections (CMEs). The Sun also emits a continuous flow of lower-energy particles, known as the solar wind, composed of plasma and magnetic flux, which is occasionally intensified by solar storms.

Radiation in space not only affects the exterior surfaces of spacecraft but can also penetrate their structure, causing ionization or atomic displacement within materials. Such interactions can trigger transient signals, degrade material properties or cause significant failures in electronic systems.

Broadly, the radiation environment near Earth is divided into two categories: the trapped radiation environment, dominated by the Van Allen belts and the transient radiation environment, which includes galactic cosmic rays and solar event particles. While GCRs are present at low intensities, they carry extremely high energy levels and include all known atomic nuclei. In contrast, solar events release bursts of protons, alpha particles, electrons and heavy ions with significant variability.

Furthermore, as reported by [10], a low-energy plasma consisting of electrons and protons is also present in space, with fluxes reaching up to  $10^{12}$  particles per  $\text{cm}^2$  per second. In the trapped environment, this plasma component is generally below 0.1 MeV and does not typically affect internal electronics but can cause charging effects on spacecraft surfaces, particularly contributing to discharges and material damage.

## 1.2 Galactic Cosmic Rays (GCRs)

Interstellar gas usually tends to organize into massive clouds of neutral atoms or molecules. When these clouds approach energetic regions, such as stars, they begin to ionize. This gas is constantly in motion, compressing, dissipating and reacting to the local balance of magnetic fields, temperature gradients, gravity and radiation. These forces create turbulence that shapes how the gas evolves: it can slow down large-scale collapse while simultaneously triggering localized compression that leads to star formation. In this way, interstellar gas serves both as the foundation and fuel for galaxies and stars.

The interplanetary medium, the space environment of our solar system, begins where the interstellar medium ends. The solar wind, a continuous stream of charged particles ejected from the Sun, travels outward in all directions until it eventually slows to subsonic speeds at a boundary known as the termination shock. This boundary lies roughly twice the distance of Pluto's orbit from the Sun. Beyond this point, the solar wind's density drops so much that it can no longer push against the interstellar medium effectively.

Encasing the solar system is the heliosphere, a vast bubble formed by the Sun's magnetic field and the outward flow of the solar wind. The edge of this bubble, called the heliopause, marks the boundary where the solar influence gives way to the interstellar environment. The heliosphere acts as a shield, deflecting many lower-energy cosmic rays. Particles with energies below around 50 MeV generally can't penetrate it, meaning that roughly three-quarters of GCRs are stopped before reaching the inner solar system.

It's believed that GCRs gain their incredible speeds through acceleration by shock waves from supernova explosions. The galactic magnetic field then bends and deflects their paths, scattering them until they arrive in our solar system from all directions. Many of these particles have been traveling through space for tens of millions of years and their direction has been randomized over time such that they are isotropic. Most GCRs carry kinetic energies around 1 GeV, though some rare particles reach energies exceeding  $10^{20}$  eV. For comparison, even the most energetic solar protons rarely exceed 1 GeV. The GCR flux below 100 MeV is deflected by the heliosphere. Above 1 GeV, the cosmic ray flux decreases fairly consistently with an increase in particle energy: the higher the energy of the particle, the rarer it is.

Within the heliosphere, the interplanetary magnetic field further deflects GCRs, particularly those with lower energies. This deflection varies with the solar cycle: during periods of high solar activity, the increased solar magnetic field strength leads to greater shielding, reducing the GCR flux. When the Sun is quieter, GCR fluxes rise. In fact, the intensity of GCRs can vary by a factor of five depending on where we are in the 11-year solar cycle.

Sunspot numbers, which serve as a key indicator of solar magnetic activity, rise and fall in this same cycle. During solar maximum, when sunspots are abundant, the stronger magnetic fields provide better protection against GCRs, especially those with lower rigidity. This inverse relationship, where GCR flux decreases as solar activity increases is also accompanied by the great variability between a solar minimum and maximum: the lower a particle's rigidity, the more sensitive it is to being deflected and therefore the more its flux changes between solar maximum and minimum.

Although GCR flux is lower than that of trapped particles near Earth, the danger they pose is considerable. Their high energies allow them to penetrate deeply into spacecraft materials and electronics. They also deposit large amounts of energy in a short distance, measured by their linear energy transfer (LET). High LET particles are particularly problematic in space systems because they can trigger single-event effects (SEEs), especially in orbits outside the magnetosphere's protective influence.

GCRs are mostly made up of ionized hydrogen (89%) and helium (9%), with the remaining 2% being electrons and heavier nuclei, including trace amounts of elements up to uranium ( $Z = 92$ ). These particles are detected not just in space, but

also indirectly on Earth: when GCRs strike the atmosphere, they create showers of secondary particles that can be measured at the surface and even underground.

Given their intensity, energy and unpredictability, completely shielding a spacecraft from GCRs is practically impossible. The high costs and strict mass limitations of space missions make such shielding unfeasible, so mitigation strategies focus on minimizing exposure and hardening systems against their effects.

Before galactic cosmic rays (GCRs) can reach a spacecraft orbiting Earth, they must first pass through the planet's magnetic barrier, known as the magnetosphere. This protective region surrounds Earth and is shaped by its magnetic field, which originates from the dynamic flow of molten, electrically conductive materials in the planet's outer core. The magnetosphere isn't static; it constantly responds to solar activity, planetary motion and influences from the broader interstellar environment.

Shaped somewhat like a comet, the magnetosphere is compressed on the side facing the Sun, extending around 6 to 10 Earth radii outward, while the opposite side stretches far into space, forming a long magnetotail that can reach hundreds of Earth radii in length. This structure acts as a powerful shield against many incoming charged particles, including GCRs, which are deflected as they travel through the magnetic field.

The motion of GCRs within the magnetosphere is governed by the Lorentz force, which describes how charged particles are influenced by electric and magnetic fields. The degree to which a particle is deflected depends on its charge, velocity and the strength and direction of the magnetic field it encounters. One of the key properties that defines how deeply a particle can penetrate a magnetic field is its rigidity, a parameter that relates the particle's momentum to its charge.

Because Earth's magnetic field weakens with altitude and is more intense near the equator than at the poles, the minimum energy a charged particle needs to reach a specific location, called the geomagnetic cut-off rigidity, varies by location. This threshold drops to nearly zero at the magnetic poles and at the outer edges of the magnetosphere, making those regions more vulnerable to particle penetration.

This is why the orbit matters greatly when it comes to GCR exposure. LEO orbits, especially near the equator, benefit from stronger magnetic shielding. In contrast, spacecraft in GEO or beyond, as well as those in polar or highly inclined orbits, receive much less protection and are far more exposed to high-energy cosmic rays.

In addition to magnetic shielding, Earth's physical presence offers another form of protection, called the Earth shadow effect. At lower altitudes, the planet itself blocks part of the sky, reducing the number of possible paths that cosmic rays can take to reach a spacecraft: the presence of the solid Earth occults part of the solid angle from which particles can arrive at a given location. This effect, combined with magnetic shielding, plays a fundamental role in enabling humans to live and work safely in space and in protecting technology in orbit.

However, when we move beyond this protective envelope, for example, in missions to Mars, the lack of natural shielding becomes a major concern. Shielding astronauts and equipment from cosmic radiation in deep space is a challenging task. The levels of protection required would require thick layers of material, such as aluminum, which are often too heavy and costly to launch. This need for robust radiation protection remains one of the key technical hurdles for long-duration human space exploration.

### 1.3 Solar Particle Events (SPEs)

The Sun, through the continuous nuclear fusion of hydrogen into helium, acts as the most powerful and persistent radiation source in the solar system, emitting over  $60 \text{ MW/m}^2$ . Two prominent features associated with solar radiation are the photosphere, a visible surface emitting light and the corona, a surrounding layer of superheated plasma reaching temperatures of approximately one million Kelvin.

The photosphere is a huge network of relatively small, dynamic, cell-like granules formed by localized convection cells. Convection granules and sunspots, appearing in the images as black areas, are the primary features of the photosphere surface. Convection is driven by heated plasma that rises from the interior and spreads across the surface. As the plasma cools during the lateral spreading, it ultimately sinks back to the cooler interior. Among the most distinctive features of the photosphere are sunspots, which appear as dark patches in solar imagery. These are regions where intense magnetic fields suppress convection, leading to lower temperatures compared to the surrounding areas. Sunspots typically emerge in pairs, representing opposite magnetic poles, such as the ends of a bar magnet.

Sunspots are not permanent; they form and dissipate over a span of days to weeks. Their appearance follows an 11-year solar cycle that alternates between periods of low and high activity. During the quieter phase, sunspots are few and far. In contrast, during the active phase, their numbers increase significantly. This rise in sunspot activity is closely linked to stronger solar magnetic storms, which, in turn, are responsible for some of the most intense and potentially damaging forms of solar radiation.

Solar radiation manifests itself in three principal forms: steady solar wind, sudden solar flares and coronal mass ejections (CMEs). The solar wind, composed of electrons, protons, helium nuclei and a few heavier ions, flows continuously from the corona at speeds of  $300\text{--}800 \text{ km/s}$ . Although most of these particles have relatively low energy and are largely deflected by planetary magnetic fields, they can still cause magnetospheric disturbances and affect Earth's magnetic storms.

Flares and CMEs are highly energetic and short-lived phenomena that significantly impact spacecraft systems. Solar flares are abrupt increases in brightness

that result from a sudden release of magnetic energy that has accumulated in localized regions. Flares typically erupt near sunspots, where chaotic and sharply changing magnetic fields destabilize the surrounding plasma. This instability can trigger violent energy discharges, ejecting massive amounts of material from the solar corona into space at extremely high speeds.

During these explosive events, the Sun releases energy across the full electromagnetic spectrum, from long-wavelength radio waves to highly energetic gamma rays. The released magnetic energy also accelerates particles such as electrons, protons and even heavier ions, pushing them to extreme kinetic energies that can travel great distances through space and impact both spacecraft and planetary environments.

CMEs involve the ejection of large quantities of plasma and magnetic fields from the solar corona. Both events, solar flares and CMEs, are more frequent during solar maximum and high solar activity periods and can accelerate particles to very high energies. For instance, during solar minimum, CMEs typically occur around once per week. At solar maximum, however, that rate increases dramatically to several CMEs per day.

One of the most critical consequences of flares and CMEs is the generation of solar energetic particles (SEPs), high-speed electrons, protons and heavier ions accelerated by these explosive events or the shock waves they create. SEP intensities can spike by factors of hundreds to even millions compared to background levels. These particles can reach energies ranging from about 1 MeV to 1 GeV, making them fast and highly penetrative.

Because these eruptions are highly directional, they tend to affect only specific areas of space. Still, when a spacecraft is caught within the path of one, the particle flux can exceed normal space radiation levels by several orders of magnitude.

It's worth noting that due to their directional nature, CMEs don't impact all satellites equally. Many will never encounter a CME directly during their operational lifetime. Nevertheless, these events are still of concern due to their potential to deform Earth's magnetic field. The massive magnetic shock waves created during a CME can compress or stretch the magnetosphere, disturbing the radiation belts and sometimes triggering powerful geomagnetic storms.

SEP events are far more frequent during solar maximum and their intensity and composition vary significantly from one event to another. This variability makes them notoriously difficult to model or predict: probabilistic tools and statistical models based on historical data can offer statistical estimates of the likelihood of a certain number of events occurring over a mission timeframe.

For spacecraft operating in orbits where SEPs are likely to strike, these particles, in terms of peak fluxes and energy spectra, are often the main factor in defining design limits and requirements for single-event effects (SEEs). Unfortunately, the warning time before a flare or CME impacts a satellite is often very short

and unreliable. SEEs have been recorded during both active and quiet periods, underscoring the unpredictability of these phenomena.

Evaluating the radiation effects of solar protons is essential, not only for their potential to cause ionization but also for their contribution to long-term degradation through non-ionizing energy loss. Both types of damage must be considered when assessing system longevity and resilience in space.

When charged particles from the solar wind reach Earth, they interact with its magnetic field, compressing it on the side facing the Sun and forming the protective bubble known as the magnetosphere. This compression results in a Bow Shock, where the supersonic solar wind abruptly slows and deflects. On the opposite side, the magnetic field is stretched far into space, creating an elongated region called the magnetotail. Although the magnetosphere is under constant bombardment by solar particles, most of them are deflected away by the magnetic field. However, some manage to enter through the polar regions, where the field lines are open and become trapped in the Earth's magnetic environment.

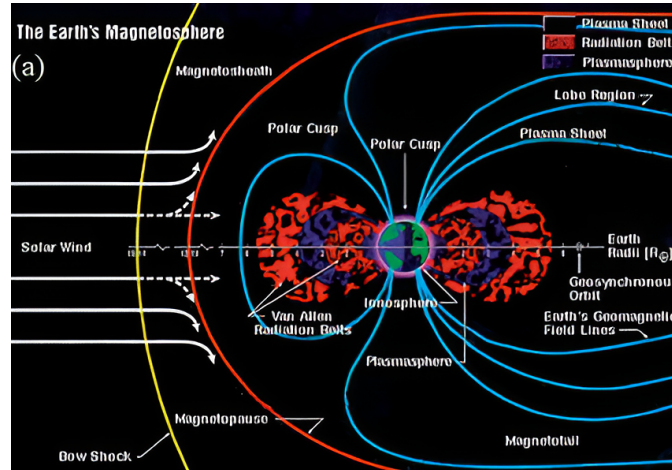


**Figure 1.1:** Structure of Earth's magnetosphere, showing the interaction with the solar wind, the bow shock, the magnetopause, the Van Allen radiation belts, the plasmasphere and the plasma sheet extending into the magnetotail [11].

For spacecraft that must continue operating during solar particle events, it's critical to account for the impact of both solar protons and solar heavy ions on the likelihood of single-event effects (SEEs). While solar heavy ions contribute minimally to total dose levels, they can cause severe SEEs because their flux during events can be orders of magnitude higher than the background levels from galactic cosmic rays. Peak flux conditions, though short-lived, can drive mission-critical design requirements. It's therefore essential to consider not just average conditions but also peak event intensities when defining operational constraints and radiation

risk assessment, due to their potential for disruption.

## 1.4 Trapped Radiation Belts

Radiation belts can develop around any planetary body with a sufficiently strong magnetic field capable of deflecting and capturing charged particles before they reach the atmosphere. These belts contain energetic particles from both the solar wind and lower-energy galactic cosmic rays. While planets such as Mercury, Venus and Mars lack significant magnetic fields and therefore do not exhibit radiation belts, others like Jupiter possess intense magnetic fields and complex belt systems far more powerful than Earth's.

Earth's radiation belts, known as the Van Allen belts, were discovered during the Explorer I mission. These toroidal regions are filled with trapped protons and electrons spiraling along the planet's magnetic field lines. The severity of radiation exposure from these belts depends on spacecraft orbit, solar activity and variations in the magnetosphere.

Both protons and electrons trapped in Earth's radiation belts play a significant role in the accumulation of total ionizing dose (TID) within spacecraft systems. In particular, energetic protons are capable of inducing single-event effects (SEEs) in sensitive electronics and also contribute to long-term degradation through non-ionizing energy loss (NIEL). Their high energy levels and strong penetration ability make them especially challenging to shield against.

Lower-energy electrons, on the other hand, can cause electrostatic discharge (ESD), which becomes a serious concern for spacecraft operating in high-altitude orbits like geostationary orbit (GEO), where exposure to electron-rich environments is more intense. Higher-energy electrons are even more problematic, they can penetrate spacecraft structures, accumulate in insulating materials and eventually discharge, potentially damaging internal electronics.

The shape and thickness of the radiation belts are not uniform. They are thickest near the equator, where the magnetic field lines run parallel to the Earth's surface and thin out toward the poles, where the field becomes perpendicular. The inner belt typically spans altitudes between approximately 0.2 to 2 Earth radii (McIlwain L shells= 1 to 3, related to magnetic field lines), while the outer belt ranges from 3 to 7 Earth radii, L=2.8 to 8.

The inner belt contains a dense population of protons with energies exceeding 10 MeV up to 400 MeV and electrons ranging from few keV to 10 MeV. In contrast, the outer belt is dominated by high energetic electrons and particle fluxes are highly variable and strongly influenced by solar activity.

Because radiation exposure is significantly heightened within these belts, mission planners aim to avoid or minimize time spent in these regions whenever possible.

Low Earth Orbits (LEOs), which lie well below the radiation belts, are considered relatively safe and exhibit much lower particle flux. Additionally, the belts themselves offer some shielding against galactic cosmic rays (GCRs), which partially offsets radiation exposure in LEO.

Interestingly, scientists have observed the temporary formation of a third, transient radiation belt, which periodically detaches from the outer belt and later dissipates. The traditional picture of Earth’s radiation environment consists of two concentric belts of charged particles: a stable inner belt dominated by protons and a highly dynamic outer belt dominated by relativistic electrons. This model was fundamentally revised following the launch of NASA’s Van Allen Probes mission in 2012, which provided high-resolution data enabling the observation and characterization of a transient third radiation belt or so-called “storage ring”. While transient in nature, these belts reveal fundamental aspects of particle transport and acceleration that are essential for space weather forecasting and satellite mission planning. The convergence of multiple independent studies, Pinto et al. (2018) [12], Hao et al. (2020) [13] and Baker (2021) [14], provides a comprehensive and compelling body of evidence confirming the physical reality and significance of three-belt configurations in the near-Earth space environment.

Pinto et al. (2018) [12] presented the first comprehensive statistical analysis of third-belt events based on five years of Van Allen Probes data. In their study, they identified 30 three-belt structures occurring also in presence of geomagnetic storms. These structures formed when a sudden depletion of the outer belt, typically due to enhanced solar wind pressure or CME-driven shocks, left behind a remnant population of ultra-relativistic electrons (around 5.2 MeV) between  $L = 2.8$  and  $L = 3.5$ . This remnant belt was subsequently isolated by the regeneration of the outer belt at higher  $L$ -shells ( $L > 4$ ), resulting in a distinct third belt. The longevity of these remnant belts was found to depend on the energy and location of trapped particles. Those located within the plasmasphere experienced slower decay due to reduced interactions with scattering waves, allowing these belts to persist for weeks or even months. The results confirm that the third belt is not a rare anomaly but a frequent and physically meaningful structure under specific magnetospheric conditions.

While previous observations focused on multi-MeV electrons, Hao et al. (2020) [13] extended the analysis to sub-MeV populations ( $< 600$  keV), revealing that three-belt configurations also occur in this lower energy regime. Their case study, focused on the September 2017 geomagnetic storms, showed a rapid formation and decay of a third belt lasting only 2–3 days. In this scenario, a remnant belt was again formed through partial dropout of the outer zone. However, due to the greater sensitivity of sub-MeV electrons to wave–particle interactions, especially with plasmaspheric hiss, the decay time was significantly shorter. The authors also observed “V-shaped” and “bump-on-tail” features in the energy spectra, indicating



complex acceleration and loss dynamics. Although short-lived, these belts exhibit the same basic morphological pattern and formation mechanism as their higher-energy counterparts, thus reinforcing the third-belt model as a general phenomenon across energy ranges.

Baker (2021) [14] offered a broader perspective on third-belt formation within the context of wave-particle interactions, particularly those triggered by solar events like CMEs and substorms. The paper highlighted how interactions between lower-band chorus waves and seed electrons (10–200 keV) can rapidly accelerate particles to relativistic and ultra-relativistic energies, generating and sustaining structures such as the storage ring. Through analysis of the March 2013 and March 2015 storm events, Baker showed that the third belt often survives the dramatic losses suffered by the outer belt following CME shocks. The persistent remnant is then encased between a depleted outer zone and a stable inner belt, completing the three-belt structure. Moreover, the existence of an "impenetrable barrier" near L 2.8 RE (Earth Radius) was found to confine relativistic electrons, contributing to the stability and inner boundary of the third belt.

Across all three studies, several consistent themes emerge:

1. **Formation Mechanism:** all authors agree that the third belt results from a two-step process: (1) dropout or loss of the outer belt population and (2) partial recovery forming a new outer belt while a remnant belt remains trapped closer to Earth.
2. **Energy Dependence:** while Pinto et al. (2018) [12] and Baker (2021) [14] focused on ultra-relativistic electrons ( $>2$  MeV), Hao et al. (2020) [13] demonstrated that even sub-MeV populations ( $\sim 600$  keV) exhibit similar three-belt dynamics, though with faster decay due to stronger wave-particle scattering.
3. **Wave-Particle Interactions:** chorus and hiss waves were identified as key mechanisms governing both acceleration and loss processes. Particularly, chorus waves accelerate seed populations, while hiss contributes to the decay of remnant belts, especially at lower energies.
4. **Geomagnetic Drivers:** CME-driven shocks and substorms consistently act as triggers for third-belt formation by modifying the global configuration of the magnetosphere and injecting seed particles.
5. **Persistence:** the remnant belt's stability is highly dependent on its location relative to the plasmasphere and the energy of the trapped electrons. Ultra-relativistic belts are more resistant to loss and can persist longer, especially when shielded within the plasmasphere.

Because the Earth's magnetic field is tilted by about 11 degrees from the rotational axis, the radiation belts don't line up perfectly with Earth's surface. This misalignment leads to an important phenomenon known as the South Atlantic Anomaly (SAA), a region off the coast of Brazil where the inner belt dips unusually close to Earth, down to altitudes of 200 to 800 km. While the particle fluxes and as consequence the radiation levels, in the SAA are lower than in deeper parts of the belt, they are much higher than elsewhere at similar altitudes. For instance, the International Space Station (ISS) receives most of its radiation dose while passing through the SAA.

Although the energy of trapped particles is lower than that of GCRs or SEPs, their sheer abundance makes them a major hazard. Prolonged exposure in these regions can damage electronics and pose risks to human health. For this reason, spacecraft are often routed to avoid the belts or limit exposure time. In some cases, onboard electronics are powered down during belt crossings to mitigate TID accumulation, especially in the presence of electric fields, which can worsen the effects of radiation.

The behavior of charged particles entering Earth's magnetosphere, either from the solar wind or from secondary processes such as neutron decay caused by cosmic ray interactions with the atmosphere, is largely controlled by Earth's magnetic field. Once within the magnetosphere, these energetic particles follow complex motions made up of three key components:

- Gyration around magnetic field lines due to the Lorentz force;
- Bounce motion, where the center of this spiraling movement travels up and down along the field lines (known as guiding center motion);
- Longitudinal drift, a slow movement of the guiding center around the planet: westward for ions and eastward for electrons.

Together, these motions produce spiral-like orbits along toroidal surfaces called drift shells, centered on Earth's magnetic dipole. Particles that become confined within these shells can remain trapped for extended periods, protons, for instance, may stay bound for years at altitudes of several thousand kilometers. These long-lived populations are what we refer to as trapped particles.

The majority of these stable, trapped particles consist of:

- Protons with energies between 100 keV and several hundred MeV;
- Electrons ranging from a few tens of keV up to 10 MeV.

There is also some observational evidence for a narrow region, located around one Earth radius in altitude, that contains trapped heavy ions. These ions are believed to be anomalous cosmic ray ions that have been decelerated and captured.

However, their concentrations are many orders of magnitude lower than those of protons in the same region.

High-energy protons (above 10 MeV) tend to be confined to low altitudes, whereas lower-energy protons ( $<1$  MeV) can reach much higher altitudes, including geosynchronous orbit. The spatial region where these particles are found narrows as energy increases and the zones of peak intensity shift inward toward Earth.

Electron populations follow a different pattern. They tend to concentrate in the two distinct regions, the inner belt and the outer belt. Between these two regions lies the slot region, a zone of relatively low particle density. The exact boundaries and structure of these belts depend heavily on electron energy. Higher-energy electrons are more tightly confined to the inner belt, while lower-energy electrons extend into the outer belt, sometimes beyond geosynchronous orbit. Notably, at high latitudes, the outer electron belt can reach much lower altitudes.

Our general understanding of the radiation belts relies heavily on NASA's AP-8 and AE-8 models, which provide average particle distributions. However, these models represent a static snapshot and it is well understood that the actual populations within the belts are highly dynamic, varying on multiple time scales.

One key source of this variability is the 11-year solar cycle. During solar maximum, increased solar irradiance causes Earth's upper atmosphere to expand. This expansion brings neutral atoms into regions of the belts where particles are trapped, resulting in increased particle loss, especially at low altitudes. This atmospheric drag effectively erodes the lower edges of the radiation belts, especially for protons. The erosion effect increases with decreasing altitude and the recovery of the population shows a phase lag which also depends on altitude.

Model outputs show that solar activity has different effects depending on the particle type and location. While the inner belt is generally stable, the outer belt is extremely dynamic, with variations of up to several orders of magnitude possible within hours, especially during periods of enhanced geomagnetic activity. The Van Allen radiation belts are inherently dynamic structures, shaped by a complex balance between particle acceleration and loss processes. Their variability, manifested through spectral hardening, boundary motion and energy-dependent spatial shifts, is influenced by internal magnetospheric dynamics and external drivers such as solar wind, geomagnetic storms and the solar cycle. Recent studies leveraging long-term satellite observations and advanced simulations have contributed significantly to our understanding of these variations.

A major advancement in quantifying radiation belt variability is the identification of a natural physical upper bound to electron flux levels, as articulated by Olifer et al. (2022) [15]. Through the analysis of 133 geomagnetic storms during the Van Allen Probes era, the authors observed a consistent spectral hardening of electron populations below 2.6 MeV, corresponding with the predictions of the Kennel-Petschek (KP) limit, a theoretical self-organizing process wherein increasing

wave growth (driven by flux anisotropy) induces pitch-angle scattering that prevents further particle accumulation. Crucially, their results showed that this energy-dependent cap was frequently reached for sub-MeV populations within hours of storm onset, whereas higher-energy electrons approached the limit only during the most extreme events. This finding reveals that radiation belt variability is not unconstrained but naturally regulated by wave–particle feedback mechanisms. The Kennel–Petschek (KP) limit describes how many electrons can be stably confined at a given location. This limit arises due to wave–particle interactions: when the flux of energetic electrons becomes too high, due to geomagnetic storms, their anisotropic distribution in pitch angle drives the generation and growth of plasma waves, particularly chorus waves. These waves, in turn, scatter the electrons into the loss cone (pitch angle scattering), causing them to precipitate into the atmosphere. This feedback mechanism creates a dynamic balance, higher fluxes generate stronger waves, which in turn enhance loss rates of electrons. As a result, the electron population self-limits: any further increase in flux beyond a certain threshold triggers more intense losses, effectively capping the maximum sustainable electron flux. This process is energy-dependent and plays a key role in shaping the spectral hardness and temporal evolution of the radiation belts during geomagnetic storms.

While the KP limit constrains flux magnitude, the spatial structure of the belts, particularly the slot region between the inner and outer belts, exhibits significant temporal and energy-dependent variability. Mei et al. (2021) [16] constructed an empirical model for the slot boundaries based on 2014–2018 Van Allen Probes data. Their analysis demonstrated that the upper and lower boundaries of the slot vary non-linearly with energy, with the lower boundary scaling logarithmically and the upper boundary governed by compression (Kp-dependent) and recovery (time-dependent) processes. They further found that slot refilling is energy-dependent: lower-energy electrons ( $<1$  MeV) can penetrate the slot more easily during geomagnetic disturbances, while higher-energy populations are constrained by plasmaspheric hiss and other loss mechanisms. The model they proposed reconstructs real-time boundary positions using only Kp and energy as inputs, making it a useful tool for operational risk assessment.

Saikin et al. (2021) [17] reconstructed the evolution of Earth’s electron radiation belts over eight complete solar cycles (1933–2017). The study provides several key evidences of variability:

- **Solar Cycle Dependence:** the reconstructed belts showed strong correlation with solar activity. Solar Cycle 24 (2008–2017), for instance, produced significantly weaker relativistic electron fluxes than any of the previous seven cycles. This confirms that low solar activity translates directly into suppressed radiation belt dynamics.

- CME vs. Corotating Interaction Regions (CIR) Dominance: the analysis revealed that CME-driven storms, more prevalent during solar maxima, caused intense but short-lived flux enhancements, while CIR-driven storms, common during solar minima, produced moderate but sustained enhancements, contributing to prolonged outer belt persistence.
- Upper L-shell Sensitivity: the simulation showed that variability at  $L > 5.5$  was most affected by the solar cycle, with deep belt penetration into lower L-shells occurring only during stronger cycles. In contrast, during Cycle 24, outer belt enhancements rarely reached  $L < 4.5$ , demonstrating spatial suppression under weak geomagnetic forcing.

This reconstruction highlights how electron flux enhancements and depletions vary depending on the solar cycle phase (ascending, maximum, declining) and the type of geomagnetic disturbances (CME-driven vs. CIR-driven). Their reconstruction confirms that Solar Cycle 24 is an outlier in terms of radiation belt weakness and should not be used as a reference for worst-case environment models. The results reinforce the necessity of incorporating solar-cycle-aware dynamics into predictive frameworks and demonstrate that historical geomagnetic indices (like Kp) can be effectively used to model belt evolution over decadal timescales.

Adding further detail to short-term variability, Shi et al. (2020) [18] analyzed Van Allen Probes data during 37 geomagnetic storms and documented the evolution of the inner boundary of the outer radiation belt. Their observations revealed that this boundary exhibits two dominant morphologies: a V-shape during the main phase of storms (associated with kappa-like energy spectra) and an S-shape during recovery (indicating reversed energy spectra or “bump-on-tail” distributions). This morphological transformation is strongly energy-dependent, typically starting at 100–550 keV and occurs predominantly within the plasmasphere. The position and energy threshold of the transition also correlated with storm intensity (SYM-H index), emphasizing the role of geomagnetic forcing in reshaping belt boundaries. These structural features reflect complex interplay between substorm injections, chorus wave acceleration and scattering by plasmaspheric hiss.

All studies agree that radiation belt dynamics are inherently energy-dependent and variability manifests across both spatial and temporal domains. From the self-regulation of maximum fluxes [15], to dynamic slot and belt boundary motion [16] and [18] and long-term solar modulation [17], the literature demonstrates that no single process governs radiation belt behavior. Instead, a hierarchy of coupled mechanisms: energy-dependent acceleration, transport and loss processes. This variability is shaped by short-term geomagnetic activity, long-term solar cycles and internal feedback mechanisms. In summary:

- The electron flux is naturally limited by a self-regulating mechanism known as the Kennel–Petschek limit. During geomagnetic storms, low-energy electrons

(100 keV) reach this limit within a few hours, while higher-energy fluxes ( $<2.6$  MeV) increase but never exceed the predicted physical cap.

- The slot region narrows during periods of high Kp (strong geomagnetic activity), due to the compression of its upper boundary. It gradually expands during quiet times as acceleration mechanisms weaken and recovery processes dominate.
- Electron fluxes are lower and less variable during weak solar cycles (e.g., Solar Cycle 24), with few deep penetrations of the outer belt. In contrast, strong solar cycles produce higher fluxes and deeper penetration toward lower L-shells.
- The inner edge of the outer radiation belt exhibits a V-shaped structure during the storm's main phase (due to the penetration of hundreds of keV electrons) and returns to an S-shape during the recovery phase, when loss mechanisms dominate and reduce low-energy fluxes.

As it is well being underlined, proton and electron fluxes in Earth's radiation belts are strongly influenced by solar activity, especially during solar energetic particle (SEP) events triggered by solar flares and coronal mass ejections (CMEs). Although both protons and electrons are accelerated by similar processes, their behavior relative to solar activity can differ markedly.

In the inner radiation belt, the main source of trapped protons originates from neutron decay, neutrons produced when cosmic rays interact with Earth's atmosphere. The rate of neutron production and thus trapped proton generation, is closely tied to cosmic ray flux, which itself depends on solar activity. During periods of high solar activity (solar maximum), the intensified solar wind and magnetic field form a stronger barrier against incoming cosmic rays, leading to fewer cosmic rays reaching the atmosphere. This results in a reduction of secondary neutrons and, consequently, a lower population of trapped protons in the inner belt. Thus, inner belt proton fluxes are anti-correlated with the solar cycle, as proved in [3] and [8]: they are higher during solar minimum and lower during solar maximum. The anti-correlation is not instantaneous; there may be a lag (months to years) between changes in galactic cosmic rays (GCRs) and the buildup/depletion of trapped protons. This delay arises due to neutron decay timescales and loss processes (e.g., scattering with plasmaspheric hiss waves). While neutron decay is the dominant source of protons in the inner belt, at higher altitudes (outer belt), protons can also originate from other processes, such as acceleration during geomagnetic storms. These findings, about the proton belt, represent a general conclusion drawn from studies reported in [19], [20] and [21].

Meanwhile, the behavior of electrons in the outer radiation belt is very different. This population is highly dynamic and heavily influenced by geomagnetic storms and

substorms driven by disturbances in the solar wind [22]. During solar maximum, the frequency and intensity of geomagnetic storms increase, injecting and accelerating electrons from the magnetotail into the outer belt. As a result, electron fluxes in the outer belt are positively correlated with solar activity: higher solar activity leads to stronger electron populations, as proved in [3] and [8].

This contrasting behavior, inner belt protons decreasing and outer belt electrons increasing with solar activity, is crucial to consider when modeling the radiation environment for mission planning, particularly in worst-case scenario analyses.

In addition to variations driven by solar activity, the low-altitude trapped particle environment is gradually evolving due to secular changes in Earth's magnetic field. Over time, the center of the planet's geomagnetic dipole is drifting away from the geographic center at a rate of about 2.5 km per year, as reported in [8] and the overall strength of the magnetic moment is slowly declining. Together, these changes cause the inner edges of the radiation belts to migrate inward.

One consequence of this drift is the formation of a local weakening of the magnetic field at low altitudes, giving rise to the SAA. Outside of the SAA, proton fluxes at these altitudes are negligible. However, electron fluxes can become significant at high latitudes, where field lines from the outer belt dip down closer to Earth. Moreover, the SAA itself is slowly drifting westward, at an estimated rate of about 0.3 degrees per year [8], a movement that must be accounted for in long-duration satellite missions.

At lower altitudes, typically below 2,000 kilometers, trapped charged particles begin to interact with the neutral atmosphere. For trapped protons with energies greater than 1 MeV, the size of their gyroradius becomes comparable to the atmospheric scale height. As these protons spiral along magnetic field lines, they pass through regions of varying atmospheric density depending on their position during each rotation. Consequently, the proton flux at a given location depends not only on energy but also on the arrival direction relative to the local magnetic field and the particle's pitch angle. This leads to an asymmetry known as the East-West effect [8], where proton fluxes arriving from different azimuths can differ by factors of three or more. This angular dependence is an important feature when calculating the integrated proton flux experienced by a satellite along its orbit.

Beyond the slow, long-term trends in trapped particle populations, short-term variations are also significant. In the outer radiation belt, for instance, electron fluxes can fluctuate by several orders of magnitude within just a few hours. Data collected by the Combined Release and Radiation Effects Satellite (CRRES), as described in [8] and [23], revealed that both the intensity and spatial distribution of outer belt electrons can change dramatically, often in response to variations in magnetospheric activity. CRRES measurements also showed that magnetic storms can heavily impact the trapped proton population, as discussed in this chapter.

The ability of energetic particles to enter the magnetosphere from outside is

fundamentally limited by Earth's magnetic shielding. Whether a particle can penetrate to a specific point depends on its rigidity, the ratio of its momentum to its charge. For every location and every possible approach direction, there is a geomagnetic cutoff rigidity: a threshold below which particles cannot penetrate. Since the cutoff rigidity varies with arrival direction, the geomagnetic transmission (the probability that a particle of a given energy can reach a location) must be averaged over all possible directions. For a particular particle energy, the attenuation factor, the fraction of incoming flux allowed through, is calculated by integrating over solid angle and normalizing by  $4\pi$  [8]. This factor, when multiplied by modeled interplanetary proton fluence and integrated over the spacecraft's orbit, determines the effective exposure time to energetic particles.

During magnetic storms, the geomagnetic cutoff can shift, temporarily lowering the energy threshold for particle penetration. This allows lower-energy particles, normally excluded, to enter regions of the magnetosphere they wouldn't typically reach. Solar events, though not always accompanied by magnetic storms, often trigger them. In fact, the variability of the near-Earth space environment is largely driven by two major forces: solar storms and magnetic storms.



## Chapter 2

# Interaction of Radiation with Matter

A comprehensive understanding of how radiation affects spacecraft requires insight into the fundamental processes governing interactions between particles and matter. Once the radiation environment was characterized in the previous chapter, this section focuses specifically on electronic materials and systems, though many of the principles discussed also apply to other materials. The technical framework adopted in this chapter have been developed primarily based on the guidance and models provided in references [2] and [6], which served as foundational sources for interpreting radiation-matter interaction mechanisms in the context of space electronics.

Radiation refers to the transfer of energy via photons, electrons, ions, muons or nucleons (such as protons and neutrons). In the early 20th century, it became evident that particles at the quantum scale could exhibit both wave-like and particle-like characteristics, a concept known as wave-particle duality. This duality means that a particle's wavelength is inversely related to its momentum or, equivalently, to the square root of its kinetic energy. As a particle's energy increases, both its velocity and momentum rise accordingly, while its associated wavelength becomes smaller. This relationship is critical, because the wavelength of an incoming particle determines what kinds of interactions it can undergo with matter. Although radiation traveling through a perfect vacuum moves unimpeded and defines much of the space radiation environment, it is the interaction between radiation and materials that ultimately gives rise to the radiation effects that concern spacecraft electronics.

When a flux of energetic particles strikes a material, referred to as the target, each particle can experience one of three possible outcomes:

- (a) The particle may pass through the material without any interaction at all,

emerging from the opposite side completely unchanged, with no loss of energy or change in direction.

(b) The particle may interact with the target, losing a portion of its kinetic energy through numerous small collisions. As a result, it exits the material with a lower energy and a deflected trajectory.

(c) The particle may be fully absorbed within the material, losing all of its energy inside the slab and failing to exit the target.

Radiation exists in many forms, including electromagnetic waves and various types of energetic particles. Electromagnetic radiation is characterized by three fundamental properties: frequency, wavelength and photon energy, with photons being the basic particles of electromagnetic energy. The wavelength and frequency are inversely related: longer wavelengths correspond to lower frequencies and lower photon energies, while shorter wavelengths are associated with higher frequencies and higher photon energies. The way electromagnetic waves interact with matter strongly depends on their wavelength.

The electromagnetic spectrum is typically divided into broad categories based on wavelength: radio waves, microwaves, infrared, visible light, ultraviolet, X-rays and finally, at the shortest wavelengths and highest energies, gamma rays. In the context of microelectronics, especially in industrial, medical and defense applications, the main concern regarding electromagnetic radiation usually focuses on X-ray and gamma-ray exposures. Lower-frequency radiation such as radio waves or electromagnetic interference (EMI) is generally not problematic, thanks to standardized shielding practices in commercial design, packaging and layout techniques and therefore is not discussed further here.

Beyond electromagnetic radiation, space environment also presents a variety of particle radiation. These include different atomic and subatomic particles, encountered naturally or in man-made settings. The primary types of particle radiation ordered from largest to smallest, are heavy and light ions (ionized atoms), nucleons (protons and neutrons) and electrons. When energetic particles encounter a material, several different outcomes are possible, ranging from complete transmission with no interaction, to full absorption within the material. The actual result depends on the interactions between the incoming particle and the electrons and nuclei of the target atoms, as illustrated in Figure 2.1. Diagram illustrating the possible outcomes when particle radiation strikes a thin slab of material

In some cases, particularly when the thickness of the target slab is small compared to the typical range of the incoming particle, the particle can pass through the material without undergoing any interactions at all, resulting in full transmission. A good example is neutrinos: these chargeless and nearly massless particles interact so weakly with matter that they can travel through massive amounts of dense material without interacting, making them irrelevant from a microelectronics reliability perspective. On the other end of the spectrum, alpha particles, which are much

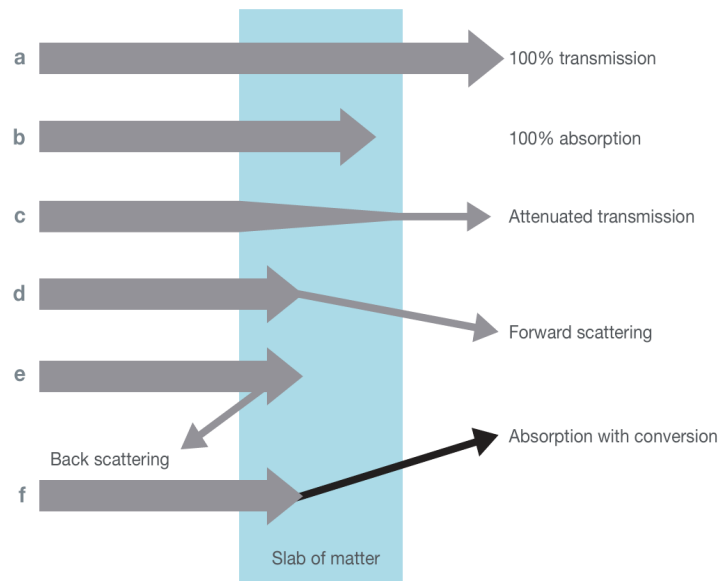


**Figure 2.1:** Diagram illustrating the possible outcomes when particle radiation strikes a thin slab of material [6].

heavier and carry an electric charge, are easily absorbed; even a thin sheet of paper is enough to stop them completely. The degree of attenuation, reduction in particle flux, depends on two mechanisms: direct absorption of the particle within the material and collisions with the electrons or nuclei of the target atoms.

As a result of these interactions, some particles are scattered, that is, deflected from their original path. The angle of scattering depends on several factors, including the particle's energy, its incident angle and the material properties of the target. Broadly speaking:

- If a particle is scattered back in the direction it came from, it is called back-scattered.
- If it continues moving forward but at a different angle, it is considered forward-scattered (as illustrated in Figure 2.1-e).
- In some cases, the incident particle itself may be absorbed and a different particle type may be emitted instead, through a nuclear or subatomic transformation (see Figure 2.1-f).

Looking more closely, for photons, some interactions involve complete absorption in a single event, for instance, the creation of a single electron-hole (e-h) pair. However, for ions, nucleons and electrons, most interactions involve a gradual loss of energy through many small collisions with the material's atoms. It typically takes multiple successive collisions for an energetic particle to fully dissipate its kinetic energy and come to rest.

The distance travelled between each collision is known as the free path, while the average distance between all collisions is referred to as the mean free path. A higher probability of interaction shortens the mean free path, meaning the particle loses more energy over a smaller distance and its overall range within the material becomes shorter.

This behavior is closely tied to the density of the material:

- In denser materials, particles experience more frequent interactions, leading to a shorter mean free path and reduced range.
- In less dense materials, particles can travel farther between interactions.

Since energy loss occurs gradually through numerous small interactions rather than one major collision, each particle's journey is stochastic, subject to randomness, resulting in variations known as range straggling. This means that even particles of the same type and energy can follow slightly different paths and lose energy at different rates as they pass through a material. Ultimately, if the thickness of the target is greater than the average range of the particles, most will be absorbed before exiting the slab.

At the core of all scattering and absorption processes lies the fundamental concept of particle collisions. These collisions are the primary way radiation interacts with matter. In general, collisions can be classified as either elastic or inelastic, depending on how energy is exchanged during the interaction. While in reality most collisions involve a mix of elastic and inelastic effects, they are typically categorized based on which form of energy transfer dominates. In an elastic collision, the incident particle and the target particle interact and then separate without any creation, destruction or transformation of particles. No energy is lost to internal excitations or radiation; instead, the total kinetic energy and momentum of the system are conserved. Although the individual energies of the particles may change after the collision, the combined kinetic energy and momentum before and after the interaction remain constant. By contrast, in an inelastic collision, the total kinetic energy is not conserved. A portion of the initial kinetic energy is converted into other forms, such as excitation energy, radiation or even the creation of new particles. In inelastic processes, the incoming and outgoing particles may differ: for example, the incoming particle might be absorbed by the target, leading to nuclear reactions or fragmentation.

A typical example is a nuclear reaction where an incoming neutron or proton is absorbed by an atomic nucleus. The kinetic energy and mass of the incoming particle contribute to the excitation of the nucleus, which then de-excites by emitting secondary particles or by breaking apart into fragments. In such cases, some of the system's initial kinetic energy is "used up" to facilitate these changes, fundamentally altering both the energy distribution and the particle makeup of the system.

In essence, particle interactions with matter are fundamentally about energy transfer, where energetic particles lose energy to the material they pass through. These interactions can take many forms, depending on the type of particle, its energy and the physical properties of the material involved. The key point is that radiation dissipates energy into matter through a variety of interaction processes. In some cases, a particle may deposit all of its energy in a single interaction, being completely absorbed in one event. More often, however, energy loss occurs gradually over many successive interactions, with the particle slowly losing kinetic energy until it eventually comes to rest within the material.

The rate of energy loss per unit distance directly affects how far a particle can travel:

- Particles that lose energy quickly have shorter ranges.
- Particles with higher initial energies can penetrate farther before coming to a stop.
- In denser materials, where more interaction sites are available, particles

experience more frequent collisions, leading to greater energy loss over shorter distances and thus a reduced range.

For microelectronic devices, this energy transfer presents a critical challenge. Most of the energy deposited by radiation gets converted into electrical charge. Since the correct operation of microelectronics relies on carefully controlling the generation, movement and storage of charge, any excess or non-equilibrium charge produced by localized radiation events can disrupt device function. These disruptions may manifest as transient errors (brief malfunctions) or as more persistent shifts in circuit behavior, leading to parametric changes or even functional failures over time.

## 2.1 Photon Interactions

Photons are the basic units of electromagnetic radiation, encompassing a wide range of wavelengths and energies, from long-wavelength radio waves to high-energy gamma rays. Being electrically neutral, photons do not experience the same interactions as charged particles, which significantly influences how they interact with matter.

There are three primary ways in which photons lose energy when passing through a material: the photoelectric effect, Compton scattering and pair production, as illustrated in Figure 2.2. Each of these mechanisms depends on the energy of the photon and the atomic structure of the material it encounters.

When an incident photon has enough energy to liberate an electron from its valence band or bound state, the photon is completely absorbed in the process, transferring all of its energy to the electron. The result is an excited photoelectron and the creation of a positively charged vacancy, often referred to as a hole.

At even higher photon energies, the photon can interact and excite tightly bound inner-shell electrons instead. In such cases, when an outer-shell electron subsequently fills the vacancy left behind, i.e. created during the original photon absorption event, a secondary X-ray photon, called a characteristic X-ray, is emitted. The energy of this secondary X-ray is unique to the specific element, reflecting the difference in energy between the involved electron shells. This phenomenon, known as the photoelectric effect, is an inelastic interaction because the photon's energy is entirely consumed in exciting or ejecting an electron. The amount of energy transferred is directly proportional to the frequency of the photon, higher-frequency (and thus shorter-wavelength) photons carry more energy.

If a photon's energy is too low to excite or free an electron, meaning it cannot generate an electron-hole pair, then the material appears transparent to that photon and it will pass through without any interaction. The likelihood of a photoelectric interaction occurring depends strongly on the relationship between

the incoming photon's energy and the binding energy of electrons in the target material. In materials like silicon, the photoelectric effect dominates the interaction between photons and matter across a wide range of photon energies—from optical wavelengths up to X-rays around 100 keV.

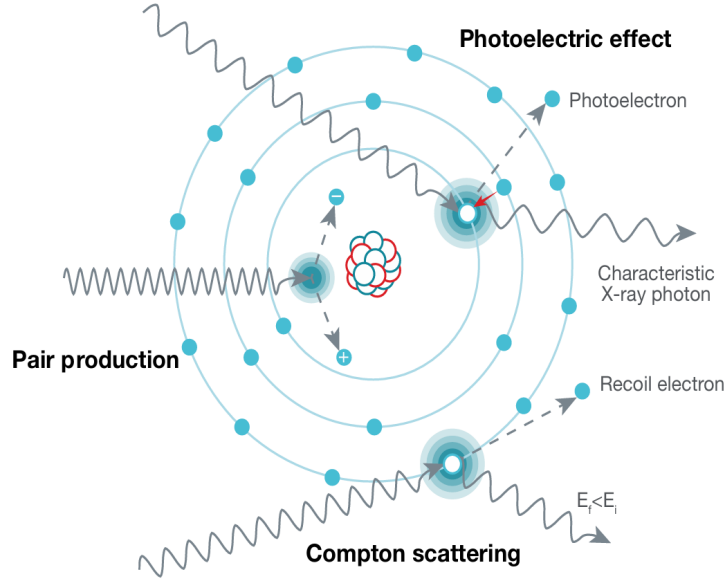


**Figure 2.2:** The three primary mechanisms by which photons lose energy when interacting with matter: the photoelectric effect, Compton scattering and pair production [6].

The three primary mechanisms by which photons lose energy when interacting with matter: the photoelectric effect, Compton scattering and pair production

At higher photon energies, a different interaction mechanism becomes dominant. In Compton scattering, the incoming photon collides with a single electron, transferring part of its energy to the electron and losing some of its own in the process. This interaction produces a recoil electron and a scattered photon, which travels in a new direction with reduced energy (and thus a lower frequency) compared to the original photon. Depending on how much energy is transferred, the impacted electron may either be promoted to a higher bound state or, if the energy transferred exceeds its binding energy, the electron may be ejected entirely, gaining enough kinetic energy to interact with other atoms or electrons in the material.

At even higher photon energies, another process called pair production becomes possible and eventually dominates the energy-loss mechanisms for high-energy gamma rays. In pair production, a gamma-ray photon interacts with the electric field of a nucleus and transforms into two particles: an electron and a positron (the

electron's antiparticle, with a positive charge). For pair production to occur, the photon's energy must be at least equal to the total resting mass of the two particles created. Any excess energy is distributed as kinetic energy between the newly formed electron and positron. Below the threshold energy, pair production cannot happen; once the threshold is crossed, the likelihood of pair production increases with rising photon energy. Furthermore, the probability of pair production scales approximately with the square of the atomic number ( $Z$ ) of the target material, meaning heavier, denser nuclei are much more effective at absorbing gamma rays through this process.

These three mechanisms, the photoelectric effect, Compton scattering and pair production, collectively determine how much of an incoming photon beam is absorbed or transmitted through a material. As the beam passes through the material, its intensity decreases exponentially based on the attenuation coefficient, which is expressed in units of  $\text{cm}^{-1}$ . The attenuation coefficient depends on both the energy of the photons and the composition of the material, as different mechanisms dominate at different energy levels.

Often, it's more practical to use the mass attenuation coefficient, which is the linear attenuation coefficient divided by the material's density, expressed in units of  $\text{cm}^2/\text{g}$ . The mass attenuation coefficient provides a clearer comparison between different materials. Figure 2.3 illustrates the mass attenuation coefficient of silicon as a function of photon energy, highlighting how the total absorption behavior results from the combined contributions of the three primary photon energy-loss mechanisms.

Plot of the total mass attenuation coefficient as a function of photon energy, highlighting the contributions from the three main energy absorption mechanisms: the photoelectric effect, Compton scattering and pair production.

Since most microelectronics are encapsulated in opaque packages (plastic, ceramic and/or metal), photons in the visible spectrum are typically not a concern. Photons of higher energy, such as X-ray and gamma photons, can easily penetrate packaging materials and are thus the primary photons of concern from the microelectronics point of view. However, in the space environment, direct fluxes of X-rays and gamma rays are generally minor compared to the radiation levels produced by other particle sources.

## 2.2 Electron Interactions

Electrons interact with matter primarily through the Coulomb force, engaging with both atomic electrons and nuclei within the target material. These interactions result in energy loss and directional changes, with or without the emission of a photon.



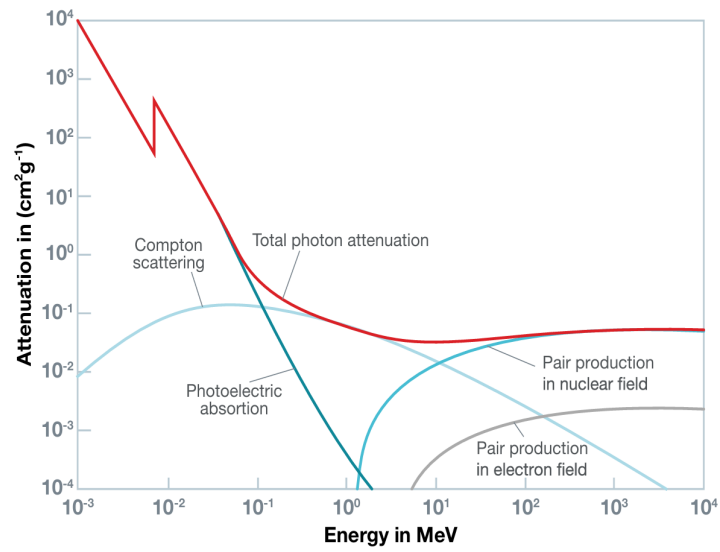


**Figure 2.3:** Plot of the total mass attenuation coefficient as a function of photon energy, highlighting the contributions from the three main energy absorption mechanisms: the photoelectric effect, Compton scattering and pair production [6].

In electron-electron interactions, as two negatively charged electrons approach each other, the repulsive Coulomb force between them increases sharply. This growing repulsion causes the incoming electron to be deflected from its original path, while the target electron typically remains bound to its atom. As a result, the incident electron exits the collision region at a different angle.

In contrast, during an electron-nucleus interaction, the situation is reversed: a strong attractive force develops between the negatively charged electron and the positively charged atomic nucleus as they get closer. This attraction causes the electron to decelerate and deviate from its original trajectory. Due to the large mass difference, the nucleus remains largely unaffected by the encounter, while the electron's path is altered significantly.

In some instances, the incoming electron may carry enough energy to displace a nucleus from its position within the atomic lattice, causing displacement damage. However, ionization, energy loss due to interactions with atomic electrons, is far more common than displacement events.

Both electron-electron and electron-nucleus interactions are classified as types of scattering and the main categories of electron scattering are illustrated in Figure 2.4.

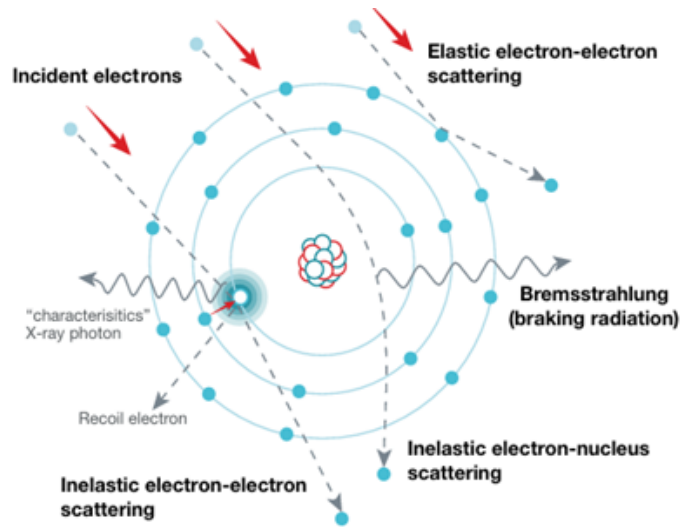


**Figure 2.4:** Diagram of the three primary mechanisms for electrons interacting with matter: elastic electron-electron, inelastic electron electron and inelastic electron-nucleus scattering [6].

The two most common interaction types for electrons traveling through matter are electron-electron scattering and electron-nucleus scattering. In electron-electron collisions, because both particles have relatively small mass, the resulting scattering

angles, the angle between the electron's incoming and outgoing paths, tend to be smaller compared to electron-nucleus collisions. In contrast, electron-nucleus interactions often produce larger scattering angles and are typically associated with inelastic processes, where part of the incident electron's energy is lost to excitation or radiation.

The scattering behavior during electron-nucleus interactions is heavily influenced by the atomic number ( $Z$ ) of the target material. Higher- $Z$  materials, with their greater electron densities, enhance the probability and severity of scattering events.

In an inelastic electron-electron collision, the incoming electron transfers part or sometimes all, of its kinetic energy to a bound target electron, exciting it to a higher energy state. If the transferred energy is sufficient to eject an inner-shell electron, it creates a vacancy. This vacancy is quickly filled by an electron from a higher energy level, releasing a photon whose energy corresponds to the difference between the two energy states. In elements with high atomic numbers, the emitted photon typically falls within the X-ray range, producing a characteristic X-ray similar to those generated by the photoelectric effect. In lighter elements (low- $Z$  materials), where electrons are more weakly bound, the energy released during these transitions often falls within the visible spectrum instead of the X-ray range.

In some cases, if a target electron gains enough energy, it may become unbound, effectively freed from its atom and can, if sufficiently energized, trigger additional ionizations before eventually losing energy and being recaptured.

Another important inelastic process involves Bremsstrahlung or braking radiation, i.e. direct emission of a photon. As an incoming electron is attracted to a nucleus, it experiences direction change by decelerating, causing it to emit part of its kinetic energy in the form of a photon. The closer the electron passes to the nucleus, the stronger the electrostatic force it experiences, resulting in greater deceleration and the emission of higher-energy photons. Because there are many possible trajectories and encounter distances, Bremsstrahlung radiation exhibits a continuous spectrum of photon energies, with the maximum photon energy limited by the initial kinetic energy of the incident electron.

Figure 2.5 presents the range of electrons in silicon (blue curve) and tungsten (red curve) as a function of their kinetic energy, illustrating how material properties affect electron penetration.

Because most microelectronic components are enclosed within opaque packaging materials, only high-energy electrons, those with kinetic energies greater than approximately 300 keV, are capable of penetrating the package and reaching the sensitive internal die.

In space environments, electron fluxes can be particularly intense, especially inside radiation belts, where the density of energetic electrons is significantly elevated. Given these energetic environment, the likelihood to encounter electrons is greater, in order to easily penetrate packaging materials and deposit energy

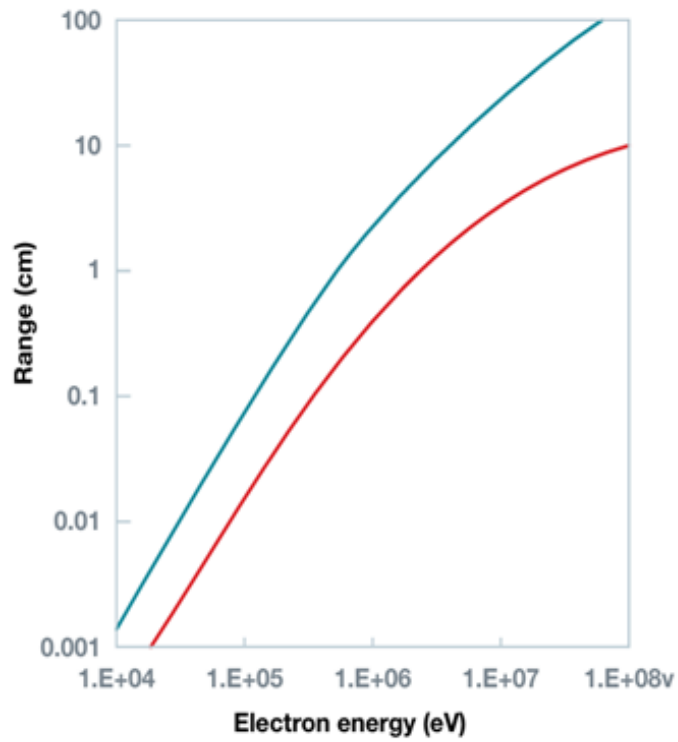


**Figure 2.5:** Electron range as a function of energy in silicon (blue curve) and tungsten (red curve). Due to tungsten's higher density and greater atomic number ( $Z$ ) compared to silicon, electrons have a significantly shorter range in tungsten [6].

within the device, leading to total ionizing dose (TID) effects that can degrade the performance and reliability of electronic systems over time.

## 2.3 Nucleons and Nuclear Reactions

Nucleons, comprising protons and neutrons, are the fundamental components of atomic nuclei. Although they are nearly identical in mass, the proton carries a positive electric charge, while the neutron is electrically neutral. This key difference significantly affects how these particles interact with matter.

Because neutrons carry no electric charge, they do not experience Coulomb interactions as they pass through matter. This means that neutrons are unable to cause direct ionization while traveling through a material. Instead, the only way neutrons can lose energy is through nuclear reactions, which can be either elastic or inelastic in nature. Due to the limited number of interactions they undergo, neutrons are highly penetrating particles, capable of traveling significant distances through matter before interacting. As illustrated in Figure 2.6, the two primary ways neutrons interact with materials are via elastic collisions, where the neutron scatters off a nucleus and inelastic collisions, where the neutron is absorbed or excites the nucleus, often leading to the emission of secondary radiation.

In an elastic nuclear reaction, a neutron collides with a target nucleus, transferring a portion of its kinetic energy to the nucleus before continuing on with reduced energy. From the perspective of microelectronics, if the neutron transfers enough energy, typically at neutron energies exceeding 100 keV, the nucleus can be displaced from its original lattice position, becoming a recoil nucleus.

In semiconductor devices, these displaced atoms can create localized defects in the crystal structure, leading to dramatic changes in the electrical properties of the material. As neutron or proton impacts accumulate over time, these individual displacements combine to produce what is known as displacement damage dose (DDD). Furthermore, once a nucleus is knocked out of its lattice position, it often loses some of its electrons, becoming a heavy charged ion. As this recoil nucleus moves through the material, it generates substantial direct ionization, contributing additional disruption. Each recoil nucleus, therefore, has the potential to trigger single-event effects (SEEs), which can compromise device functionality.

In contrast, inelastic nuclear reactions occur when the incident neutron is absorbed by the target nucleus, with the neutron's mass and energy being converted into nuclear excitation. This highly excited nucleus may then release its excess energy through various secondary processes, such as the emission of radiation or fragmentation into lighter particles.

The excess energy released after an inelastic nuclear reaction is emitted through one of four primary pathways, depending on the energy of the incoming neutron

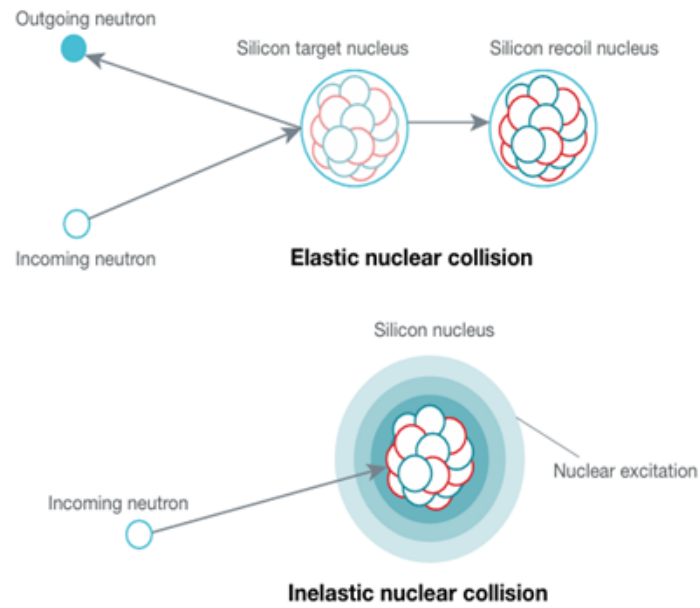


**Figure 2.6:** Elastic (top) and inelastic (bottom) nuclear reactions between an energetic neutron and a silicon target nucleus. In an elastic collision, the neutron "bounces" off the nucleus without being absorbed, transferring some energy and creating a recoil nucleus. In an inelastic collision, the neutron is absorbed by the nucleus, leaving it in a highly excited state [6]

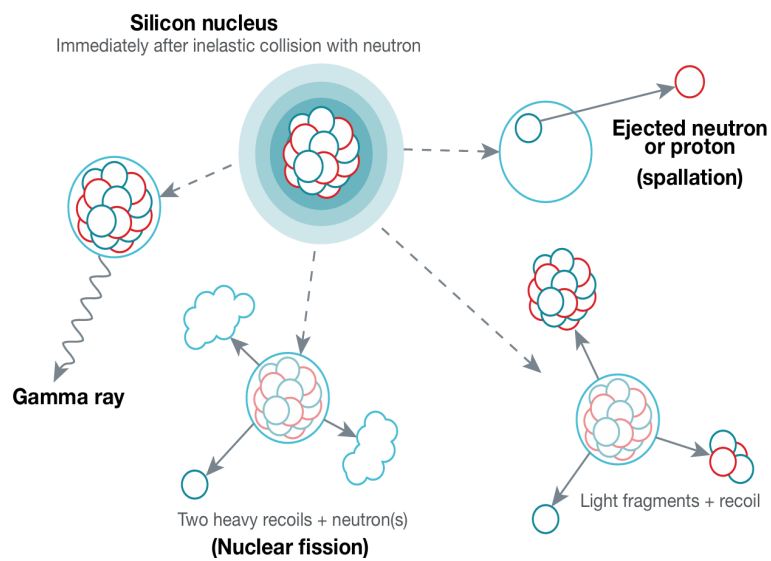


**Figure 2.7:** Immediately following an inelastic nuclear reaction, the nucleus remains in a highly excited state. It subsequently releases its excess energy through one of four possible pathways [6]

and the nature of the target nucleus:

At low neutron energies, typically up to a few tens of kiloelectron volts, the incident neutron is usually captured by the nucleus. The resulting excess energy is then released in the form of gamma-ray photons.

When the neutron energy lies between roughly one and several tens of mega-electron volts, the absorbed energy is generally distributed among all the nucleons inside the nucleus. In response, the nucleus typically breaks apart, ejecting one or more light fragments (such as nucleons or light ions) along with gamma-ray emissions. The emitted fragments typically carry kinetic energies in the MeV range and can cause direct ionization, making them a major contributor to single-event effects (SEEs) in microelectronics. An exception to this are secondary neutrons produced in the breakup, which themselves are not directly ionizing, but can lead to secondary nuclear reactions that do produce ionizing radiation.

In certain cases, particularly with specific heavy elements, the nucleus undergoes nuclear fission, splitting into two recoil fragments of nearly equal mass while emitting one or more neutrons. Nuclear fission is the same process that underpins nuclear reactors. However, in the context of microelectronics, materials that can undergo fission are present only in trace impurity levels (parts per billion), making fission an insignificant contributor to total ionizing dose (TID) or SEE concerns.

At very high neutron energies, above approximately 100 MeV, the neutron's wavelength becomes small enough that it no longer interacts with the nucleus as a whole. Instead, it transfers most or all of its energy to an individual nucleon inside the nucleus. This leads to a reaction known as spallation, where a single high-energy nucleon is ejected. The ejected particle can then travel through the material, potentially triggering additional nuclear reactions and contributing further to radiation effects.

Although protons and neutrons have nearly identical masses, they behave quite differently when interacting with matter because protons carry a positive electric charge. In addition to causing many of the same nuclear reactions as neutrons, protons can also engage in Coulomb interactions, allowing them to directly ionize materials.

While the amount of charge generated by protons in typical device-sensitive volumes is relatively small, in advanced digital circuits, especially those with very low critical charge thresholds, proton-induced single-event effects (SEEs) have been observed. Protons, being positively charged, are attracted to electrons but repelled by other positively charged nuclei. At proton energies below 50 MeV, Coulombic forces dominate, meaning that protons are generally repelled from nuclei before a nuclear reaction can occur. However, when proton energies exceed 50 MeV, they possess enough kinetic energy to overcome the repulsive Coulomb barrier, allowing nuclear interactions similar to those triggered by neutrons.

For microelectronics applications, understanding the fluence, the number of



particles per area and energy spectrum of incident protons or neutrons, along with the corresponding nuclear reaction cross-section, enables predictions of the number of nuclear interactions likely to occur within a given material. This information is essential for estimating single-event rates and evaluating radiation doses within sensitive components.

In the space environment, protons represent one of the most significant radiation threats. A considerable fraction of spaceborne protons have sufficient energy to penetrate shielding and packaging materials, depositing substantial energy directly into microelectronic systems. As a result, protons are a major source of SEEs in space-based electronics and at high enough fluences, they can also contribute to total ionizing dose (TID) and displacement damage dose (DDD) effects.

On Earth, neutrons are the primary concern at altitudes ranging from sea level to flight altitudes. The natural terrestrial neutron spectrum, created when cosmic-ray protons interact with the atmosphere, includes neutrons with energies ranging from tens to hundreds of MeV. These high-energy neutrons are capable of causing significant SEEs in terrestrial applications. However, because neutron fluences at ground level are relatively low over typical product lifetimes, TID and DDD effects from terrestrial neutrons are generally not a major concern for most electronic systems.

## 2.4 Ion Interactions

Ions are energetic particles that consist of atomic nuclei stripped of some or all of their electrons, resulting in a net positive charge. These particles, which include both light and heavy ions, travel at high velocities defined by their kinetic energy and interact with matter primarily through two mechanisms: electronic interactions, where energy is transferred to atomic electrons and nuclear interactions, which involve collisions with atomic nuclei.

As an ion penetrates a material, it continuously loses kinetic energy by ionizing surrounding atoms and displacing nuclei. This energy deposition process is characterized by the linear energy transfer (LET), which quantifies the amount of energy imparted per unit distance traveled. A representative simulation of the LET for a Xenon ion passing through Silicon, as a function of the ion's energy, is shown in Figure 2.8. At higher ion energies, the LET is dominated by electronic stopping, where energy loss occurs via direct ionization of the material. In contrast, at lower ion energies, a second, smaller peak appears, corresponding to nuclear stopping, where energy is lost due to displacement of target nuclei.

As the ion moves through the material, it continually loses kinetic energy, gradually slowing down as it undergoes multiple elastic and inelastic collisions with both electrons and nuclei. Because of their positive charge, energetic ions are

highly effective in ejecting nearby electrons from their orbits, creating a dense trail of electron-hole pairs along their path.

Heavier ions, which carry more positive charge, are significantly more efficient at causing direct ionization. In fact, at any given energy, heavier ions generate more charge over a given distance than lighter ions, resulting in a higher LET. Additionally, energetic ions also interact directly with atomic nuclei. As a charged ion approaches an atom, its electric field is partially screened by the atom's bound electrons, which reduce the Coulomb repulsive force between the ion and the nucleus. However, as the ion comes closer, this screening effect diminishes and the full repulsive force between the ion and nucleus becomes significant.

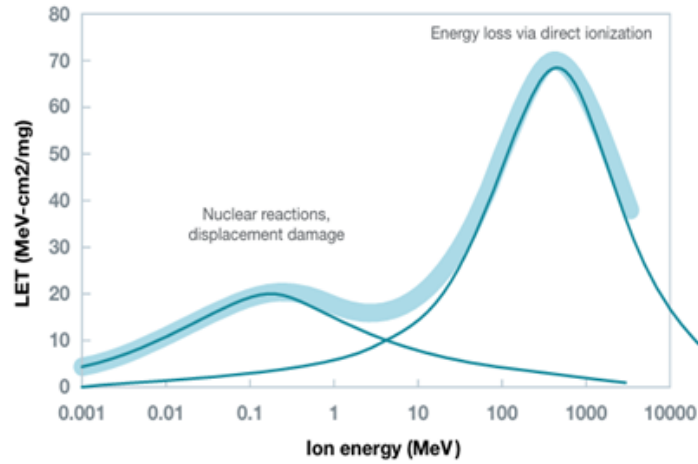


**Figure 2.8:** Linear energy transfer (LET) of a Xenon ion in silicon as a function of ion energy, illustrating the two distinct energy-loss mechanisms: electronic stopping (at higher energies) and nuclear stopping (at lower energies) [6].

As the energetic ion, approaching closer to the nucleus, experiences the full Coulomb repulsive force, this repulsive force, which is inversely proportional to the distance between the two charged bodies, causes the ion to be scattered or deflected onto a new trajectory. During this scattering event, the ion also loses kinetic energy. Through a multitude of successive collisions and interactions with the target material, the ion continues to gradually lose energy until it ultimately comes to rest within the material.

Compared to photons, electrons and nucleons, energetic ions deposit much higher densities of energy along their paths. They leave behind localized, filament-like cylindrical tracks of highly ionized charge in the material. A comparison of different types of radiation and the amount of charge they deposit along their trajectories is illustrated in Figure 2.9.

Because lighter ions and electrons cause much less disturbance than heavy ions,

it is heavy ion strikes that dominate the occurrence of single-event effects (SEEs) in microelectronics, rather than other types of radiation.

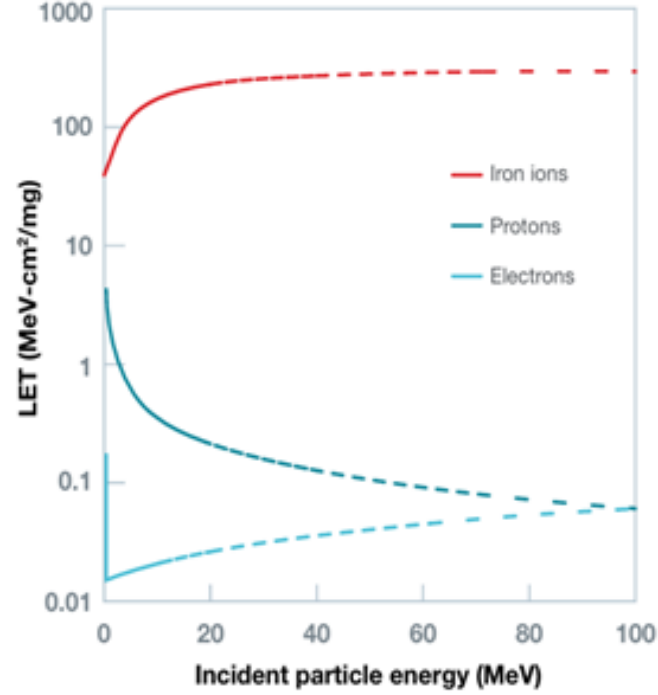


**Figure 2.9:** Comparison of the linear charge generated per distance traveled ( $dQ/dx$ ) by various radiation types in silicon as a function of the incident particle energy. Note that heavier ions are orders of magnitude more disruptive than other particles [6].

When a heavy ion strikes a microelectronic device, it deposits a large amount of excess charge into a very small volume of silicon over an extremely short timescale, typically on the order of femtoseconds to picoseconds. From the perspective of the device, the impact appears as an almost instantaneous injection of ambipolar charge (a combination of electrons and holes) along the ion's path, occurring before any significant charge separation or recombination can take place. Initially, the electron-hole (e-h) pairs remain in close proximity, meaning the overall disturbance appears quasi-neutral until the charges begin to separate.

These events create narrow cylindrical tracks of excess charge, often micrometers in length but only nanometers in radius. If the ion passes through non-sensitive areas of the device, it typically has no noticeable effect. However, when it intersects active regions, such as sensitive device layers, the sudden, localized injection of charge can trigger serious malfunctions, affecting device behavior and reliability.

In addition to the abundant fluxes of protons (hydrogen ions) and alpha particles, heavier ions are primarily encountered in space originating mostly from galactic cosmic rays. These high-energy ions can easily penetrate shielding and packaging materials, depositing more energy and generating more charge than any other type of particle.

In the space environment, heavy ions are a major cause of single-event effects (SEEs) due to their very high linear energy transfer (LET). Their energy deposition can induce a wide range of both nondestructive and destructive SEEs in microelectronics. However, even in space, heavy ions are relatively rare and their fluences are generally too low to cause significant total ionizing dose (TID) or displacement damage dose (DDD) effects.

On Earth, heavy ions pose virtually no threat to microelectronics because they are quickly absorbed by the atmosphere and do not reach ground level.

## **2.5 Summary of Radiation Effects**

Radiation effects on spacecraft systems can be broadly categorized into long-term and short-term impacts. Long-term effects result from the cumulative exposure to radiation, including both ionizing and non-ionizing interactions. In contrast, short-term effects are typically the result of single-particle events, which may still lead to permanent damage depending on their severity.

From a radiation effects perspective, three main mechanisms are considered in space electronics: Total Ionizing Dose (TID), Displacement Damage Dose (DDD) and Single Event Effects (SEE). Each of these mechanisms arises from distinct physical interactions and requires different mitigation strategies.

TID reflects the gradual accumulation of energy deposited in insulating layers or substrates due to prolonged exposure to ionizing radiation. This process can alter key electrical parameters, such as threshold voltage, leakage current and timing characteristics, ultimately degrading circuit performance or causing outright failure. TID is primarily caused by electrons and protons trapped in the Van Allen belts, as well as protons from solar particle events.

DDD arises from the displacement of atoms within a crystal lattice due to collisions with energetic particles like protons and neutrons. This structural disruption leads to material defects that degrade electrical or optical performance over time. Importantly, devices that are tolerant to TID are not necessarily immune to DDD, as the two mechanisms operate independently.

SEE refers to the interaction of a single high-energy particle with a sensitive volume of a device, potentially triggering a transient or permanent malfunction. SEEs are further classified into soft errors, like bit flips in memory and hard errors, which may result in latch-up, burnout or irreversible damage. These effects can

be induced by heavy ions, solar protons or secondary particles generated from interactions with high-energy neutrons or protons.

## Chapter 3

# Synthetic Worst-Case Orbit Definition for Radiation Environment Analysis

The main objective of this section is to identify the worst-case radiation environment by constructing a synthetic orbit. In the absence of a specific mission profile, various orbital conditions were analyzed with the aim of creating an artificial worst-case orbit that combines the most severe environmental factors. This synthetic orbit is designed to represent the most extreme radiation conditions, merging contributions from multiple particle populations and geophysical models. This approach ensures that the analysis encompasses the full range of potential hazards, thereby supporting the development of robust satellite systems capable of operating across any terrestrial orbit, from Low Earth Orbit (LEO) to Geostationary Orbit (GEO). The methodology adopted in constructing this worst-case scenario is grounded in established best practices and internationally recognized standards, which define the appropriate procedures for assessing the diverse radiation effects encountered in space environments, as outlined in ECSS and industry references such as [1], [3] and [5].

As highlighted in [5], the goal of an environment specification is to comprehensively define the severity of the space environment in which the mission must operate, incorporating an appropriate level of conservatism consistent with the mission's risk tolerance. The reference used also provides a description of current-generation tools and methodologies, along with worked examples, aimed at supporting the development of preliminary space environment specifications for satellite system acquisitions. This material serves both as an introductory guide for survivability engineers new to space vehicle design and as a practical reference for experienced professionals seeking to familiarize themselves with updated tools and best practices.

The synthetic orbit was defined through a detailed study of different orbital regimes, namely LEO, Medium Earth Orbit (MEO), Highly Elliptical Orbit (HEO) and GEO, selecting the specific conditions that lead to the maximum radiation exposure. The primary objective is to provide support for the design of a sensor module capable of ensuring reliable operation throughout the mission duration, without failures or malfunctions induced by radiation effects. In this framework, the analysis considers the key radiation contributors: trapped particles, solar energetic particles and galactic cosmic rays (GCRs), evaluating their impact on the Total Ionizing Dose (TID), the Total Non-Ionizing Dose (TNID) and Single-Event Effects (SEE). The results derived from this study will serve as a reference for defining the necessary Radiation Hardness Assurance (RHA) strategies and the required Radiation Design Margin (RDM) for onboard electronics and materials.

The mission analysis focuses on evaluating both the long-term and short-term environmental effects that spacecraft experience during their operational lifetime. The main environmental factors considered include:

- Trapped particle fluences, comprising both electrons and protons in the Earth's magnetosphere;
- Solar particle fluences, namely protons accelerated during Solar Energetic Particle (SEP) events;
- Galactic Cosmic Rays (GCRs), constituting a continuous and pervasive background radiation originating from outside the Solar System.

In order to mitigate the impacts of these environmental factors on satellite systems, the analysis computes several worst-case quantities:

- **Worst-case solar particle flux:** this is particularly important for addressing Single-Event Effects (SEE). If the spacecraft is designed to operate beyond the peak flux, operational continuity is ensured. A worst-case five-minute proton flux was selected, corresponding to the shortest practical timescale within the SEP environment, where elevated fluxes are observed. This selection is justified because spacecraft in most Earth orbits, such as GEO, HEO and polar LEO, are periodically or continuously exposed to interplanetary proton fluxes for durations of at least five minutes. In particular, GEO orbits are permanently exposed, HEO orbits spend considerable time beyond the geomagnetic cutoffs and even polar LEO orbits encounter direct flux exposure when transiting the polar regions.
- **Stormy conditions of the magnetosphere:** severe geomagnetic storms can cause a displacement of the geomagnetic cutoffs equatorward, exposing regions of the orbit that would otherwise be shielded.

- **Confidence-level approach for SEP flux modeling:** a 95% confidence-level flux was adopted to conservatively account for the inherent uncertainties related to solar dynamics and SEP modeling.

The radiation hazards posed by the space environment are intrinsically linked to distinct particle populations, characterized by specific energy ranges, temporal behaviors and spatial distributions. These populations are modeled using geophysical tools, forming the basis for accurate environment specification necessary for satellite system design.

It is important to emphasize that spacecraft frequently sample multiple particle populations during each orbit or episodically over the mission duration. Furthermore, the relationship between environmental sources and resulting satellite hazards is not uniquely defined. For instance, both trapped protons and solar proton events contribute to the total ionizing dose accumulation, while single-event effects can originate from various environmental sources such as GCRs, trapped particles and SEPs.

Table 3.1 summarizes the contributions of each particle environment to the radiation effects considered in this analysis.

**Table 3.1:** Contribution of each environment to different radiation effects

Environment	TID	TNID	SEEs
Trapped protons	X	X	X
Solar protons	X	X	X
Solar heavy ions			X
Galactic cosmic rays			X
Trapped electrons	X	X	

### 3.1 Methodology and Considerations

This section describes the methodology adopted for the analysis and definition of the synthetic worst-case orbit. Different orbital regimes were examined to identify and capture the most severe radiation conditions. For each orbit type, a systematic approach was applied: the relevant radiation environments were characterized, representative altitudes and inclinations were selected and specific modeling assumptions were introduced to ensure conservative and realistic worst-case estimates. The assessment was conducted using two different software tools, SPENVIS (developed by ESA) and OMERE (developed by FASTRAD). This choice was made to gather a broader set of information from independent sources, thereby improving the understanding of the worst-case scenario. It is important to



note that, in the context of modeling and simulation, the definition of a worst case inherently depends on the underlying physics models and mathematical approaches adopted. The following subsections provide a detailed discussion for each orbital regime considered.

### 3.1.1 Low Earth Orbit (LEO)

LEO presents a highly variable radiation environment due to its position relative to the Earth’s radiation belts. The following key features were considered:

#### 1. Environment Characterization:

- *Inner Belt*: high-energy proton environment, with localized intensifications such as the South Atlantic Anomaly (SAA).
- *Outer Belt*: dominated by high-energy electrons, where the geomagnetic field lines bring to low altitudes at “auroral” latitudes above about 50°.
- *Cosmic Rays and Solar Particles*: almost unattenuated fluxes of cosmic rays and solar energetic particles contribute to the overall radiation environment on the high-latitude parts of the orbit.

#### 2. Orbit Selection:

- *Altitude*. Two representative altitudes were analyzed:
  - 400 km: close to the edge of the inner belt and more influenced by the SAA.
  - 800 km: higher exposure to outer belt electrons.
- *Inclination*: Four inclinations were examined:
  - 20° and 40°: representative of regions with significant SAA contribution.
  - 60° and 80°: capturing auroral and polar radiation environments.
- *Exclusion of Equatorial Orbits*: Equatorial inclinations were excluded because the primary radiation contribution at low inclinations comes from the SAA. Higher inclinations were selected to account for auroral-polar environments, which present more challenging radiation conditions.
- *Sun-Synchronous Orbit (SSO)*: an SSO at 894 km altitude and 99° inclination was included due to its high commercial relevance and its representation of a polar orbit.

#### 3. Output:

- The output of the LEO environment analysis is represented by the worst-case curve, referred to as the *LEO Maximum Envelope*, encompassing contributions from scenarios at 400 km, 800 km and SSO. This envelope serves as a unified worst-case baseline and critical input for the definition of the synthetic orbit.

### 3.1.2 Medium Earth Orbit (MEO)

MEO encompasses regions within or across the radiation belts, where the environment is dominated by trapped protons and electrons.

#### 1. Environment Characterization:

- Orbits near the peaks of the inner and outer belts encounter the most severe trapped particle fluxes.
- The inner belt is primarily composed of high-energy protons, while the outer belt contains energetic electrons.

#### 2. Orbit Selection:

- *Altitude.* Two altitudes were selected:
  - 3000 km: near the peak of the inner belt proton flux.
  - 17000 km: near the peak of the outer belt electron flux.
- *Inclination:*
  - Equatorial orbits were selected to maximize exposure to trapped particles, as the geomagnetic field is strongest near the equator.
- *Exclusion of Higher Inclinations:* Higher inclinations were excluded because trapped particle fluxes decrease with increasing inclination.

#### 3. Exclusion of Solar and Cosmic Ray Analysis:

- Solar and cosmic ray analysis was deemed unnecessary for MEO because geomagnetic shielding significantly reduces their contributions; the worst-case scenarios for these components are better represented by GEO analysis.

### 3.1.3 Highly Elliptical Orbit (HEO)

HEO traverses the full range of radiation environments, making it critical for worst-case analysis. A major limitation of Molniya-type orbits is the hazardous radiation environment, with high concentrations of energetic trapped protons and electrons encountered during each perigee pass. HEO satellites generally require more shielding compared to LEO and GEO satellites.

## **1. Orbit Selection:**

- A Molniya orbit was selected with the following parameters:
  - Perigee altitude: 538 km.
  - Apogee altitude: 39906 km.
  - Inclination: 63.4°.
  - Argument of perigee: 270°.

## **2. Assumptions:**

- For conservative analysis and comparison with GEO, geomagnetic shielding was disregarded.

### **3.1.4 Geostationary Orbit (GEO)**

GEO is characterized by a radiation environment dominated by trapped electrons, cosmic rays and solar particles.

#### **1. Environment Characterization:**

- The analysis focused on high-energy electrons in the outer belt.

#### **2. Orbit Selection:**

- Inclination: only 0° was analyzed, as trapped particle flux decreases with increasing inclination.
- Geomagnetic shielding effects were disregarded to ensure conservative results.

#### **3. Models Used:**

- IGE2006-upper case for trapped electron fluxes, as recommended by ECSS-E-ST-10-04C.
- AP8-MIN model for trapped proton fluxes.
- allows the use of IGE2006 only for equatorial inclinations (0°); OMERE, instead, enables inclination variation with IGE2006.

#### **4. Main Assumptions:**

- By removing geomagnetic shielding, solar particle and GCR fluxes become independent of inclination, ensuring a conservative evaluation focused solely on trapped particle variations.

#### **5. Observations with OMERE:**

- Trapped electrons: fluxes remain constant regardless of inclination.
- Trapped protons: fluxes are higher at  $0^\circ$  inclination due to stronger magnetic confinement at the equator.
- TID: remains unchanged across different inclinations.

## 6. Adopted Strategy:

- To ensure direct comparison between SPENVIS and OMERE, the analysis was restricted to  $0^\circ$  inclination (equatorial), representing a worst-case condition and ensuring consistent and comparable results.

tabularx

## 3.1.5 Summary of Selected Orbits

Table 3.2 summarizes the different orbits chosen for the analysis.

**Table 3.2:** Summary of selected orbits

Orbit Type	Altitude (km)	Inclination ( $^\circ$ )	Rationale
LEO	400, 800	20, 40, 60, 80	Capture SAA and auroral-polar environments.
SSO	894	99	Representative of polar orbits; commercially relevant.
MEO	3000, 17000	0	Near inner and outer belt peaks; equatorial worst-case fluxes.
HEO	538 (perigee), 39906 (apogee)	63.4	Covers full radiation environment; conservative assumptions.
GEO	36000	0	Outer belt electrons; conservative analysis.

The selection of synthetic orbits for radiation analysis was guided by the need to capture worst-case scenarios across different orbital environments. Special attention was paid to:

- The variability of LEO, including the influence of the South Atlantic Anomaly (SAA) and polar regions.

- Peak radiation environments in MEO and HEO.
- Unique considerations for GEO, including the application of ECSS-recommended models.
- The simulations were conducted assuming a mission duration of five years, specifically from January 1, 2025 to January 1, 2030. According to data from the NOAA Space Weather Prediction Center<sup>1</sup>, as illustrated in Figure 3.1, this period spans the peak of Solar Cycle 25, expected to occur in 2025 and includes its descending phase toward the next solar minimum, projected to occur around 2030. As such, the radiation environment modeled reflects both the heightened activity typical of solar maximum conditions and the gradual decline toward lower flux levels, ensuring a comprehensive assessment across varying space weather intensities. Solar Cycle 26 is projected to begin sometime between January 2029 and December 2032, although no specific predictions are currently available.

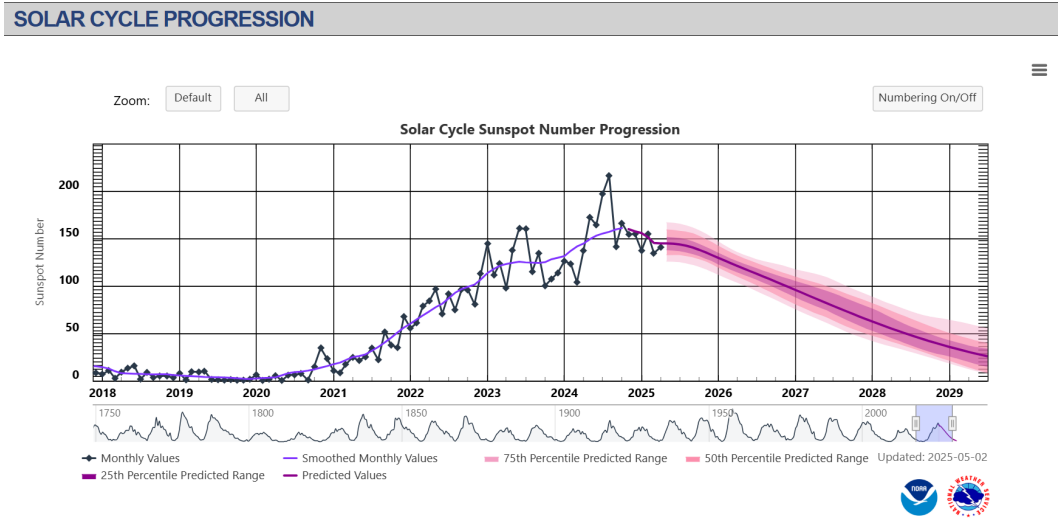


**Figure 3.1:** Solar Cycle 25 progression as reported by NOAA Space Weather Prediction Center. The plot shows the observed and predicted monthly sunspot numbers, highlighting the current solar maximum phase expected to peak in 2025, followed by a gradual decline toward the next solar minimum around 2030, as reported in [24].

<sup>1</sup><https://www.swpc.noaa.gov/products/solar-cycle-progression> [24]

## Chapter 4

# Modeling of the Space Radiation Environment

This chapter describes the models and methods adopted for the radiation analysis. The results presented are the outcome of simulations performed using two different software tools, following a structured approach to ensure reliable comparison across outputs. The selection of environmental models was guided by the recommendations provided in the ECSS standard [1] and [3], ensuring methodological consistency with recognized space engineering practices. In parallel, the worst-case design philosophy was applied to drive the construction of conservative radiation environments, maximizing robustness in the absence of specific mission constraints.

### 4.1 Environment – Trapped Particles

#### 4.1.1 LEO and MEO

Table 4.1 presents the key analytical and numerical models for characterizing trapped particles in Low Earth Orbit (LEO) and Medium Earth Orbit (MEO) regimes.

#### 4.1.2 GEO

As previously stated, for the geostationary orbit there is an exception in the model used. Table 4.2 lists the models used to analyze trapped particle populations in the Geostationary Orbit (GEO) environment.

**Table 4.1:** Models for trapped particles in LEO and MEO environments

	<b>SPENVIS</b>	<b>OMERE</b>
Electrons	AE-8 MAX: - Solar activity: maximum - Magnetic field: Jensen & Cain (standard) - Confidence level: 50%	AE-8 MAX: - Solar activity: maximum - Magnetic field: Jensen & Cain (standard)
Protons	AP-8 MIN: - Solar activity: minimum - Magnetic field: Jensen & Cain (standard)	AP-8 MIN: - Solar activity: minimum - Magnetic field: Jensen & Cain (standard)

**Table 4.2:** Models for trapped particles in GEO environment

	<b>SPENVIS</b>	<b>OMERE</b>
Electrons	IGE 2006: - Upper case	IGE 2006: - Upper case
Protons	AP-8 MIN: - Solar activity: minimum - Magnetic field: Jensen & Cain (standard)	AP-8 MIN: - Solar activity: minimum - Magnetic field: Jensen & Cain (standard)

## 4.2 Environment – Solar Particles

### 4.2.1 Average Statistical Models

Table 4.3 presents the models used for Solar Energetic Particle (SEP) analysis in space environments.

### 4.2.2 Solar Particle Peak Flux During a Solar Flare

Table 4.4 presents current methodologies for modeling upper-bound SEP conditions, including event selection criteria and spectral extrapolation techniques.

In **SPENVIS**, the interface does not explicitly separate protons from heavier ions when configuring a solar particle event (SPE) analysis. Instead, by selecting ions in the range from hydrogen (H) to uranium (U) using the **CRÈME-96** model, protons are inherently included in the analysis, since hydrogen corresponds to a single proton. As a result, the output includes both proton and ion fluxes across different energy levels, even if the configuration appears to treat them collectively.

On the other hand, **OMERE** provides a clear distinction between protons and heavier ions within its interface. However, to ensure consistency between the tools,

**Table 4.3:** Models for solar energetic particles (average statistical models)

	<b>SPENVIS</b>	<b>OMERE</b>
Protons	<b>ESP:</b> <ul style="list-style-type: none"> <li>- Confidence level: 95%</li> <li>- Geomagnetic shielding: Størmer up-grade theory</li> <li>- Magnetospheric condition: stormy</li> <li>- Arrival direction: all</li> <li>- Applied shielding for LET calculation: 3 mm of Al</li> </ul>	<b>ESP:</b> <ul style="list-style-type: none"> <li>- Confidence level: 95%</li> <li>- Geomagnetic shielding: Størmer theory</li> <li>- Magnetospheric condition: stormy</li> <li>- Magnetospheric cutoff: vertical</li> <li>- Applied shielding for LET calculation: 3 mm of Al</li> </ul>
Ions	<b>PSYCHIC:</b> <ul style="list-style-type: none"> <li>- Elements considered: from He to U</li> <li>- Geomagnetic shielding: Størmer up-grade theory</li> <li>- Magnetospheric condition: stormy</li> <li>- Arrival direction: all</li> <li>- Applied shielding for LET calculation: 3 mm of Al</li> </ul>	<b>PSYCHIC:</b> <ul style="list-style-type: none"> <li>- Elements considered: from He to U</li> <li>- Geomagnetic shielding: Størmer theory</li> <li>- Magnetospheric condition: stormy</li> <li>- Magnetospheric cutoff: vertical</li> <li>- Applied shielding for LET calculation: 3 mm of Al</li> </ul>

**Table 4.4:** Models for solar particle peak flux during a solar flare

	<b>SPENVIS</b>	<b>OMERE</b>
Protons	none	<b>Worst 5 min October 1989:</b> <ul style="list-style-type: none"> <li>- Peak 5-minute-averaged fluxes</li> <li>- Geomagnetic shielding: Størmer theory</li> <li>- Magnetospheric condition: stormy</li> <li>- Magnetospheric cutoff: vertical</li> <li>- Applied shielding for LET calculation: 3 mm of Al</li> </ul>
Ions	<b>CRÈME-96:</b> <ul style="list-style-type: none"> <li>- Peak 5-minute-averaged fluxes</li> <li>- Ion range: from H to U</li> <li>- Geomagnetic shielding: Størmer up-grade theory</li> <li>- Magnetospheric condition: stormy</li> <li>- Arrival direction: all</li> <li>- Applied shielding for LET calculation: 3 mm of Al</li> </ul>	<b>CRÈME-96:</b> <ul style="list-style-type: none"> <li>- Peak 5-minute-averaged fluxes</li> <li>- Ion range: from H to U</li> <li>- Geomagnetic shielding: Størmer theory</li> <li>- Magnetospheric condition: stormy</li> <li>- Magnetospheric cutoff: vertical</li> <li>- Applied shielding for LET calculation: 3 mm of Al</li> </ul>

the same modeling assumptions were selected for both particle types: peak 5-minute-averaged fluxes during the October 1989 event, Størmer theory for geomagnetic shielding, stormy magnetospheric conditions, vertical cutoff geometry and 3 mm of



aluminum shielding for LET calculations.

Despite this difference in how particle types are categorized in the setup, the resulting outputs are effectively equivalent: both tools provide spectral fluxes for protons and for ions (from H to U) as a function of energy. The distinction is mainly in the user interface and input structure, not in the physical content of the results.

### 4.3 Environment – Galactic Cosmic Rays (GCR)

Table 4.5 summarizes current models for galactic cosmic ray (GCR) fluxes and their energy spectra across different space environments.

**Table 4.5:** Models for galactic cosmic rays (GCR)

	<b>SPENVIS</b>	<b>OMERE</b>
GCRs	ISO-15390 standard model: - Solar activity: solar minimum - Ion range: from H to U - Geomagnetic shielding: Størmer upgrade theory - Magnetospheric condition: stormy - Arrival direction: all - Applied shielding for LET calculation: 3 mm of Al	ISO-15390 standard model: - Solar activity: solar minimum - Ion range: from H to U - Geomagnetic shielding: Størmer theory - Magnetospheric condition: stormy - Magnetospheric cutoff: vertical - Applied shielding for LET calculation: 3 mm of Al

### 4.4 Total Ionizing Dose (TID) and Total Non-Ionizing Dose (TNID)

#### 4.4.1 TID Evaluation

Table 4.6 lists the radiation transport codes and environment-to-dose conversion methods for TID assessment in different orbital regimes.

**Table 4.6:** Models for TID evaluation

	<b>SPENVIS</b>	<b>OMERE</b>
Total Ionizing Dose	SHIELDOSE-2: - Target material: Silicon - Geometry: centre of Al sphere - Shielding depths: from 0.05 to 20 mm	SHIELDOSE-2: - Target material: Silicon - Geometry: centre of Al sphere - Shielding depths: from 0.05 to 20 mm

### 4.4.2 Displacement Damage Dose (DDD)

Table 4.7 compares non-ionizing energy deposition models for predicting displacement damage effects in electronic devices.

**Table 4.7:** Models for the Displacement Damage Dose (DDD)

NIEL Damage Curve	SPENVIS	OMERE
Silicon	Akkerman Theory: - Damage factor: $1\text{E-}11 \text{ g(Si)·MeV}^{-1}$ - Proton equivalent energy: 10 MeV - Aluminium shielding depths: from 0.05 to 20 mm	Nemo-Onera Theory: - Proton equivalent energy: 10 MeV - Aluminium shielding depths: from 0.05 to 20 mm - Incidence: omnidirectional
Gallium Arsenide	Summers Theory: - Damage factor: $1\text{E-}11 \text{ g(Si)·MeV}^{-1}$ - Proton equivalent energy: 10 MeV - Aluminium shielding depths: from 0.05 to 20 mm	Nemo-Onera Theory: - Proton equivalent energy: 10 MeV - Aluminium shielding depths: from 0.05 to 20 mm - Incidence: omnidirectional

## 4.5 Shielded Fluxes

Table 4.8 reports the boundary conditions defined for the shielded fluxes analysis.

**Table 4.8:** Models for shielded fluxes calculation

	SPENVIS	OMERE
Shielded Fluxes	MFLUX + MULASSIS look-up tables: - Shielding thickness: 3.705 mm of Aluminium - Contribution: solar protons and trapped protons	CREME86: - Shielding thickness: 3 mm of Aluminium - Contribution: solar protons and trapped protons

It is worth noting the reasoning behind the selection of the 3.0 mm value used for calculating the LET and proton flux behind a given shielding thickness. Based on a preliminary analysis of space debris particle impacts, a minimum shielding thickness of 3.0 mm was determined to be required. This value was chosen to provide adequate protection against the mechanical impacts from small debris particles in orbit, mitigating the risk of penetration from space debris.

## Chapter 5

# Synthetic Orbit and Worst-Case Scenario

Once all boundary conditions that influence the results in terms of radiation effects have been defined and described, this chapter presents the results obtained by following the evaluation logic depicted in Figure 5.1. The selection, organization and presentation of the results are structured according to the guidelines provided in Annex A of the ECSS standard [4], referred to as the Mission Radiation Environment Specification. This ensures consistency with recognized practices for documenting space environment assessments in support of system-level requirements.

The results will be presented from different software applying the same models in terms of:

- a. Radiation sources
- b. Magnetic field
- c. Particles interactions with matter

In our case, since two different software tools were used, the results are presented following a systematic format: for each type of output, the tables containing the numerical results obtained from both tools are shown first, followed by the corresponding plots that graphically represent the tabulated data. This structure is repeated consistently across all result categories.

### 5.1 TID and TNID Environment

In this chapter, the results obtained through the use of OMERE and SPENVIS are presented.

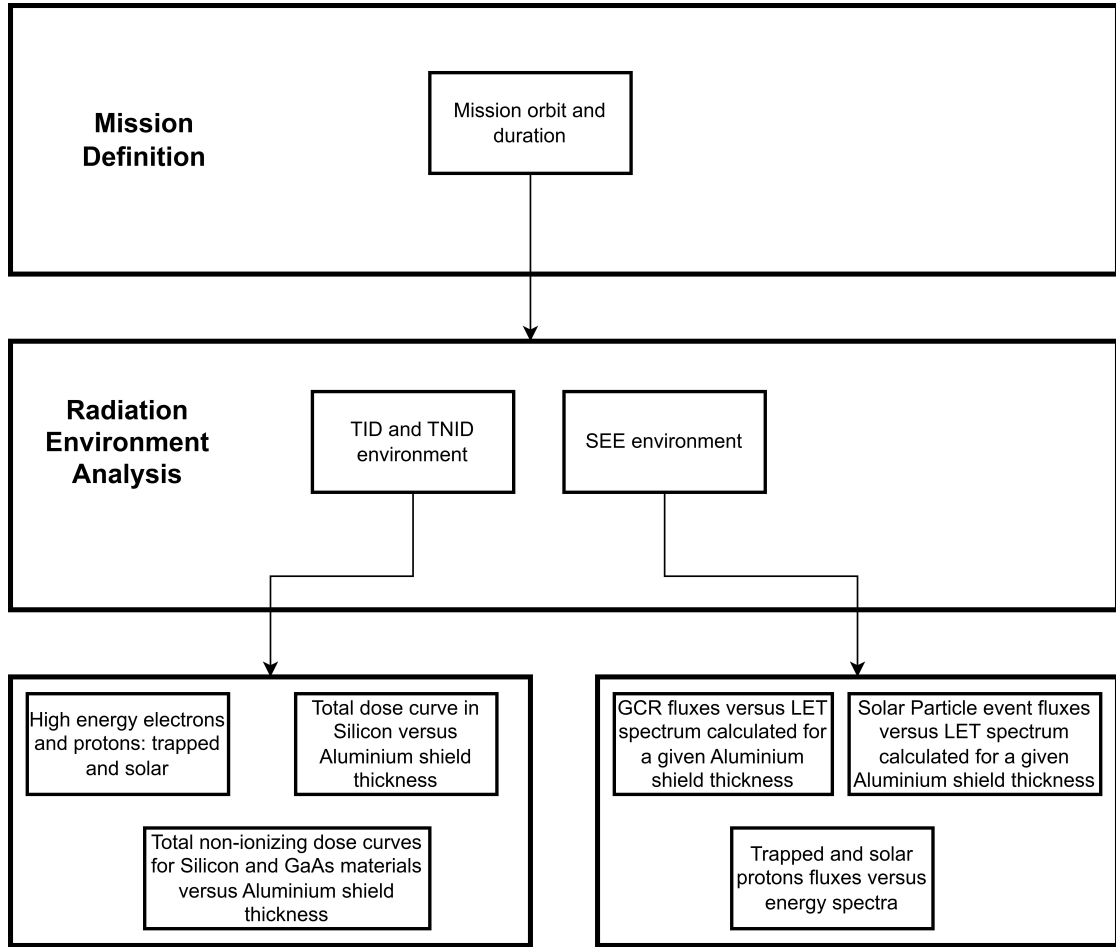


**Figure 5.1:** Schematic representation of the evaluation path for the characterization of the space radiation environment.

### 5.1.1 Protons Incident Fluence versus Energy Spectra

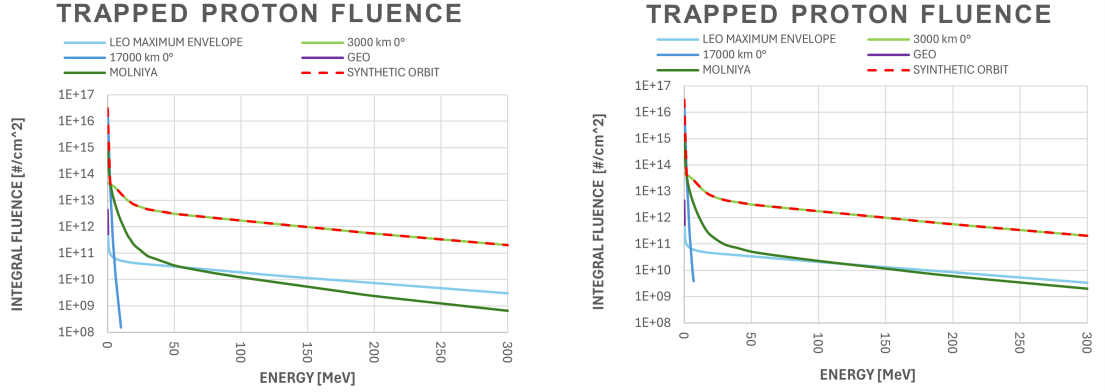
Tables 5.1 and 5.2 show the trapped proton integral fluence over a 5-year mission for different energy bins, as computed using OMERE and SPENVIS respectively.

**Table 5.1:** OMERE – Trapped Proton Integral Fluence for a 5-year mission

ENERGY	LEO MAX ENVELOPE	3000 km 0°	17000 km 0°	GEO	MOLNIYA	SYNTHETIC ORBIT
[MeV]	[#/cm <sup>2</sup> ]	[#/cm <sup>2</sup> ]	[#/cm <sup>2</sup> ]	[#/cm <sup>2</sup> ]	[#/cm <sup>2</sup> ]	[#/cm <sup>2</sup> ]
0.10	2.08E+12	4.65E+13	3.06E+16	4.38E+12	1.37E+15	3.06E+16
0.25	8.82E+11	4.60E+13	1.61E+16	5.37E+11	7.72E+14	1.61E+16
0.50	3.63E+11	4.53E+13	6.38E+15	5.51E+10	3.83E+14	6.38E+15
0.75	2.15E+11	4.46E+13	2.64E+15	0.00E+00	2.27E+14	2.64E+15
1.00	1.54E+11	4.40E+13	1.07E+15	0.00E+00	1.47E+14	1.07E+15
2.00	9.12E+10	4.11E+13	3.36E+13	0.00E+00	4.53E+13	4.53E+13
3.00	7.91E+10	3.86E+13	3.18E+12	0.00E+00	2.44E+13	3.86E+13
4.00	7.08E+10	3.62E+13	3.03E+11	0.00E+00	1.45E+13	3.62E+13
5.00	6.53E+10	3.30E+13	6.50E+10	0.00E+00	9.46E+12	3.30E+13
6.00	6.11E+10	3.01E+13	1.40E+10	0.00E+00	6.32E+12	3.01E+13
8.00	5.54E+10	2.35E+13	1.39E+09	0.00E+00	3.10E+12	2.35E+13
10.00	5.15E+10	1.82E+13	1.50E+08	0.00E+00	1.67E+12	1.82E+13
12.00	4.90E+10	1.44E+13	9.50E+06	0.00E+00	1.00E+12	1.44E+13
15.00	4.58E+10	1.02E+13	0.00E+00	0.00E+00	4.70E+11	1.02E+13
17.00	4.42E+10	8.73E+12	0.00E+00	0.00E+00	3.34E+11	8.73E+12
20.00	4.20E+10	6.92E+12	0.00E+00	0.00E+00	2.02E+11	6.92E+12
25.00	3.97E+10	5.66E+12	0.00E+00	0.00E+00	1.24E+11	5.66E+12
30.00	3.75E+10	4.64E+12	0.00E+00	0.00E+00	7.75E+10	4.64E+12
35.00	3.57E+10	4.20E+12	0.00E+00	0.00E+00	6.26E+10	4.20E+12
40.00	3.40E+10	3.81E+12	0.00E+00	0.00E+00	5.08E+10	3.81E+12
45.00	3.24E+10	3.46E+12	0.00E+00	0.00E+00	4.15E+10	3.46E+12
50.00	3.09E+10	3.14E+12	0.00E+00	0.00E+00	3.40E+10	3.14E+12
60.00	2.81E+10	2.76E+12	0.00E+00	0.00E+00	2.64E+10	2.76E+12
70.00	2.53E+10	2.45E+12	0.00E+00	0.00E+00	2.14E+10	2.45E+12
80.00	2.29E+10	2.18E+12	0.00E+00	0.00E+00	1.74E+10	2.18E+12
90.00	2.06E+10	1.94E+12	0.00E+00	0.00E+00	1.45E+10	1.94E+12
100.00	1.86E+10	1.73E+12	0.00E+00	0.00E+00	1.20E+10	1.73E+12
125.00	1.43E+10	1.30E+12	0.00E+00	0.00E+00	7.99E+09	1.30E+12
150.00	1.14E+10	9.81E+11	0.00E+00	0.00E+00	5.32E+09	9.81E+11
175.00	9.16E+09	7.39E+11	0.00E+00	0.00E+00	3.54E+09	7.39E+11
200.00	7.35E+09	5.56E+11	0.00E+00	0.00E+00	2.36E+09	5.56E+11
300.00	3.00E+09	2.03E+11	0.00E+00	0.00E+00	6.52E+08	2.03E+11

**Table 5.2:** SPENVIS – Trapped Proton Integral Fluence for a 5-year mission

ENERGY	LEO MAX ENVELOPE	3000 km 0°	17000 km 0°	GEO	MOLNIYA	SYNTHETIC ORBIT
[MeV]	[#/cm <sup>2</sup> ]	[#/cm <sup>2</sup> ]	[#/cm <sup>2</sup> ]	[#/cm <sup>2</sup> ]	[#/cm <sup>2</sup> ]	[#/cm <sup>2</sup> ]
1.00E-01	1.81E+12	4.68E+13	2.99E+16	4.38E+12	1.30E+15	2.99E+16
1.50E-01	1.30E+12	4.66E+13	2.38E+16	0.00E+00	1.05E+15	2.38E+16
2.00E-01	9.62E+11	4.65E+13	1.90E+16	0.00E+00	8.56E+14	1.90E+16
3.00E-01	6.15E+11	4.62E+13	1.30E+16	0.00E+00	6.16E+14	1.30E+16
4.00E-01	4.18E+11	4.59E+13	8.92E+15	0.00E+00	4.54E+14	8.92E+15
5.00E-01	3.18E+11	4.56E+13	6.21E+15	0.00E+00	3.50E+14	6.21E+15
6.00E-01	2.51E+11	4.53E+13	4.32E+15	0.00E+00	2.75E+14	4.32E+15
7.00E-01	2.10E+11	4.50E+13	3.05E+15	0.00E+00	2.23E+14	3.05E+15
1.00E+00	1.42E+11	4.42E+13	1.03E+15	0.00E+00	1.28E+14	1.03E+15
1.50E+00	1.03E+11	4.28E+13	1.80E+14	0.00E+00	6.33E+13	1.80E+14
2.00E+00	9.12E+10	4.14E+13	3.16E+13	0.00E+00	3.60E+13	4.14E+13
3.00E+00	7.97E+10	3.88E+13	2.95E+12	0.00E+00	1.87E+13	3.88E+13
4.00E+00	7.19E+10	3.64E+13	2.76E+11	0.00E+00	1.09E+13	3.64E+13
5.00E+00	6.67E+10	3.32E+13	5.85E+10	0.00E+00	7.16E+12	3.32E+13
6.00E+00	6.27E+10	3.03E+13	1.24E+10	0.00E+00	4.86E+12	3.03E+13
7.00E+00	5.99E+10	2.67E+13	3.80E+09	0.00E+00	3.46E+12	2.67E+13
1.00E+01	5.38E+10	1.83E+13	1.10E+08	0.00E+00	1.41E+12	1.83E+13
1.50E+01	4.84E+10	1.02E+13	0.00E+00	0.00E+00	4.39E+11	1.02E+13
2.00E+01	4.48E+10	6.89E+12	0.00E+00	0.00E+00	2.10E+11	6.89E+12
3.00E+01	4.05E+10	4.63E+12	0.00E+00	0.00E+00	9.71E+10	4.63E+12
4.00E+01	3.67E+10	3.81E+12	0.00E+00	0.00E+00	6.96E+10	3.81E+12
5.00E+01	3.34E+10	3.14E+12	0.00E+00	0.00E+00	5.11E+10	3.14E+12
6.00E+01	3.03E+10	2.76E+12	0.00E+00	0.00E+00	4.22E+10	2.76E+12
7.00E+01	2.73E+10	2.46E+12	0.00E+00	0.00E+00	3.58E+10	2.46E+12
1.00E+02	2.04E+10	1.74E+12	0.00E+00	0.00E+00	2.27E+10	1.74E+12
1.50E+02	1.30E+10	9.82E+11	0.00E+00	0.00E+00	1.16E+10	9.82E+11
2.00E+02	8.28E+09	5.56E+11	0.00E+00	0.00E+00	6.01E+09	5.56E+11
3.00E+02	3.32E+09	2.03E+11	0.00E+00	0.00E+00	2.01E+09	2.03E+11
4.00E+02	1.35E+09	7.40E+10	0.00E+00	0.00E+00	6.80E+08	7.40E+10


**Figure 5.2:** Trapped proton environment: results from OMERE are shown on the left, while SPENVIS results are shown on the right

A comparison between the results obtained from **OMERE** and **SPENVIS** shows a generally consistent trend in the identification of worst-case environments:

- Both tools agree that the **outer MEO region (17000 km)** dominates for low-energy protons ( $<1$  MeV), due to the intense population in the outer radiation belt.
- For **medium energies (1–10 MeV)**, both tools confirm that the **inner Van Allen belt** (near 3000 km) represents the primary source of high proton fluence.
- Minor discrepancies arise at select energies (e.g., 1.5–2.0 MeV) where SPENVIS reports slightly higher contributions from Molniya orbit, whereas OMERE favors MEO.
- For high energies ( $>100$  MeV), the differences become less significant due to the low overall trapped population at these energies and both tools converge on similar values and dominant environments.

Despite using the same underlying AP-8 model, minor discrepancies between SPENVIS and OMERE are attributed to different implementation details, spatial resolution, orbit propagation assumptions and averaging methodologies. These differences highlight the importance of cross-validating results with multiple tools when designing radiation-hardened systems for space missions.

### 5.1.2 Electrons Incident Fluence versus Energy Spectra

Since different models were used to characterize the electron environment across the orbits under analysis, each model produced flux values at different energy levels, which are not directly comparable. For example, certain energy bins considered in the GEO model may not be available for LEO. In the case of OMERE, the electron environment has been reported using three distinct tables. Table 5.3 presents the results obtained using the AE8 model, while Table 5.4 shows the fluxes derived from the IGE2006 model, which was applied specifically for the GEO orbit. Table 5.5 summarizes the electron fluxes corresponding to the synthetic orbit across the full energy range of interest.

In contrast, SPENVIS provided a single dataset reported in Table 5.6, where all orbital environments are compiled under a unified energy scale. In this table, the notation *n.a.* (not available) indicates that the electron flux at a given energy could not be provided by the selected model due to a lack of data in the original model formulation for that specific energy bin.

As a consequence of using different models with varying energy resolutions and ranges, the flux values are not always directly comparable across tools and orbits.

**Table 5.3:** OMERE – Trapped Electron Integral Fluence for a 5-year mission in LEO, MEO and Molniya orbits

ENERGY	LEO MAX ENVELOPE	3000 km 0°	17000 km 0°	MOLNIYA
[MeV]	[#/cm <sup>2</sup> ]	[#/cm <sup>2</sup> ]	[#/cm <sup>2</sup> ]	[#/cm <sup>2</sup> ]
4.00E-02	1.34E+14	2.96E+16	9.75E+15	4.36E+15
1.00E-01	8.80E+13	2.16E+16	6.00E+15	2.94E+15
2.50E-01	2.36E+13	7.35E+15	2.49E+15	8.91E+14
5.00E-01	4.23E+12	6.85E+14	1.12E+15	1.59E+14
7.50E-01	1.86E+12	2.30E+14	6.30E+14	5.32E+13
1.00E+00	1.09E+12	1.09E+14	4.13E+14	2.96E+13
1.50E+00	4.59E+11	4.40E+13	2.07E+14	1.19E+13
2.00E+00	1.97E+11	2.00E+13	9.68E+13	4.92E+12
2.50E+00	8.80E+10	9.36E+12	4.86E+13	2.10E+12
3.00E+00	3.26E+10	1.35E+12	1.91E+13	8.19E+11
3.50E+00	1.23E+10	1.13E+11	7.28E+12	3.12E+11
4.00E+00	4.21E+09	9.55E+09	2.31E+12	1.04E+11
4.50E+00	1.27E+09	7.96E+08	6.41E+11	3.10E+10
5.00E+00	3.62E+08	0.00E+00	1.48E+11	8.61E+09
5.50E+00	8.15E+07	0.00E+00	2.85E+10	2.07E+09
6.00E+00	1.20E+07	0.00E+00	4.43E+09	4.56E+08
6.50E+00	2.50E+05	0.00E+00	6.52E+08	8.46E+07
7.00E+00	0.00E+00	0.00E+00	0.00E+00	1.00E+07

**Table 5.4:** OMERE – Trapped Electron Integral Fluence for a 5-year mission in GEO orbit

ENERGY	GEO
[MeV]	[#/cm <sup>2</sup> ]
9.17E-04	1.59E+17
2.01E-03	1.32E+17
1.06E-02	5.03E+16
2.76E-02	2.04E+16
3.91E-02	1.44E+16
2.06E-01	9.90E+14
5.86E-01	1.09E+14
1.29E+00	1.61E+13
1.99E+00	3.95E+12
2.17E+00	2.85E+12
2.37E+00	2.04E+12
2.58E+00	1.42E+12
2.82E+00	9.77E+11
3.08E+00	6.38E+11
3.36E+00	4.05E+11
4.00E+00	1.47E+11
4.76E+00	3.16E+10
5.20E+00	0.00E+00



**Table 5.5:** OMERE – Trapped Electron Integral Fluence for a 5-year mission in the Synthetic orbit

ENERGY	SYNTHETIC ORBIT
[MeV]	[#/cm <sup>2</sup> ]
9.17000e-04	1.59000e+17
1.00000e-03	1.57000e+17
1.19000e-03	1.51093e+17
1.30000e-03	1.48162e+17
1.55000e-03	1.41953e+17
1.69000e-03	1.38667e+17
2.01000e-03	1.31719e+17
2.40000e-03	1.24266e+17
2.61000e-03	1.20347e+17
3.11000e-03	1.12156e+17
3.71000e-03	1.03524e+17
4.04000e-03	9.90857e+16
4.82000e-03	8.99879e+16
5.26000e-03	8.53906e+16
6.26000e-03	7.61652e+16
7.45000e-03	6.71108e+16
8.13000e-03	6.26921e+16
9.68000e-03	5.42554e+16
1.06000e-02	5.02549e+16
1.26000e-02	4.28811e+16
1.50000e-02	3.63798e+16
1.63000e-02	3.35003e+16
1.95000e-02	2.83942e+16
2.32000e-02	2.40673e+16
2.53000e-02	2.21536e+16
2.76000e-02	2.03968e+16
3.29000e-02	1.72535e+16
3.59000e-02	1.57704e+16
3.91000e-02	1.43711e+16
4.66000e-02	1.17082e+16
5.09000e-02	1.04403e+16
6.06000e-02	8.07381e+15
6.61000e-02	6.99841e+15
7.21000e-02	6.04769e+15
8.59000e-02	4.47474e+15
9.37000e-02	3.83215e+15
1.02000e-01	3.29000e+15
1.22000e-01	2.44658e+15
1.45000e-01	1.83052e+15
1.58000e-01	1.57746e+15
1.88000e-01	1.15995e+15
2.06000e-01	9.90125e+14
2.24000e-01	8.42542e+14
2.67000e-01	6.03808e+14
2.91000e-01	5.07960e+14
3.18000e-01	4.25166e+14
3.47000e-01	3.53862e+14
4.13000e-01	2.39393e+14
4.92000e-01	1.60912e+14
5.37000e-01	1.32307e+14
6.39000e-01	9.01502e+13
6.98000e-01	7.44028e+13
8.31000e-01	4.99899e+13
9.07000e-01	4.05423e+13
9.89000e-01	3.27187e+13
1.08000e+00	2.61201e+13
1.29000e+00	1.60624e+13
1.53000e+00	9.44385e+12
1.67000e+00	7.15625e+12
1.99000e+00	3.94774e+12
2.17000e+00	2.85376e+12
2.58000e+00	1.42314e+12
2.82000e+00	9.77243e+11
3.36000e+00	4.05311e+11
4.00000e+00	1.46686e+11
4.36000e+00	7.70025e+10
4.76000e+00	3.16238e+10
5.20000e+00	0.00000e+00

**Table 5.6:** SPENVIS – Trapped Proton Integral Fluence for a 5-year mission

ENERGY	LEO MAX ENVELOPE	3000 km 0°	17000 km 0°	GEO	MOLNIYA	SYNTHETIC ORBIT
[MeV]	[#/cm <sup>2</sup> ]	[#/cm <sup>2</sup> ]	[#/cm <sup>2</sup> ]	[#/cm <sup>2</sup> ]	[#/cm <sup>2</sup> ]	[#/cm <sup>2</sup> ]
9.20E-04	<i>n.a.</i>	<i>n.a.</i>	<i>n.a.</i>	1.38E+17	<i>n.a.</i>	1.38E+17
1.20E-03	<i>n.a.</i>	<i>n.a.</i>	<i>n.a.</i>	1.31E+17	<i>n.a.</i>	1.31E+17
1.60E-03	<i>n.a.</i>	<i>n.a.</i>	<i>n.a.</i>	1.23E+17	<i>n.a.</i>	1.23E+17
2.10E-03	<i>n.a.</i>	<i>n.a.</i>	<i>n.a.</i>	1.15E+17	<i>n.a.</i>	1.15E+17
2.70E-03	<i>n.a.</i>	<i>n.a.</i>	<i>n.a.</i>	1.06E+17	<i>n.a.</i>	1.06E+17
3.50E-03	<i>n.a.</i>	<i>n.a.</i>	<i>n.a.</i>	9.60E+16	<i>n.a.</i>	9.60E+16
4.50E-03	<i>n.a.</i>	<i>n.a.</i>	<i>n.a.</i>	8.54E+16	<i>n.a.</i>	8.54E+16
5.90E-03	<i>n.a.</i>	<i>n.a.</i>	<i>n.a.</i>	7.34E+16	<i>n.a.</i>	7.34E+16
7.70E-03	<i>n.a.</i>	<i>n.a.</i>	<i>n.a.</i>	6.15E+16	<i>n.a.</i>	6.15E+16
1.00E-02	<i>n.a.</i>	<i>n.a.</i>	<i>n.a.</i>	5.05E+16	<i>n.a.</i>	5.05E+16
1.30E-02	<i>n.a.</i>	<i>n.a.</i>	<i>n.a.</i>	4.07E+16	<i>n.a.</i>	4.07E+16
1.70E-02	<i>n.a.</i>	<i>n.a.</i>	<i>n.a.</i>	3.25E+16	<i>n.a.</i>	3.25E+16
3.00E-02	<i>n.a.</i>	<i>n.a.</i>	<i>n.a.</i>	1.98E+16	<i>n.a.</i>	1.98E+16
4.00E-02	1.37E+14	2.95E+16	9.79E+15	<i>n.a.</i>	3.74E+15	2.95E+16
6.10E-02	<i>n.a.</i>	<i>n.a.</i>	<i>n.a.</i>	8.61E+15	<i>n.a.</i>	8.61E+15
8.90E-02	<i>n.a.</i>	<i>n.a.</i>	<i>n.a.</i>	4.65E+15	<i>n.a.</i>	4.65E+15
1.00E-01	8.93E+13	2.15E+16	6.03E+15	<i>n.a.</i>	2.50E+15	2.15E+16
1.30E-01	<i>n.a.</i>	<i>n.a.</i>	<i>n.a.</i>	2.50E+15	<i>n.a.</i>	2.50E+15
1.80E-01	<i>n.a.</i>	<i>n.a.</i>	<i>n.a.</i>	1.47E+15	<i>n.a.</i>	1.47E+15
2.00E-01	3.57E+13	1.05E+16	3.36E+15	<i>n.a.</i>	1.13E+15	1.05E+16
2.70E-01	<i>n.a.</i>	<i>n.a.</i>	<i>n.a.</i>	7.12E+14	<i>n.a.</i>	7.12E+14
3.00E-01	1.62E+13	4.55E+15	2.14E+15	<i>n.a.</i>	5.29E+14	4.55E+15
4.00E-01	7.95E+12	1.76E+15	1.55E+15	3.22E+14	2.66E+14	1.76E+15
5.00E-01	4.33E+12	6.82E+14	1.13E+15	<i>n.a.</i>	1.45E+14	1.13E+15
6.00E-01	3.07E+12	4.40E+14	8.97E+14	<i>n.a.</i>	9.14E+13	8.97E+14
6.10E-01	<i>n.a.</i>	<i>n.a.</i>	<i>n.a.</i>	1.30E+14	<i>n.a.</i>	1.30E+14
7.00E-01	2.23E+12	2.84E+14	7.12E+14	<i>n.a.</i>	6.21E+13	7.12E+14
8.00E-01	1.71E+12	1.97E+14	5.83E+14	<i>n.a.</i>	4.63E+13	5.83E+14
9.10E-01	<i>n.a.</i>	<i>n.a.</i>	<i>n.a.</i>	5.49E+13	<i>n.a.</i>	5.49E+13
1.00E+00	1.12E+12	1.09E+14	4.17E+14	<i>n.a.</i>	2.94E+13	4.17E+14
1.25E+00	7.22E+11	6.89E+13	2.94E+14	2.38E+13	1.85E+13	2.94E+14
1.28E+00	<i>n.a.</i>	<i>n.a.</i>	<i>n.a.</i>	<i>n.a.</i>	<i>n.a.</i>	2.38E+13
1.50E+00	4.69E+11	4.37E+13	2.07E+14	<i>n.a.</i>	1.18E+13	2.07E+14
1.75E+00	3.07E+11	2.95E+13	1.42E+14	5.95E+12	7.58E+12	1.42E+14
1.99E+00	<i>n.a.</i>	<i>n.a.</i>	<i>n.a.</i>	<i>n.a.</i>	<i>n.a.</i>	5.95E+12
2.00E+00	2.01E+11	1.99E+13	9.71E+13	<i>n.a.</i>	4.88E+12	9.71E+13
2.25E+00	1.34E+11	1.36E+13	6.88E+13	2.76E+12	3.18E+12	6.88E+13
2.44E+00	<i>n.a.</i>	<i>n.a.</i>	<i>n.a.</i>	<i>n.a.</i>	<i>n.a.</i>	2.76E+12
2.50E+00	9.08E+10	9.31E+12	4.87E+13	<i>n.a.</i>	<i>n.a.</i>	4.87E+13
2.75E+00	5.57E+10	3.53E+12	3.05E+13	<i>n.a.</i>	1.28E+12	3.05E+13
3.00E+00	3.47E+10	1.34E+12	1.91E+13	9.96E+11	7.92E+11	1.91E+13
3.07E+00	<i>n.a.</i>	<i>n.a.</i>	<i>n.a.</i>	<i>n.a.</i>	<i>n.a.</i>	9.96E+11
3.25E+00	2.13E+10	3.88E+11	1.17E+13	<i>n.a.</i>	4.84E+11	1.17E+13
3.50E+00	1.32E+10	1.13E+11	7.23E+12	<i>n.a.</i>	2.98E+11	7.23E+12
3.75E+00	7.71E+09	3.27E+10	4.06E+12	<i>n.a.</i>	1.71E+11	4.06E+12
3.97E+00	<i>n.a.</i>	<i>n.a.</i>	<i>n.a.</i>	2.31E+11	<i>n.a.</i>	2.31E+11
4.00E+00	4.53E+09	9.49E+09	2.28E+12	<i>n.a.</i>	9.89E+10	2.28E+12
4.25E+00	2.48E+09	2.74E+09	1.20E+12	<i>n.a.</i>	5.35E+10	1.20E+12
4.50E+00	1.37E+09	7.91E+08	6.33E+11	<i>n.a.</i>	2.92E+10	6.33E+11
4.75E+00	7.27E+08	2.17E+08	3.03E+11	<i>n.a.</i>	1.49E+10	3.03E+11
5.00E+00	3.90E+08	0.00E+00	1.45E+11	0.00E+00	7.96E+09	1.45E+11
5.20E+00	<i>n.a.</i>	<i>n.a.</i>	<i>n.a.</i>	<i>n.a.</i>	<i>n.a.</i>	0.00E+00
5.50E+00	8.64E+07	0.00E+00	2.78E+10	<i>n.a.</i>	1.88E+09	2.78E+10
6.00E+00	1.03E+07	0.00E+00	4.29E+09	<i>n.a.</i>	4.06E+08	4.29E+09
6.50E+00	0.00E+00	0.00E+00	6.15E+08	<i>n.a.</i>	7.38E+07	6.15E+08
7.00E+00	0.00E+00	0.00E+00	0.00E+00	<i>n.a.</i>	8.15E+06	8.15E+06

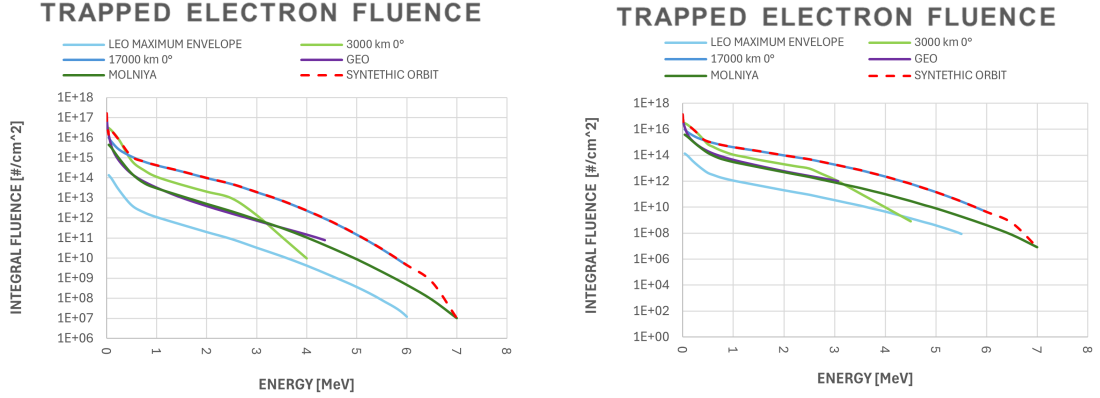


**Figure 5.3:** Trapped electron environment: results from OMERE are shown on the left, while SPENVIS results are shown on the right

A high-resolution comparison of trapped electron integral fluence spectra was carried out between **OMERE** and **SPENVIS** for a 5-year mission duration. The data span energies from  $\sim 1$  keV up to 7 MeV, with fine binning to capture spectral trends.

- Both tools show excellent agreement in identifying the **GEO orbit** as the dominant contributor to trapped electron fluence in the lower energy range (from  $\sim 1$  keV to  $\sim 0.1$  MeV), with peak fluence levels exceeding  $10^{17}$  electrons/cm<sup>2</sup> at  $\sim 1$  MeV.
- In the mid-energy range (0.1–1 MeV), OMERE and SPENVIS show **consistent spectral shapes**, but OMERE reports slightly higher fluences in the MEO region, possibly due to differences in spatial averaging or drift-shell interpolation.
- At higher energies ( $>1$  MeV), the total fluence drops off by several orders of magnitude in both tools. However, SPENVIS includes several additional data points above 4 MeV not fully covered in OMERE's table. These points show the presence of residual high-energy electrons in GEO and 17000 km orbits, relevant for **TID and deep penetration** effects in shielding design.
- Across all energies, the worst-case values remain consistent between the two tools in terms of orbital origin: GEO for low energies, 17000 km MEO for moderate energies and negligible flux for LEO across the entire spectrum.

### 5.1.3 Total dose curve

Table 5.7 and Table 5.8 show the accumulated total dose in Silicon versus Aluminium shield thickness for a solid sphere geometry over a 5-year mission.

**Table 5.7:** OMERE – TID results for a 5-year mission

SHIELDING	LEO MAX ENVELOPE	3000 km 0°	17000 km 0°	GEO	MOLNIYA	SYNTHETIC ORBIT
[mm]	[rad]	[rad]	[rad]	[rad]	[rad]	[rad]
0.05	6.22E+06	1.51E+09	4.46E+08	2.49E+08	2.76E+08	1.51E+09
0.1	3.28E+06	9.01E+08	2.16E+08	9.90E+07	1.40E+08	9.01E+08
0.2	1.30E+06	3.87E+08	1.21E+08	3.77E+07	6.22E+07	3.87E+08
0.3	6.68E+05	1.84E+08	8.38E+07	2.03E+07	3.31E+07	1.84E+08
0.4	4.04E+05	1.02E+08	6.33E+07	1.26E+07	1.94E+07	1.02E+08
0.5	2.74E+05	6.37E+07	5.02E+07	8.51E+06	1.22E+07	6.37E+07
0.6	2.01E+05	4.36E+07	4.12E+07	6.13E+06	8.19E+06	4.36E+07
0.8	1.28E+05	2.45E+07	2.97E+07	3.67E+06	4.37E+06	2.97E+07
1	9.21E+04	1.60E+07	2.27E+07	2.46E+06	2.75E+06	2.27E+07
1.5	5.25E+04	7.75E+06	1.38E+07	1.12E+06	1.28E+06	1.38E+07
2	3.47E+04	4.79E+06	9.14E+06	5.87E+05	7.46E+05	9.14E+06
2.5	2.45E+04	3.33E+06	6.19E+06	3.36E+05	4.69E+05	6.19E+06
3	1.82E+04	2.52E+06	4.24E+06	2.06E+05	3.06E+05	4.24E+06
4	1.13E+04	1.53E+06	1.99E+06	8.87E+04	1.40E+05	1.99E+06
5	7.86E+03	9.90E+05	8.69E+05	4.36E+04	7.06E+04	9.90E+05
6	6.20E+03	7.81E+05	3.52E+05	2.42E+04	4.12E+04	7.81E+05
7	5.25E+03	6.89E+05	1.36E+05	1.47E+04	2.75E+04	6.89E+05
8	4.73E+03	6.29E+05	5.23E+04	1.01E+04	2.09E+04	6.29E+05
9	4.32E+03	5.63E+05	2.26E+04	7.43E+03	1.66E+04	5.63E+05
10	4.04E+03	5.04E+05	1.27E+04	6.00E+03	1.38E+04	5.04E+05
12	3.78E+03	4.32E+05	8.29E+03	4.60E+03	1.07E+04	4.32E+05
14	3.53E+03	3.84E+05	7.36E+03	3.78E+03	8.80E+03	3.84E+05
16	3.31E+03	3.52E+05	6.81E+03	3.20E+03	7.53E+03	3.52E+05
18	3.13E+03	3.29E+05	6.37E+03	2.77E+03	6.62E+03	3.29E+05
20	2.95E+03	3.07E+05	5.94E+03	2.42E+03	5.86E+03	3.07E+05

Table 5.8: SPENVIS – TID results for a 5-year mission

ENERGY	LEO MAX ENVELOPE	3000 km 0°	17000 km 0°	GEO	MOLNIYA	SYNTHETIC ORBIT
[mm]	[rad]	[rad]	[rad]	[rad]	[rad]	[rad]
5.00E-02	6.55E+06	1.44E+09	5.84E+08	2.73E+08	2.55E+08	1.44E+09
1.00E-01	3.65E+06	9.09E+08	2.49E+08	1.12E+08	1.30E+08	9.09E+08
2.00E-01	1.55E+06	4.61E+08	1.31E+08	4.45E+07	5.72E+07	4.61E+08
3.00E-01	8.21E+05	2.45E+08	8.82E+07	2.47E+07	3.08E+07	2.45E+08
4.00E-01	4.84E+05	1.35E+08	6.61E+07	1.55E+07	1.86E+07	1.35E+08
5.00E-01	3.11E+05	7.83E+07	5.23E+07	1.06E+07	1.21E+07	7.83E+07
6.00E-01	2.18E+05	4.92E+07	4.27E+07	7.70E+06	8.38E+06	4.92E+07
8.00E-01	1.34E+05	2.66E+07	3.08E+07	4.69E+06	4.65E+06	3.08E+07
1.00E+00	9.56E+04	1.78E+07	2.35E+07	3.20E+06	2.97E+06	2.35E+07
1.50E+00	5.34E+04	8.71E+06	1.40E+07	1.51E+06	1.37E+06	1.40E+07
2.00E+00	3.49E+04	5.26E+06	9.31E+06	8.17E+05	7.90E+05	9.31E+06
2.50E+00	2.45E+04	3.60E+06	6.33E+06	4.76E+05	4.93E+05	6.33E+06
3.00E+00	1.80E+04	2.63E+06	4.29E+06	2.89E+05	3.20E+05	4.29E+06
4.00E+00	1.11E+04	1.59E+06	2.01E+06	1.18E+05	1.48E+05	2.01E+06
5.00E+00	7.79E+03	1.07E+06	8.88E+05	5.19E+04	7.50E+04	1.07E+06
6.00E+00	6.20E+03	8.23E+05	3.59E+05	2.37E+04	4.33E+04	8.23E+05
7.00E+00	5.32E+03	7.05E+05	1.40E+05	1.15E+04	2.90E+04	7.05E+05
8.00E+00	4.94E+03	6.33E+05	5.47E+04	7.29E+03	2.22E+04	6.33E+05
9.00E+00	4.75E+03	5.82E+05	2.41E+04	5.85E+03	1.84E+04	5.82E+05
1.00E+01	4.55E+03	5.32E+05	1.37E+04	5.13E+03	1.58E+04	5.32E+05
1.20E+01	4.25E+03	4.58E+05	8.70E+03	4.16E+03	1.26E+04	4.58E+05
1.40E+01	3.98E+03	4.06E+05	7.65E+03	3.46E+03	1.05E+04	4.06E+05
1.60E+01	3.76E+03	3.73E+05	7.07E+03	2.95E+03	9.19E+03	3.73E+05
1.80E+01	3.57E+03	3.50E+05	6.60E+03	2.57E+03	8.24E+03	3.50E+05
2.00E+01	3.37E+03	3.27E+05	6.20E+03	2.26E+03	7.47E+03	3.27E+05

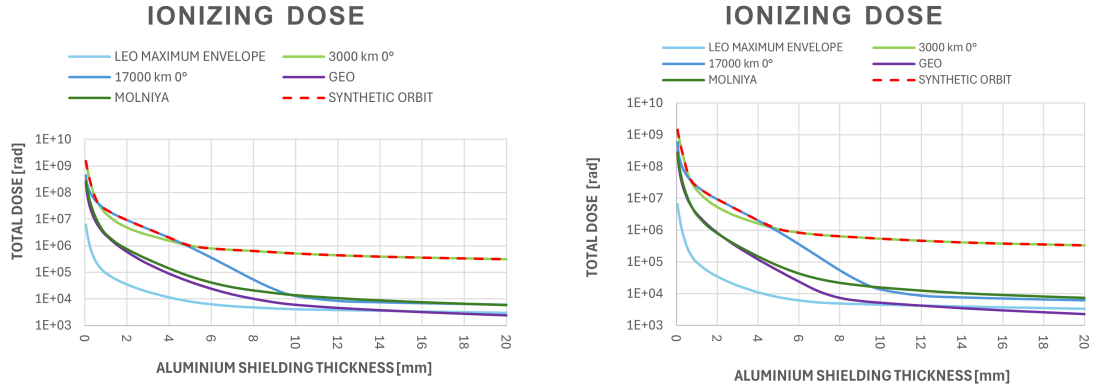


**Figure 5.4:** Dose depth curve: results from OMERE are shown on the left, while SPENVIS results are shown on the right

The TID analysis shows more evident discrepancies between OMERE and SPENVIS, especially at specific shielding levels:

- At **low shielding** (e.g., 0.05 mm Al), both tools predict extreme values above

$10^9$  rad(Si) in MEO (3000 km), but OMERE consistently reports slightly higher values (up to +5% at 1 mm and +10% at 2 mm).

- In the **intermediate shielding range** (4–10 mm), both tools identify the same worst-case orbit (3000 km) and show converging values (e.g., at 10 mm, SPENVIS gives  $5.32 \times 10^5$  rad vs  $5.04 \times 10^5$  rad from OMERE). Discrepancies remain within  $\sim 10\%$  and are acceptable for most shielding assessments.
- At **high shielding levels** ( $>12$  mm), the tools converge more closely, as shielding capability decreases and both tools show this saturation trend.
- For **LEO, GEO and Molniya** environments, both tools agree that these contribute less to TID compared to MEO, especially around 3000 km.

#### 5.1.4 On the "100 krad(Si)" Threshold as a Reference for TID Tolerance

The value of 100 krad(Si) is frequently regarded as a “magic number” [50] in radiation tolerance analysis for a multi-year mission. This threshold is often used as a benchmark for assessing the survivability of electronic components in the presence of cumulative radiation effects. For a first-order analysis, let us consider this 100 krad(Si) tolerance over a mission duration of 60 months (5 years). Dividing the total TID tolerance by the mission duration gives an allowable dose rate of approximately: 1.6 krad/month.

However, when evaluating specific orbital environments, it becomes evident that this threshold can be exceeded. For instance, at an altitude of 3000 km, which is near the peak of the inner radiation belt, the cumulative dose over 5 years behind a shielding of 5 mm aluminium, as obtained with Omere, is approximately 990 krad. Dividing this cumulative dose by the mission duration yields: 16.5 krad/month. This dose rate exceeds the “magic number” by a factor of more than 10. Similarly, the threshold is also exceeded at 17000 km, near the peak of the outer radiation belt. This significant discrepancy highlights the unsuitability of long-duration missions in such an orbit without implementing additional radiation mitigation strategies.

Given the high dose rates encountered in these environments, it is clear that operational constraints must be placed on mission duration for spacecraft operating at these altitudes. For instance:

- **Mission Duration Limitation:** reducing the total time spent in such orbits to ensure that the cumulative TID remains below the acceptable threshold for onboard electronics.

- **Increased Shielding:** employing thicker shielding (e.g., beyond 5 mm of aluminum) to reduce the radiation dose rate. This, however, must be balanced with mass constraints of the satellite. It is true that it is possible to reduce TID with an increased shielding, but as shielding is increased, shielding effectiveness decreases because of the difficulty in slowing down the higher energy protons. A shielding material absorbs most electrons and lower energy protons.
- **Alternative Orbital Strategies:** avoiding prolonged exposure to radiation belt peaks by using transfer orbits or partial mission phases at lower radiation environments.

**Alternative Shielding Materials for Radiation Protection** In space mission design, aluminum (Al) has traditionally been the material of choice for spacecraft shielding due to its availability, well-understood properties and balance between structural and radiation shielding performance. However, emerging studies, as reported in [25], [26] and [27], have explored alternative materials that could achieve equivalent or better shielding performance while offering weight savings and improved adaptability to specific radiation environments.

Potential competitors could be polymeric materials (low atomic number,  $Z$ ) such as polyethylene (PE) and epoxy and metallic materials (high  $Z$ ) such as tantalum (Ta) and tungsten (W). By analyzing shielding efficiency, weight savings and performance trade-offs, it is possible to identify optimal materials for specific orbital environments.

#### **Shielding Performance in Different Environments**

- **High- $Z$  materials:** high- $Z$  materials like tantalum and tungsten are highly effective in electron-dominated radiation environments. Their superior shielding performance makes them the preferred choice for orbits where trapped electrons are the primary radiation source [2]. While these materials offer effective radiation attenuation, their high density ( $16.65 \text{ g/cm}^3$  for Ta and  $19.3 \text{ g/cm}^3$  for W) makes them less advantageous for weight-sensitive missions.
- **Low- $Z$  materials:** in proton-dominated environments, low- $Z$  polymeric materials like polyethylene ( $0.94 \text{ g/cm}^3$ ) and epoxy ( $1.28 \text{ g/cm}^3$ ) demonstrate better shielding efficiency [2] and can provide significant weight savings over traditional aluminum shielding.

#### **Practical Considerations**

1. **Structural Properties:** PE has inherently weaker structural properties compared to aluminum. To address this, the material can be reinforced with fibers to create PE-based composites. Such composites are being actively developed to enhance mechanical strength while retaining the radiation shielding advantages of polyethylene.

2. **Material Compatibility:** any shielding material must satisfy additional requirements for spacecraft applications, including resistance to:

- Outgassing: To prevent contamination of sensitive spacecraft instruments.
- Atomic Oxygen (AO): Particularly in low Earth orbit (LEO), where AO can erode surfaces.
- Thermal Cycling: Ability to withstand extreme temperature variations in space.
- Space Charging: Mitigating the buildup of electrostatic charges that can interfere with spacecraft operations.

### 5.1.5 Total non-ionizing dose

Table 5.9 and Table 5.10 show total non-ionizing dose for Silicon and GaAs materials versus Aluminium shield thickness for a solid sphere geometry

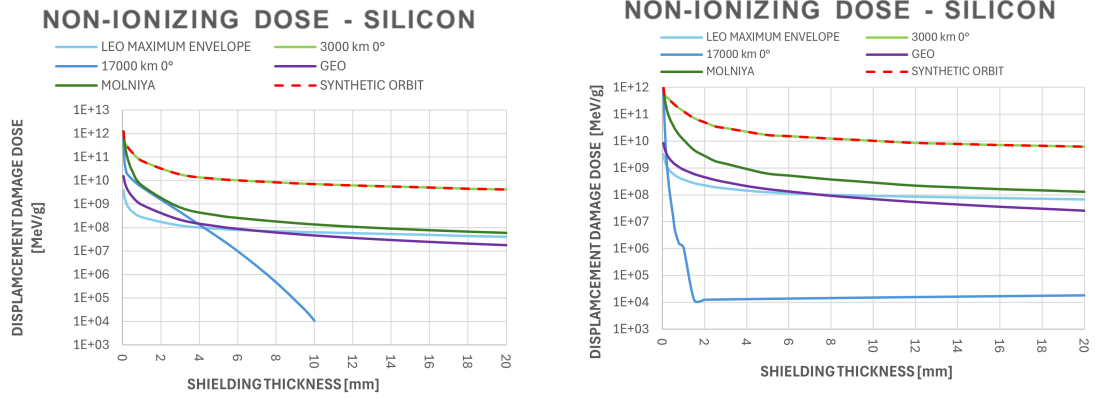
**Table 5.9:** OMERE – displacement damage dose for Silicon for a 5-year mission

SHIELDING	LEO MAX ENVELOPE	3000 km 0°	17000 km 0°	GEO	MOLNIYA	SYNTHETIC ORBIT
[mm]	[MeV/g]	[MeV/g]	[MeV/g]	[MeV/g]	[MeV/g]	[MeV/g]
0.05	3.89E+09	4.99E+11	9.63E+11	1.53E+10	1.24E+12	1.24E+12
0.1	2.01E+09	4.16E+11	6.67E+10	9.18E+09	4.30E+11	4.30E+11
0.2	1.06E+09	3.17E+11	2.21E+10	5.16E+09	1.42E+11	3.17E+11
0.3	7.43E+08	2.46E+11	1.67E+10	3.56E+09	6.93E+10	2.46E+11
0.5	4.84E+08	1.57E+11	1.12E+10	2.12E+09	2.64E+10	1.57E+11
1	2.77E+08	6.89E+10	5.20E+09	9.28E+08	6.31E+09	6.89E+10
3	1.23E+08	1.80E+10	4.55E+08	2.11E+08	7.20E+08	1.80E+10
5	8.91E+07	1.15E+10	3.76E+07	1.10E+08	3.27E+08	1.15E+10
6	7.97E+07	1.01E+10	9.77E+06	8.71E+07	2.60E+08	1.01E+10
7	7.43E+07	9.12E+09	2.26E+06	7.16E+07	2.15E+08	9.12E+09
8	7.03E+07	8.29E+09	4.63E+05	6.06E+07	1.82E+08	8.29E+09
9	6.68E+07	7.59E+09	7.85E+04	5.21E+07	1.57E+08	7.59E+09
10	6.36E+07	7.00E+09	1.07E+04	4.54E+07	1.37E+08	7.00E+09
12	5.81E+07	6.14E+09	6.10E+01	3.57E+07	1.09E+08	6.14E+09
14	5.34E+07	5.51E+09	0.00E+00	2.89E+07	9.08E+07	5.51E+09
16	4.91E+07	5.01E+09	0.00E+00	2.41E+07	7.78E+07	5.01E+09
18	4.39E+07	4.45E+09	0.00E+00	2.04E+07	6.78E+07	4.45E+09
20	4.10E+07	4.12E+09	0.00E+00	1.75E+07	5.97E+07	4.12E+09



**Table 5.10:** SPENVIS – displacement damage dose for Silicon for a 5-year mission

SHIELDING	LEO MAX ENVELOPE	3000 km 0°	17000 km 0°	GEO	MOLNIYA	SYNTHETIC ORBIT
[mm]	[MeV/g]	[MeV/g]	[MeV/g]	[MeV/g]	[MeV/g]	[MeV/g]
0.05	3.24E+09	5.54E+11	8.00E+11	8.45E+09	9.93E+11	9.93E+11
0.1	2.01E+09	5.07E+11	5.07E+10	5.46E+09	4.23E+11	5.07E+11
0.2	1.19E+09	4.34E+11	1.82E+09	3.31E+09	1.59E+11	4.34E+11
0.3	8.74E+08	3.75E+11	2.41E+08	2.41E+09	8.66E+10	3.75E+11
0.4	7.09E+08	3.07E+11	5.85E+07	1.92E+09	5.56E+10	3.07E+11
0.5	6.11E+08	2.60E+11	1.69E+07	1.60E+09	3.94E+10	2.60E+11
0.6	5.30E+08	2.20E+11	4.60E+06	1.38E+09	2.79E+10	2.20E+11
0.8	4.29E+08	1.66E+11	1.51E+06	1.07E+09	1.67E+10	1.66E+11
1	3.69E+08	1.30E+11	1.11E+06	8.71E+08	1.12E+10	1.30E+11
1.50	2.72E+08	7.19E+10	1.25E+04	5.97E+08	4.63E+09	7.19E+10
2.00	2.26E+08	5.05E+10	1.26E+04	4.54E+08	2.83E+09	5.05E+10
2.50	1.91E+08	3.56E+10	1.28E+04	3.57E+08	1.80E+09	3.56E+10
3.00	1.72E+08	3.07E+10	1.30E+04	2.96E+08	1.44E+09	3.07E+10
4.00	1.43E+08	2.26E+10	1.33E+04	2.12E+08	9.12E+08	2.26E+10
5.00	1.24E+08	1.70E+10	1.36E+04	1.63E+08	6.10E+08	1.70E+10
6.00E	1.13E+08	1.54E+10	1.39E+04	1.33E+08	5.20E+08	1.54E+10
7.00E	1.04E+08	1.39E+10	1.42E+04	1.10E+08	4.38E+08	1.39E+10
8.00E	9.84E+07	1.25E+10	1.46E+04	9.16E+07	3.71E+08	1.25E+10
9.00E	9.49E+07	1.15E+10	1.49E+04	7.95E+07	3.26E+08	1.15E+10
10	9.12E+07	1.04E+10	1.52E+04	6.93E+07	2.83E+08	1.04E+10
12	8.46E+07	8.67E+09	1.58E+04	5.36E+07	2.18E+08	8.67E+09
14	7.97E+07	7.93E+09	1.65E+04	4.36E+07	1.88E+08	7.93E+09
16	7.49E+07	7.23E+09	1.71E+04	3.57E+07	1.62E+08	7.23E+09
18	7.08E+07	6.77E+09	1.77E+04	3.03E+07	1.45E+08	6.77E+09
20	6.65E+07	6.28E+09	1.83E+04	2.55E+07	1.29E+08	6.28E+09


**Figure 5.5:** Non-ionizing dose depth curve for Silicon target material: results from OMERE are shown on the left, while SPENVIS results are shown on the right

The Displacement Damage Dose (DDD) in silicon was estimated for a 5-year mission across a wide range of aluminum shielding thicknesses, using both **OMERE** and **SPENVIS**. The comparison reveals a high-level agreement in overall trends and worst-case orbital contributors, with some tool-dependent differences in numerical output:

- For **minimal shielding** ( $\leq 0.1$  mm), both tools predict extremely high DDD values in MEO regions. The discrepancies may be linked to differences in energy bin resolution or NIEL interpolation within the tools.
- In the **intermediate range** (1–10 mm), both tools consistently identify **3000 km** as the dominant environment. OMERE tends to predict higher contributions from **proton-dominated inner belt**, while SPENVIS includes more structured attenuation with increasing shielding.
- For **high shielding** ( $>10$  mm), both tools show strong convergence, with dose values flattening and becoming limited by high-energy proton components.
- Notably, **GEO and Molniya** orbits consistently result in significantly lower DDD compared to MEO, as expected due to geomagnetic shielding and electron-dominated environments.

**Table 5.11:** OMERE – displacement damage dose for Gallium Arsenide (GaAs) for a 5-year mission

SHIELDING	LEO MAX ENVELOPE	3000 km 0°	17000 km 0°	GEO	MOLNIYA	SYNTHETIC ORBIT
[mm]	[MeV/g]	[MeV/g]	[MeV/g]	[MeV/g]	[MeV/g]	[MeV/g]
0.05	3.22E+09	4.40E+11	7.25E+11	1.17E+10	9.83E+11	9.83E+11
0.1	1.74E+09	3.71E+11	5.01E+10	7.07E+09	3.49E+11	3.71E+11
0.2	9.66E+08	2.85E+11	1.65E+10	4.11E+09	1.18E+11	2.85E+11
0.3	7.05E+08	2.24E+11	1.27E+10	2.92E+09	5.85E+10	2.24E+11
0.5	4.84E+08	1.46E+11	8.73E+09	1.81E+09	2.28E+10	1.46E+11
1	2.99E+08	6.82E+10	4.12E+09	8.47E+08	5.71E+09	6.82E+10
3	1.51E+08	2.12E+10	3.60E+08	2.20E+08	7.46E+08	2.12E+10
5	1.16E+08	1.45E+10	2.90E+07	1.21E+08	3.66E+08	1.45E+10
6	1.08E+08	1.30E+10	7.39E+06	9.76E+07	2.97E+08	1.30E+10
7	1.02E+08	1.19E+10	1.67E+06	8.15E+07	2.50E+08	1.19E+10
8	9.73E+07	1.09E+10	3.34E+05	6.98E+07	2.15E+08	1.09E+10
9	9.28E+07	1.01E+10	5.49E+04	6.07E+07	1.88E+08	1.01E+10
10	8.87E+07	9.45E+09	7.16E+03	5.34E+07	1.66E+08	9.45E+09
12	8.14E+07	8.41E+09	3.36E+01	4.28E+07	1.36E+08	8.41E+09
14	7.50E+07	7.61E+09	0.00E+00	3.52E+07	1.15E+08	7.61E+09
16	6.92E+07	6.94E+09	0.00E+00	2.97E+07	9.97E+07	6.94E+09
18	6.06E+07	6.07E+09	0.00E+00	2.54E+07	8.78E+07	6.07E+09
20	5.68E+07	5.65E+09	0.00E+00	2.21E+07	7.82E+07	5.65E+09

**Table 5.12:** SPENVIS – displacement damage dose for Gallium Arsenide (GaAs) for a 5-year mission

SHIELDING	LEO MAX ENVELOPE	3000 km 0°	17000 km 0°	GEO	MOLNIYA	SYNTHETIC ORBIT
[mm]	[MeV/g]	[MeV/g]	[MeV/g]	[MeV/g]	[MeV/g]	[MeV/g]
5.00E-02	3.67E+09	4.89E+11	1.49E+12	9.28E+09	1.28E+12	1.49E+12
1.00E-01	2.10E+09	4.33E+11	8.50E+10	5.48E+09	4.84E+11	4.84E+11
2.00E-01	1.15E+09	3.73E+11	2.43E+09	3.04E+09	1.59E+11	3.73E+11
3.00E-01	8.41E+08	3.32E+11	2.91E+08	2.13E+09	8.38E+10	3.32E+11
4.00E-01	6.82E+08	2.71E+11	7.08E+07	1.68E+09	5.19E+10	2.71E+11
5.00E-01	5.90E+08	2.28E+11	2.17E+07	1.36E+09	3.61E+10	2.28E+11
6.00E-01	5.23E+08	1.95E+11	8.04E+06	1.17E+09	2.59E+10	1.95E+11
8.00E-01	4.28E+08	1.47E+11	3.81E+06	8.95E+08	1.47E+10	1.47E+11
1.00E+00	3.75E+08	1.15E+11	3.47E+06	7.18E+08	9.75E+09	1.15E+11
1.50E+00	2.94E+08	6.61E+10	2.47E+06	4.91E+08	3.91E+09	6.61E+10
2.00E+00	2.58E+08	4.92E+10	2.47E+06	3.78E+08	2.44E+09	4.92E+10
2.50E+00	2.28E+08	3.58E+10	2.47E+06	3.00E+08	1.53E+09	3.58E+10
3.00E+00	2.13E+08	3.22E+10	2.47E+06	2.51E+08	1.26E+09	3.22E+10
4.00E+00	1.91E+08	2.60E+10	2.46E+06	1.84E+08	8.52E+08	2.60E+10
5.00E+00	1.83E+08	2.10E+10	2.46E+06	1.44E+08	5.93E+08	2.10E+10
6.00E+00	1.77E+08	1.97E+10	2.45E+06	1.21E+08	5.21E+08	1.97E+10
7.00E+00	1.71E+08	1.84E+10	2.44E+06	1.03E+08	4.57E+08	1.84E+10
8.00E+00	1.65E+08	1.72E+10	2.44E+06	8.72E+07	4.00E+08	1.72E+10
9.00E+00	1.61E+08	1.63E+10	2.43E+06	7.73E+07	3.64E+08	1.63E+10
1.00E+01	1.57E+08	1.54E+10	2.43E+06	6.90E+07	3.30E+08	1.54E+10
1.20E+01	1.50E+08	1.38E+10	2.42E+06	5.57E+07	2.73E+08	1.38E+10
1.40E+01	1.43E+08	1.30E+10	2.41E+06	4.70E+07	2.46E+08	1.30E+10
1.60E+01	1.37E+08	1.23E+10	2.39E+06	4.01E+07	2.21E+08	1.23E+10
1.80E+01	1.32E+08	1.17E+10	2.38E+06	3.52E+07	2.04E+08	1.17E+10
2.00E+01	1.27E+08	1.12E+10	2.37E+06	3.09E+07	1.88E+08	1.12E+10

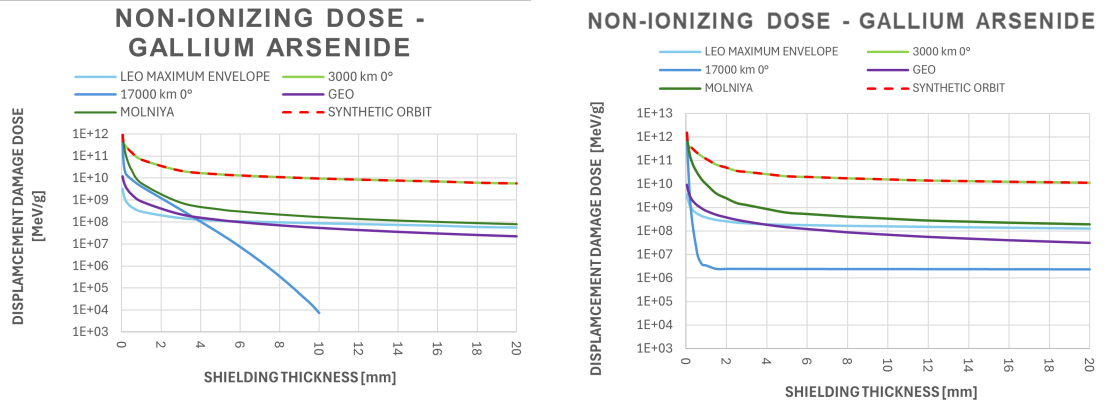


**Figure 5.6:** Non-ionizing dose depth curve for GaAs target material: results from OMERE are shown on the left, while SPENVIS results are shown on the right

In addition to silicon, Gallium Arsenide (GaAs) was also evaluated in terms of Displacement Damage Dose (DDD) across the same orbital configurations and shielding thicknesses, using both **OMERE** and **SPENVIS**. The goal was to assess

whether tool discrepancies persist when shifting to alternative target materials and how they influence technology selection during radiation hardness assurance.

- As observed for Si, both tools consistently identify **MEO orbits** as worst-case environments for GaAs as well, with negligible contribution from GEO or LEO.
- For **minimal shielding** ( $<0.1$  mm), the values diverge more strongly: SPENVIS consistently reports **higher peak values** (up to +30%) compared to OMERE in the unshielded case. For example, at 0.05 mm, SPENVIS reports  $1.49 \times 10^{12}$  MeV/g, while OMERE gives  $9.83 \times 10^{11}$  MeV/g.
- Between **1 and 10 mm**, both tools converge around similar DDD trends, with OMERE generally slightly more conservative below 3 mm and SPENVIS dominating above 4 mm in some cases.
- For **higher shielding** ( $>10$  mm), DDD values flatten and both tools become consistent within  $\sim 10\%$ , with slightly lower absolute values for GaAs compared to Si due to differences in NIEL curve normalization.

This section presents a comparative analysis of the Displacement Damage Dose (DDD) experienced by two key semiconductor materials, **Silicon (Si)** and **Gallium Arsenide (GaAs)**, over a 5-year mission, under solar minimum conditions, using results obtained from the **OMERE** simulation tool. The data are provided as a function of aluminum shielding thickness across representative orbital environments (LEO, MEO, GEO, Molniya).

#### **Common Trends Observed in Both Materials:**

- The **3000 km orbit** (MEO) consistently emerges as the **dominant source of DDD** for both Si and GaAs across all shielding levels. This orbit lies within the heart of the inner Van Allen belt, where high-energy trapped protons are densely concentrated.
- For both materials, the **damage dose decreases monotonically** with increasing shielding, confirming the effectiveness of aluminum in attenuating the low- to mid-energy proton fluxes responsible for displacement damage.
- **GEO and LEO contributions** remain marginal in all cases, with DDD levels typically one to two orders of magnitude lower than those found in MEO or Molniya orbits.
- The **Molniya orbit**, due to its repeated traversal of the inner belt, contributes significantly at low shielding thicknesses (e.g.,  $9.83 \times 10^{11}$  MeV/g for GaAs at 0.05 mm), but its influence quickly diminishes with increased shielding.

- At **high shielding levels** (above 12 mm), both materials show **saturation behavior**, with DDD values flattening around  $10^8$  MeV/g. This indicates that additional shielding yields marginal improvements, as most low- and medium-energy particles have already been absorbed.

#### Material-Specific Differences:

- Across all environments and shielding levels, **GaAs consistently exhibits lower DDD values** than Si. This is attributed to the inherently **lower NIEL sensitivity** of GaAs compared to silicon, especially at low-to-intermediate energies.
- The difference in damage levels is most apparent at intermediate shielding levels (1–5 mm), where GaAs can show up to **20–30% lower dose** than Si. For instance, at 1 mm, the dose is  $6.82 \times 10^{10}$  MeV/g for GaAs and  $6.89 \times 10^{10}$  MeV/g for Si.
- While the **overall trend in DDD reduction vs. shielding is nearly identical** between the two materials, Si remains the more conservative choice for bounding analysis, especially in critical subsystems where displacement damage may affect lifetime.

## 5.2 SEE Environment

### 5.2.1 GCR fluxes versus LET spectrum calculated for an Aluminium shield thickness of 3 mm

In order to assess the impact of galactic cosmic rays (GCRs) on spacecraft electronics, it is essential to characterize the integral particle fluxes as a function of the linear energy transfer (LET) spectrum. This characterization enables the estimation of single-event effect (SEE) rates and the evaluation of shielding effectiveness. Tables 5.13 and 5.14 present the GCR integral fluxes computed using OMERE and SPENVIS respectively, for an isotropic environment and an aluminium shielding thickness of 3 mm.

**Table 5.13:** OMERE – GCR integral fluxes

LET	LEO MAX ENVELOPE	GEO	MOLNIYA	SYNTHETIC ORBIT
[MeV·cm <sup>2</sup> /g]	[#/cm <sup>2</sup> /s]	[#/cm <sup>2</sup> /s]	[#/cm <sup>2</sup> /s]	[#/cm <sup>2</sup> /s]
1.61E+00	1.65E+00	4.59E+00	4.59E+00	4.59E+00
2.63E+00	3.56E-01	1.11E+00	1.11E+00	1.11E+00
3.21E+00	2.81E-01	8.36E-01	8.36E-01	8.36E-01
4.64E+00	2.19E-01	6.02E-01	6.02E-01	6.02E-01
1.00E+01	5.63E-02	1.77E-01	1.77E-01	1.77E-01
5.56E+01	1.49E-02	3.81E-02	3.81E-02	3.81E-02
2.16E+02	3.78E-03	9.99E-03	9.99E-03	9.99E-03
6.03E+02	1.16E-03	3.08E-03	3.08E-03	3.08E-03
8.61E+02	8.58E-04	2.23E-03	2.23E-03	2.23E-03
1.31E+03	3.30E-04	9.99E-04	9.99E-04	9.99E-04
1.96E+03	1.17E-04	3.91E-04	3.91E-04	3.91E-04
3.20E+03	3.90E-05	1.35E-04	1.35E-04	1.35E-04
4.63E+03	1.70E-05	5.96E-05	5.96E-05	5.96E-05
1.54E+04	8.89E-07	3.15E-06	3.15E-06	3.15E-06
2.20E+04	2.78E-07	9.83E-07	9.83E-07	9.83E-07
2.84E+04	1.26E-08	4.44E-08	4.44E-08	4.44E-08
3.14E+04	4.60E-10	1.55E-09	1.55E-09	1.55E-09
3.63E+04	1.94E-10	6.44E-10	6.44E-10	6.44E-10
5.93E+04	2.97E-11	9.74E-11	9.74E-11	9.74E-11
8.47E+04	2.63E-12	8.60E-12	8.60E-12	8.60E-12
9.26E+04	2.47E-13	8.02E-13	8.02E-13	8.02E-13
1.02E+05	2.12E-14	6.85E-14	6.85E-14	6.85E-14
1.06E+05	0.00E+00	0.00E+00	0.00E+00	0.00E+00

**Table 5.14:** SPENVIS – GCR integral fluxes

LET	LEO MAX ENVELOPE	GEO	MOLNIYA	SYNTHETIC ORBIT
[MeV·cm <sup>2</sup> /g]	[#/cm <sup>2</sup> /s]	[#/cm <sup>2</sup> /s]	[#/cm <sup>2</sup> /s]	[#/cm <sup>2</sup> /s]
1.61E+00	1.61E+00	4.45E+00	4.45E+00	4.45E+00
2.63E+00	3.53E-01	1.09E+00	1.09E+00	1.09E+00
3.21E+00	2.81E-01	8.22E-01	8.22E-01	8.22E-01
4.64E+00	2.19E-01	5.85E-01	5.85E-01	5.85E-01
1.00E+01	5.55E-02	1.69E-01	1.69E-01	1.69E-01
5.56E+01	1.49E-02	3.66E-02	3.66E-02	3.66E-02
2.16E+02	3.72E-03	9.57E-03	9.57E-03	9.57E-03
6.03E+02	1.16E-03	3.00E-03	3.00E-03	3.00E-03
8.61E+02	8.49E-04	2.16E-03	2.16E-03	2.16E-03
1.31E+03	2.87E-04	8.77E-04	8.77E-04	8.77E-04
1.96E+03	1.12E-04	3.69E-04	3.69E-04	3.69E-04
3.20E+03	3.85E-05	1.33E-04	1.33E-04	1.33E-04
4.63E+03	1.71E-05	5.98E-05	5.98E-05	5.98E-05
1.54E+04	9.44E-07	3.35E-06	3.35E-06	3.35E-06
2.20E+04	3.28E-07	1.16E-06	1.16E-06	1.16E-06
2.84E+04	6.24E-08	2.20E-07	2.20E-07	2.20E-07
3.14E+04	2.23E-09	7.70E-09	7.70E-09	7.70E-09
3.63E+04	2.61E-10	8.36E-10	8.36E-10	8.36E-10
5.93E+04	5.30E-11	1.69E-10	1.69E-10	1.69E-10
8.47E+04	9.02E-12	2.86E-11	2.86E-11	2.86E-11
9.26E+04	4.50E-12	1.43E-11	1.43E-11	1.43E-11
1.02E+05	7.32E-13	2.32E-12	2.32E-12	2.32E-12
1.06E+05	1.59E-13	5.04E-13	5.04E-13	5.04E-13

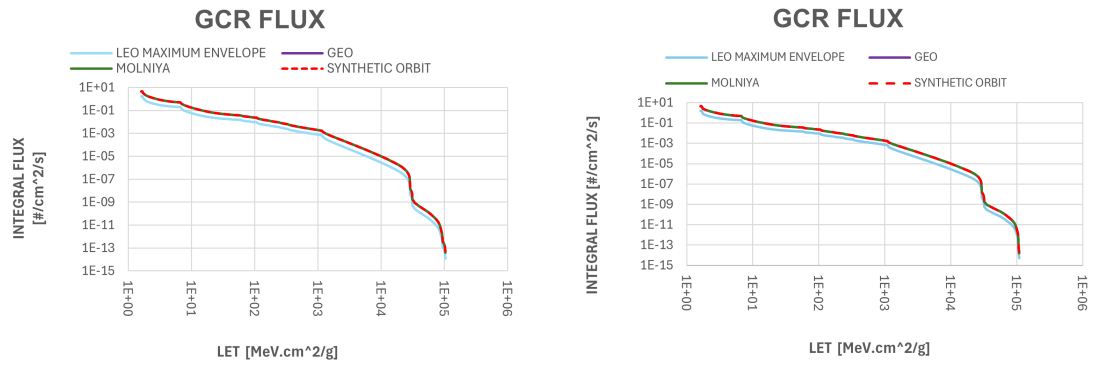


**Figure 5.7:** GCR Fluxes: results from OMERE are shown on the left, while SPENVIS results are shown on the right

A comparison of the results obtained using SPENVIS and OMERE for Galactic Cosmic Ray (GCR) integral fluxes was carried out across four orbital environments: LEO, GEO, Molniya and a synthetic orbit identified as the worst-case scenario. These environments were analyzed assuming the same solar minimum conditions and using the same LET bins. However, slight discrepancies may arise due to interpolation procedures and differences in the resolution of the LET grid between the two tools.

The synthetic orbit, intended to model an unshielded trajectory with constant exposure to cosmic rays, is considered the worst-case scenario for GCRs. It is worth noting that the Molniya orbit was modeled to represent a completely unshielded case for GCRs and this assumption led to obtain the same results as for GEO, while the MEO orbit, omitted here, was modeled as fully shielded by the geomagnetic field, resulting in negligible GCR exposure.

A careful comparison of the results reveals the following:

- Across all LET values, OMERE systematically reports slightly higher flux values than SPENVIS, with differences generally within 10%, especially for lower LET values. This difference becomes progressively more significant at higher LET values, particularly in the LEO environment. For instance, beyond  $20,000 \text{ MeV} \cdot \text{cm}^2/\text{g}$ , OMERE begins to diverge from SPENVIS more sharply, reaching an order-of-magnitude difference at very high LETs (e.g., above  $80,000 \text{ MeV} \cdot \text{cm}^2/\text{g}$ ).
- In the GEO, Molniya and synthetic orbits, where GCR exposure is not mitigated by Earth's magnetic field, both tools yield very similar results across most LET bins, although OMERE still maintains slightly higher flux values.
- The maximum relative difference is observed in the LEO environment due to the stronger effect of the geomagnetic cutoff. In this case, OMERE seems to model a slightly less effective shielding, resulting in higher GCR fluxes, especially in the tail of the LET distribution.

It is worth noting that both tools agree on the shape of the integral flux curves and the relative dominance of each orbit. The synthetic orbit, Molniya and GEO environments all converge to similar flux values, confirming their comparable exposure to cosmic radiation. LEO remains the most shielded, with the lowest GCR fluxes, especially for higher LETs.

Overall, despite the minor discrepancies, most likely due to differences in geomagnetic shielding modeling, interpolation methods or integration of the GCR spectra, both tools provide consistent outputs that allow for a robust evaluation of worst-case scenarios. OMERE tends to provide slightly more conservative estimates, which could be beneficial in critical applications such as Radiation Hardness Assurance.



## 5.2.2 Solar particle event fluxes versus LET spectrum for a given Aluminium shield thickness of 3 mm

To evaluate the vulnerability of spacecraft electronics during solar particle events (SPEs), it is crucial to model the integral particle fluxes as a function of the linear energy transfer (LET) spectrum. This enables accurate predictions of the probability and severity of single-event effects (SEEs) in different mission environments. Tables 5.15 and 5.16 present the SEP integral fluxes obtained using OMERE and SPENVIS, respectively, for an aluminium shielding thickness of 3 mm.

In addition, Tables 5.17 and 5.18 report the worst-case 5-minute integral flux levels derived from each tool, representing extreme short-duration SEP events. These brief but intense fluxes are particularly relevant for evaluating peak SEE rates and for determining the resilience of spacecraft systems to transient, high-radiation bursts.

**Table 5.15:** OMERE – solar energetic particle (SEP) integral fluxes

LET	LEO MAX ENVELOPE	GEO	MOLNIYA	SYNTHETIC ORBIT
[MeV·cm <sup>2</sup> /g]	[#/cm <sup>2</sup> /s]	[#/cm <sup>2</sup> /s]	[#/cm <sup>2</sup> /s]	[#/cm <sup>2</sup> /s]
1.61E+00	8.54E+01	3.42E+02	3.42E+02	3.42E+02
2.63E+00	8.54E+01	3.42E+02	3.42E+02	3.42E+02
3.21E+00	8.52E+01	3.41E+02	3.41E+02	3.41E+02
4.64E+00	8.29E+01	3.33E+02	3.33E+02	3.33E+02
1.00E+01	6.41E+01	2.60E+02	2.60E+02	2.60E+02
5.56E+01	5.00E+00	2.06E+01	2.06E+01	2.06E+01
2.16E+02	2.17E-01	9.03E-01	9.03E-01	9.03E-01
6.03E+02	5.88E-03	2.59E-02	2.59E-02	2.59E-02
8.61E+02	2.93E-03	1.29E-02	1.29E-02	1.29E-02
1.31E+03	1.15E-03	5.05E-03	5.05E-03	5.05E-03
1.96E+03	3.97E-04	1.74E-03	1.74E-03	1.74E-03
3.20E+03	1.63E-04	7.19E-04	7.19E-04	7.19E-04
4.63E+03	7.55E-05	3.32E-04	3.32E-04	3.32E-04
1.54E+04	1.82E-06	8.02E-06	8.02E-06	8.02E-06
2.20E+04	6.16E-07	2.71E-06	2.71E-06	2.71E-06
2.84E+04	3.52E-08	1.55E-07	1.55E-07	1.55E-07
3.14E+04	4.31E-10	1.89E-09	1.89E-09	1.89E-09
3.63E+04	1.08E-10	4.73E-10	4.73E-10	4.73E-10
5.93E+04	1.49E-11	6.54E-11	6.54E-11	6.54E-11
8.47E+04	2.26E-12	9.93E-12	9.93E-12	9.93E-12
9.26E+04	2.07E-13	9.10E-13	9.10E-13	9.10E-13
1.02E+05	2.94E-15	1.29E-14	1.29E-14	1.29E-14
1.06E+05	0.00E+00	0.00E+00	0.00E+00	0.00E+00

**Table 5.16:** SPENVIS – solar energetic particle (SEP) integral fluxes

LET	LEO MAX ENVELOPE	GEO	MOLNIYA	SYNTHETIC ORBIT
[MeV.cm <sup>2</sup> /g]	[#/cm <sup>2</sup> /s]	[#/cm <sup>2</sup> /s]	[#/cm <sup>2</sup> /s]	[#/cm <sup>2</sup> /s]
1.61E+00	6.72E+01	2.74E+02	2.74E+02	2.74E+02
2.63E+00	6.71E+01	2.73E+02	2.73E+02	2.73E+02
3.21E+00	6.67E+01	2.72E+02	2.72E+02	2.72E+02
4.64E+00	6.50E+01	2.65E+02	2.65E+02	2.65E+02
1.00E+01	5.02E+01	2.07E+02	2.07E+02	2.07E+02
5.56E+01	3.84E+00	1.63E+01	1.63E+01	1.63E+01
2.16E+02	1.75E-01	7.33E-01	7.33E-01	7.33E-01
6.03E+02	5.86E-03	2.26E-02	2.26E-02	2.26E-02
8.61E+02	2.90E-03	1.11E-02	1.11E-02	1.11E-02
1.31E+03	1.08E-03	4.15E-03	4.15E-03	4.15E-03
1.96E+03	4.14E-04	1.58E-03	1.58E-03	1.58E-03
3.20E+03	1.75E-04	6.64E-04	6.64E-04	6.64E-04
4.63E+03	8.02E-05	3.02E-04	3.02E-04	3.02E-04
1.54E+04	2.05E-06	7.27E-06	7.27E-06	7.27E-06
2.20E+04	7.60E-07	2.68E-06	2.68E-06	2.68E-06
2.84E+04	1.83E-07	6.44E-07	6.44E-07	6.44E-07
3.14E+04	6.04E-09	2.11E-08	2.11E-08	2.11E-08
3.63E+04	1.71E-10	5.56E-10	5.56E-10	5.56E-10
5.93E+04	3.04E-11	9.70E-11	9.70E-11	9.70E-11
8.47E+04	6.46E-12	2.05E-11	2.05E-11	2.05E-11
9.26E+04	3.92E-12	1.24E-11	1.24E-11	1.24E-11
1.02E+05	1.02E-12	3.22E-12	3.22E-12	3.22E-12
1.06E+05	2.35E-13	7.45E-13	7.45E-13	7.45E-13

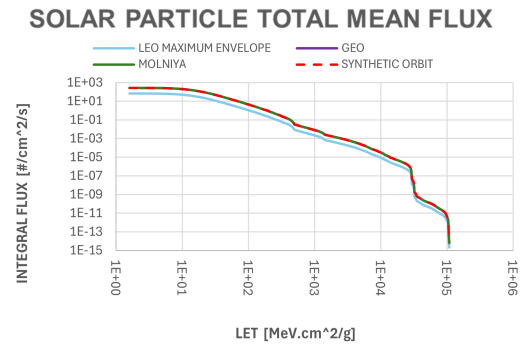
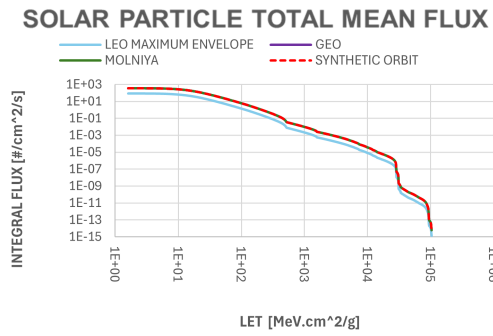


**Figure 5.8:** SEP Fluxes: results from OMERE are shown on the left, while SPENVIS results are shown on the right

**Table 5.17:** OMERE – Solar Particle Worst-Case 5-Minute Integral Flux

LET	LEO MAX ENVELOPE	GEO	MOLNIYA	SYNTHETIC ORBIT
[MeV·cm <sup>2</sup> /g]	[#/cm <sup>2</sup> /s]	[#/cm <sup>2</sup> /s]	[#/cm <sup>2</sup> /s]	[#/cm <sup>2</sup> /s]
1.61E+00	7.53E+04	3.11E+05	3.11E+05	3.11E+05
2.63E+00	7.51E+04	3.11E+05	3.11E+05	3.11E+05
3.21E+00	7.47E+04	3.09E+05	3.09E+05	3.09E+05
4.64E+00	7.33E+04	3.04E+05	3.04E+05	3.04E+05
1.00E+01	6.10E+04	2.55E+05	2.55E+05	2.55E+05
5.56E+01	5.52E+03	2.32E+04	2.32E+04	2.32E+04
2.16E+02	2.22E+02	9.32E+02	9.32E+02	9.32E+02
6.03E+02	2.22E+00	8.72E+00	8.72E+00	8.72E+00
8.61E+02	1.03E+00	4.00E+00	4.00E+00	4.00E+00
1.31E+03	3.58E-01	1.37E+00	1.37E+00	1.37E+00
1.96E+03	1.07E-01	3.93E-01	3.93E-01	3.93E-01
3.20E+03	5.09E-02	1.86E-01	1.86E-01	1.86E-01
4.63E+03	2.73E-02	9.87E-02	9.87E-02	9.87E-02
1.54E+04	1.49E-03	5.27E-03	5.27E-03	5.27E-03
2.20E+04	5.02E-04	1.77E-03	1.77E-03	1.77E-03
2.84E+04	2.65E-05	9.35E-05	9.35E-05	9.35E-05
3.14E+04	3.30E-07	1.13E-06	1.13E-06	1.13E-06
3.63E+04	8.68E-08	2.91E-07	2.91E-07	2.91E-07
5.93E+04	8.99E-09	2.95E-08	2.95E-08	2.95E-08
8.47E+04	1.29E-09	4.22E-09	4.22E-09	4.22E-09
9.26E+04	1.15E-10	3.75E-10	3.75E-10	3.75E-10
1.02E+05	3.84E-12	1.24E-11	1.24E-11	1.24E-11
1.06E+05	0.00E+00	0.00E+00	0.00E+00	0.00E+00

**Table 5.18:** SPENVIS – Solar Particle Worst-Case 5-Minute Integral Flux

LET	LEO MAX ENVELOPE	GEO	MOLNIYA	SYNTHETIC ORBIT
[MeV·cm <sup>2</sup> /g]	[#/cm <sup>2</sup> /s]	[#/cm <sup>2</sup> /s]	[#/cm <sup>2</sup> /s]	[#/cm <sup>2</sup> /s]
1.61E+00	3.59E+04	1.47E+05	1.47E+05	1.47E+05
2.63E+00	3.59E+04	1.47E+05	1.47E+05	1.47E+05
3.21E+00	3.58E+04	1.47E+05	1.47E+05	1.47E+05
4.64E+00	3.53E+04	1.45E+05	1.45E+05	1.45E+05
1.00E+01	2.92E+04	1.21E+05	1.21E+05	1.21E+05
5.56E+01	2.46E+03	1.05E+04	1.05E+04	1.05E+04
2.16E+02	1.06E+02	4.47E+02	4.47E+02	4.47E+02
6.03E+02	2.17E+00	8.37E+00	8.37E+00	8.37E+00
8.61E+02	9.65E-01	3.71E+00	3.71E+00	3.71E+00
1.31E+03	2.88E-01	1.10E+00	1.10E+00	1.10E+00
1.96E+03	8.37E-02	3.14E-01	3.14E-01	3.14E-01
3.20E+03	4.13E-02	1.52E-01	1.52E-01	1.52E-01
4.63E+03	2.24E-02	8.18E-02	8.18E-02	8.18E-02
1.54E+04	1.53E-03	5.41E-03	5.41E-03	5.41E-03
2.20E+04	5.79E-04	2.04E-03	2.04E-03	2.04E-03
2.84E+04	1.38E-04	4.88E-04	4.88E-04	4.88E-04
3.14E+04	2.99E-06	1.04E-05	1.04E-05	1.04E-05
3.63E+04	1.23E-07	4.04E-07	4.04E-07	4.04E-07
5.93E+04	1.86E-08	5.95E-08	5.95E-08	5.95E-08
8.47E+04	3.18E-09	1.01E-08	1.01E-08	1.01E-08
9.26E+04	1.94E-09	6.17E-09	6.17E-09	6.17E-09
1.02E+05	4.62E-10	1.46E-09	1.46E-09	1.46E-09
1.06E+05	1.07E-10	3.39E-10	3.39E-10	3.39E-10

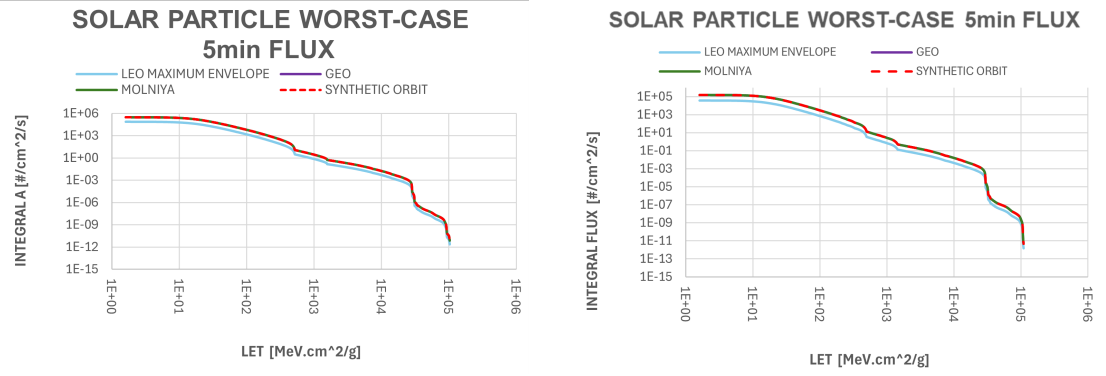


**Figure 5.9:** SEP Fluxes in the worst-case 5-minutes condition: results from OMERE are shown on the left, while SPENVIS results are shown on the right

A comparative evaluation of SEP integral fluxes as a function of LET was conducted using both OMERE and SPENVIS for two different cases: a typical medium SEP event and a worst-case 5-minute peak event. The analysis considered four orbital environments: LEO, GEO and Molniya, from which a synthetic orbit representing a continuous, unshielded path, was derived. As in the GCR analysis, MEO is excluded here due to its full geomagnetic shielding and Molniya is treated identically to GEO, assuming full exposure to the solar particle environment.

For the medium event scenario, both tools display the same general spectral behavior across all orbits. However, OMERE consistently predicts higher integral fluxes than SPENVIS across the LET spectrum, particularly for LEO. At low LET values (e.g., below  $10 \text{ MeV} \cdot \text{cm}^2/\text{g}$ ), OMERE yields fluxes around 20–25% higher than SPENVIS, with this discrepancy gradually decreasing at higher LETs. In the synthetic orbit, the two tools align more closely, with differences generally within 10–15%, though OMERE still maintains a slightly more conservative profile. The synthetic orbit, GEO and Molniya show identical results as expected due to the modeling assumption of full exposure. In contrast, LEO sees lower fluxes due to geomagnetic shielding, though OMERE estimates higher residual fluxes than SPENVIS in this orbit too.

In the worst-case 5-minute scenario, the differences between the tools become even more pronounced. OMERE predicts SEP fluxes that are roughly twice as high as those from SPENVIS at all LET values and for all exposed orbits. For instance, at  $1.61 \text{ MeV} \cdot \text{cm}^2/\text{g}$ , OMERE reports a GEO flux of approximately  $3.11 \times 10^5$  particles/cm<sup>2</sup>/s, compared to SPENVIS'  $1.47 \times 10^5$ , more than a twofold increase. This ratio remains consistent across the entire LET spectrum, even at high LET values above  $50,000 \text{ MeV} \cdot \text{cm}^2/\text{g}$ . In LEO, where shielding reduces the fluxes, OMERE again yields significantly higher predictions, maintaining its tendency to offer more conservative estimates.

The spectral shapes remain nearly identical between tools, but the magnitudes diverge significantly, especially in the high-flux, low-LET region. These differences likely stem from how each tool models the SEP event profile, particle energy spectra and transport through shielding. OMERE's predictions, especially in critical cases like the 5-minute peak event, represent a substantially more pessimistic approach, which may be advantageous in conservative spacecraft design, particularly for worst-case Total Ionizing Dose and Single Event Effect evaluations.

Overall, the tools are in agreement about the relative severity of each orbital scenario. The synthetic orbit and GEO (along with Molniya) consistently present the most severe radiation environments, while LEO benefits from natural shielding. OMERE's consistently higher outputs suggest a design philosophy on the side of caution, especially valuable for radiation hardness assurance planning under high-risk solar activity conditions.

### **5.2.3 Trapped and solar protons shielded fluxes versus energy spectra behind 3 mm of Aluminium**

Understanding the energy-dependent attenuation of protons is fundamental to evaluating spacecraft component survivability. Tables 5.19 and 5.20 present the integral fluxes of shielded protons computed using OMERE and SPENVIS, respectively, for an aluminium shielding thickness of 3 mm. These tables illustrate how each tool models the energy spectra of protons after shielding and help quantify the effectiveness of passive shielding strategies across a wide energy range.

**Table 5.19:** OMERE – shielded proton integral flux

ENERGY	LEO MAX ENVELOPE	3000 km 0°	17000 km 0°	GEO	MOLNIYA	SYNTHETIC ORBIT
[MeV]	[#/cm <sup>2</sup> /s]	[#/cm <sup>2</sup> /s]	[#/cm <sup>2</sup> /s]	[#/cm <sup>2</sup> /s]	[#/cm <sup>2</sup> /s]	[#/cm <sup>2</sup> /s]
1.00E-02	3.15E+02	3.63E+04	0.00E+00	3.42E+02	1.20E+03	3.63E+04
1.26E-02	3.15E+02	3.63E+04	0.00E+00	3.42E+02	1.20E+03	3.63E+04
1.58E-02	3.15E+02	3.63E+04	0.00E+00	3.42E+02	1.20E+03	3.63E+04
2.00E-02	3.15E+02	3.63E+04	0.00E+00	3.42E+02	1.20E+03	3.63E+04
2.51E-02	3.15E+02	3.63E+04	0.00E+00	3.42E+02	1.20E+03	3.63E+04
3.16E-02	3.15E+02	3.63E+04	0.00E+00	3.42E+02	1.20E+03	3.63E+04
3.98E-02	3.15E+02	3.63E+04	0.00E+00	3.42E+02	1.20E+03	3.63E+04
5.01E-02	3.15E+02	3.63E+04	0.00E+00	3.42E+02	1.20E+03	3.63E+04
6.31E-02	3.15E+02	3.63E+04	0.00E+00	3.42E+02	1.20E+03	3.63E+04
7.94E-02	3.15E+02	3.63E+04	0.00E+00	3.42E+02	1.20E+03	3.63E+04
1.00E-01	3.14E+02	3.63E+04	0.00E+00	3.42E+02	1.20E+03	3.63E+04
2.50E-01	3.14E+02	3.63E+04	0.00E+00	3.42E+02	1.20E+03	3.63E+04
5.00E-01	3.14E+02	3.63E+04	0.00E+00	3.42E+02	1.20E+03	3.63E+04
7.50E-01	3.13E+02	3.62E+04	0.00E+00	3.41E+02	1.20E+03	3.62E+04
1.00E+00	3.13E+02	3.62E+04	0.00E+00	3.41E+02	1.19E+03	3.62E+04
2.00E+00	3.09E+02	3.60E+04	0.00E+00	3.38E+02	1.18E+03	3.60E+04
3.00E+00	3.04E+02	3.57E+04	0.00E+00	3.35E+02	1.16E+03	3.57E+04
4.00E+00	2.99E+02	3.54E+04	0.00E+00	3.31E+02	1.14E+03	3.54E+04
5.00E+00	2.92E+02	3.50E+04	0.00E+00	3.25E+02	1.11E+03	3.50E+04
6.00E+00	2.85E+02	3.45E+04	0.00E+00	3.20E+02	1.08E+03	3.45E+04
8.00E+00	2.70E+02	3.35E+04	0.00E+00	3.07E+02	1.02E+03	3.35E+04
1.00E+01	2.54E+02	3.24E+04	0.00E+00	2.92E+02	9.52E+02	3.24E+04
1.20E+01	2.40E+02	3.12E+04	0.00E+00	2.77E+02	8.85E+02	3.12E+04
1.50E+01	2.26E+02	2.96E+04	0.00E+00	2.54E+02	7.92E+02	2.96E+04
1.70E+01	2.21E+02	2.85E+04	0.00E+00	2.38E+02	7.36E+02	2.85E+04
2.00E+01	2.16E+02	2.71E+04	0.00E+00	2.17E+02	6.62E+02	2.71E+04
2.50E+01	2.08E+02	2.49E+04	0.00E+00	1.83E+02	5.58E+02	2.49E+04
3.00E+01	2.00E+02	2.30E+04	0.00E+00	1.55E+02	4.73E+02	2.30E+04
3.50E+01	1.91E+02	2.12E+04	0.00E+00	1.31E+02	4.02E+02	2.12E+04
4.00E+01	1.83E+02	1.95E+04	0.00E+00	1.12E+02	3.42E+02	1.95E+04
4.50E+01	1.75E+02	1.82E+04	0.00E+00	9.54E+01	2.96E+02	1.82E+04
5.00E+01	1.67E+02	1.70E+04	0.00E+00	8.20E+01	2.60E+02	1.70E+04
6.00E+01	1.51E+02	1.50E+04	0.00E+00	6.14E+01	2.05E+02	1.50E+04
7.00E+01	1.36E+02	1.33E+04	0.00E+00	4.66E+01	1.64E+02	1.33E+04
8.00E+01	1.21E+02	1.18E+04	0.00E+00	3.60E+01	1.33E+02	1.18E+04
9.00E+01	1.08E+02	1.04E+04	0.00E+00	2.82E+01	1.09E+02	1.04E+04
1.00E+02	9.64E+01	9.21E+03	0.00E+00	2.25E+01	9.03E+01	9.21E+03
1.25E+02	7.09E+01	6.66E+03	0.00E+00	1.30E+01	5.65E+01	6.66E+03
1.50E+02	5.11E+01	4.72E+03	0.00E+00	7.87E+00	3.55E+01	4.72E+03
1.75E+02	3.60E+01	3.25E+03	0.00E+00	4.85E+00	2.18E+01	3.25E+03
2.00E+02	2.44E+01	2.16E+03	0.00E+00	2.97E+00	1.32E+01	2.16E+03
2.76E+02	2.18E+00	1.88E+02	0.00E+00	2.41E-01	1.06E+00	1.88E+02
3.00E+02	0.00E+00	0.00E+00	0.00E+00	0.00E+00	0.00E+00	0.00E+00

Table 5.20: SPENVIS – shielded proton integral flux

ENERGY	LEO MAX ENVELOPE	3000 km 0°	17000 km 0°	GEO	MOLNIYA	SYNTHETIC ORBIT
[MeV]	[#/cm <sup>2</sup> /s]	[#/cm <sup>2</sup> /s]	[#/cm <sup>2</sup> /s]	[#/cm <sup>2</sup> /s]	[#/cm <sup>2</sup> /s]	[#/cm <sup>2</sup> /s]
4,00E-02	2,27E+02	2,30E+04	7,88E-01	1,29E+02	5,38E+02	2,30E+04
1,00E-01	2,27E+02	2,30E+04	7,88E-01	1,29E+02	5,38E+02	2,30E+04
2,00E-01	2,27E+02	2,30E+04	7,88E-01	1,29E+02	5,38E+02	2,30E+04
3,00E-01	2,27E+02	2,30E+04	7,88E-01	1,29E+02	5,38E+02	2,30E+04
4,00E-01	2,27E+02	2,30E+04	7,88E-01	1,29E+02	5,38E+02	2,30E+04
5,00E-01	2,27E+02	2,30E+04	7,88E-01	1,29E+02	5,38E+02	2,30E+04
6,00E-01	2,27E+02	2,30E+04	7,88E-01	1,29E+02	5,38E+02	2,30E+04
7,00E-01	2,27E+02	2,30E+04	7,88E-01	1,29E+02	5,38E+02	2,30E+04
8,00E-01	2,27E+02	2,30E+04	7,88E-01	1,29E+02	5,38E+02	2,30E+04
1,00E+00	2,27E+02	2,29E+04	7,88E-01	1,29E+02	5,38E+02	2,29E+04
1,25E+00	2,27E+02	2,29E+04	7,88E-01	1,29E+02	5,38E+02	2,29E+04
1,50E+00	2,27E+02	2,29E+04	7,88E-01	1,29E+02	5,38E+02	2,29E+04
1,75E+00	2,27E+02	2,29E+04	7,88E-01	1,29E+02	5,37E+02	2,29E+04
2,00E+00	2,27E+02	2,29E+04	7,88E-01	1,29E+02	5,37E+02	2,29E+04
2,25E+00	2,27E+02	2,29E+04	7,88E-01	1,29E+02	5,37E+02	2,29E+04
2,50E+00	2,27E+02	2,29E+04	7,88E-01	1,29E+02	5,37E+02	2,29E+04
2,75E+00	2,27E+02	2,29E+04	7,88E-01	1,29E+02	5,36E+02	2,29E+04
3,00E+00	2,27E+02	2,29E+04	7,88E-01	1,28E+02	5,36E+02	2,29E+04
3,25E+00	2,27E+02	2,29E+04	7,88E-01	1,28E+02	5,36E+02	2,29E+04
3,50E+00	2,27E+02	2,29E+04	7,87E-01	1,28E+02	5,36E+02	2,29E+04
3,75E+00	2,27E+02	2,29E+04	7,87E-01	1,28E+02	5,35E+02	2,29E+04
4,00E+00	2,27E+02	2,29E+04	7,87E-01	1,28E+02	5,35E+02	2,29E+04
4,25E+00	2,27E+02	2,29E+04	7,87E-01	1,28E+02	5,34E+02	2,29E+04
4,50E+00	2,27E+02	2,29E+04	7,87E-01	1,28E+02	5,34E+02	2,29E+04
4,75E+00	2,27E+02	2,28E+04	7,87E-01	1,28E+02	5,34E+02	2,28E+04
5,00E+00	2,27E+02	2,28E+04	7,87E-01	1,28E+02	5,33E+02	2,28E+04
5,50E+00	2,26E+02	2,28E+04	7,87E-01	1,27E+02	5,32E+02	2,28E+04
6,00E+00	2,26E+02	2,28E+04	7,87E-01	1,27E+02	5,31E+02	2,28E+04
6,50E+00	2,26E+02	2,28E+04	7,87E-01	1,27E+02	5,30E+02	2,28E+04
7,00E+00	2,26E+02	2,27E+04	7,87E-01	1,26E+02	5,29E+02	2,27E+04
1,00E+01	2,25E+02	2,25E+04	7,87E-01	1,24E+02	5,20E+02	2,25E+04
2,00E+01	2,19E+02	2,14E+04	7,86E-01	1,10E+02	4,75E+02	2,14E+04
3,00E+01	2,09E+02	1,98E+04	7,86E-01	9,29E+01	4,15E+02	1,98E+04
4,00E+01	1,96E+02	1,81E+04	7,85E-01	7,60E+01	3,58E+02	1,81E+04
5,00E+01	1,82E+02	1,66E+04	7,84E-01	6,12E+01	3,09E+02	1,66E+04
6,00E+01	1,67E+02	1,50E+04	7,83E-01	4,99E+01	2,68E+02	1,50E+04
7,00E+01	1,50E+02	1,33E+04	7,82E-01	3,96E+01	2,27E+02	1,33E+04
8,00E+01	1,34E+02	1,18E+04	7,82E-01	3,11E+01	1,91E+02	1,18E+04
1,00E+02	1,07E+02	9,04E+03	7,80E-01	2,02E+01	1,36E+02	9,04E+03
1,50E+02	6,70E+01	5,10E+03	7,76E-01	9,40E+00	6,96E+01	5,10E+03
2,00E+02	3,96E+01	2,73E+03	7,71E-01	4,98E+00	3,49E+01	2,73E+03
3,00E+02	9,42E+00	5,97E+02	6,19E-01	1,32E+00	7,22E+00	5,97E+02
4,00E+02	1,08E-01	0,00E+00	2,85E-01	3,56E-01	3,56E-01	3,56E-01
5,00E+02	2,83E-02	0,00E+00	8,21E-02	9,44E-02	9,44E-02	9,44E-02
8,00E+02	0,00E+00	0,00E+00	0,00E+00	0,00E+00	0,00E+00	0,00E+00
1,00E+03	0,00E+00	0,00E+00	0,00E+00	0,00E+00	0,00E+00	0,00E+00

The comparison between OMERE and SPENVIS in terms of shielded proton integral fluxes as a function of energy, behind 3 mm of Aluminium shielding, reveals several consistent trends as well as noteworthy differences depending on orbital configuration.

First, both tools confirm that low-altitude orbits, such as the LEO maximum



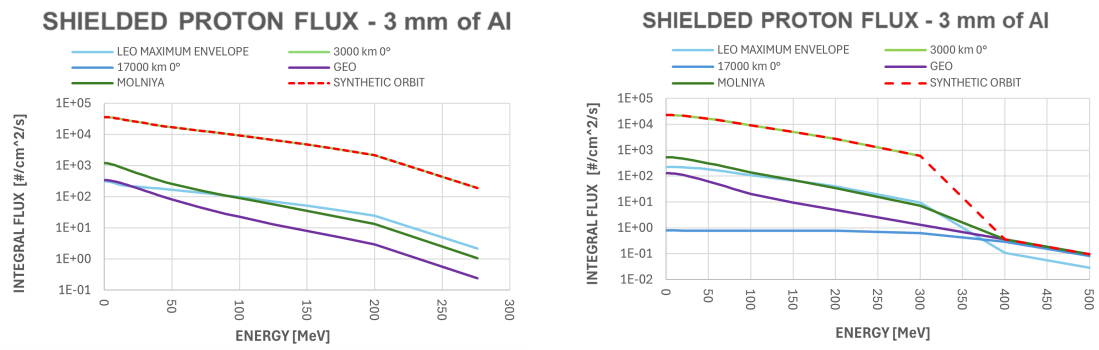


**Figure 5.10:** Shielded proton fluxes: results from OMERE are shown on the left, while SPENVIS results are shown on the right

envelope, are subject to relatively low fluxes of trapped and solar protons, with fluxes around  $3 \times 10^2$  particles/cm<sup>2</sup>/s for energies below 10 MeV. These fluxes progressively decline as energy increases. Notably, OMERE estimates a slightly higher flux baseline in LEO compared to SPENVIS, especially at low energies, with deviations that can reach 30–40% at specific energy bins. The decline with energy follows a similar exponential decay pattern in both tools.

In the GEO and Molniya cases, both environments exhibit significantly elevated proton fluxes due to the limited geomagnetic shielding and higher radiation exposure. OMERE estimates a GEO flux of over  $3.4 \times 10^2$  particles/cm<sup>2</sup>/s at low energies, with a smoother decrease up to around 300 MeV. SPENVIS, on the other hand, produces lower values in this range, about 130 particles/cm<sup>2</sup>/s at 0.1 MeV in GEO, which translates to a discrepancy of approximately 60%, showing the more conservative nature of OMERE seen in prior comparisons.

As expected, the 17,000 km equatorial orbit shows effectively zero flux in OMERE and very low values of the order of  $10^{-1}$  particles/cm<sup>2</sup>/s in SPENVIS. This is consistent with the assumption that MEO is fully shielded from trapped particles due to its specific location in the magnetosphere.

The synthetic orbit, defined to simulate full, continuous exposure to the radiation belts and solar particles, predictably shows the most severe environment. OMERE estimates fluxes that peak around  $3.6 \times 10^4$  particles/cm<sup>2</sup>/s below 1 MeV, remaining an order of magnitude above SPENVIS predictions (which stabilize around  $2.3 \times 10^4$ ).

For Molniya, modeled under the same exposure assumptions as GEO, the two tools again show consistent trends, but OMERE consistently reports higher fluxes across the spectrum, especially in the 1–100 MeV energy range. Differences here typically range from 30% to over 50%, confirming that OMERE maintains a more conservative posture in estimating proton exposure behind shielding.

Across all orbits and tools, the spectral shape remains largely consistent, characterized by a sharp drop in flux with increasing proton energy. This agreement supports the qualitative reliability of both tools in modeling the spectral behavior of shielded protons, even if their quantitative outputs diverge.

In conclusion, OMERE systematically estimates higher shielded proton fluxes than SPENVIS, particularly at low energies and in weakly shielded orbits. This is consistent with the findings in SEP and GCR analyses. For design purposes, OMERE may be considered more conservative and thus more appropriate in contexts requiring worst-case evaluations for radiation hardness assurance.

## Chapter 6

# Radiation Hardness Assurance Across Space Agency Development Phases

### 6.1 Introduction

Radiation Hardness Assurance (RHA) is a comprehensive engineering methodology that ensures the reliable performance of spaceborne electronics throughout their operational lifetime in harsh radiation environments. This chapter provides a technical overview of the RHA process as adopted in ESA space missions [4], linking high-level programmatic phases to detailed radiation modeling, testing and assurance practices. While the foundation of this thesis is grounded in ECSS standards, it also incorporates, with more evidence in this chapter, relevant NASA standards and methodologies, as described in [28], [29] and [53] in order to define a robust and unified approach suitable for ARCap. The objective is to outline an RHA strategy capable of addressing emerging challenges in space radiation engineering, through a structured process that includes hazard definition, hazard evaluation, requirements derivation, assessment of component usage and the systematic application of mitigation techniques, with the active involvement of design engineers throughout the mission lifecycle.

### 6.2 RHA Methodology and Process Overview

The RHA process, as shown in Figure 6.1, is structured as a top-down, iterative workflow. It begins with mission definition and environmental characterization, followed by detailed component testing and design validation. The goal is to ensure

all critical functions of electronic systems remain within operational limits under worst-case conditions. Key radiation effects to consider include:

- **TID**: cumulative energy deposition causing parameter drift or functional failure.
- **DDD**: displacement of atoms from their lattice positions, affecting long-term performance.
- **SEE**: transient or permanent failures from a single energetic particle.

The process adheres to standards such as ECSS-E-ST-10-12 and ECSS-Q-ST-60-15C, ensuring traceability and consistency across mission phases.

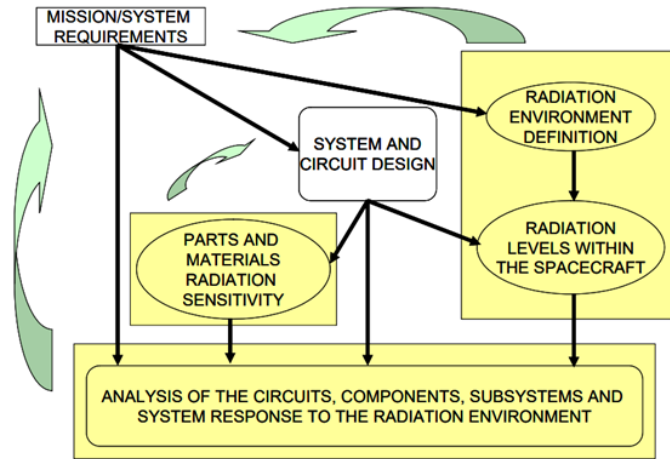


Figure 6.1: RHA process overview [4].

### 6.3 Phase 0/A: Mission Analysis and Feasibility

In Phases 0 and A, the mission radiation environment is initially defined. This involves identifying relevant sources, Galactic Cosmic Rays (GCRs), Solar Energetic Particles (SEPs) and trapped radiation in the Van Allen belts. These inputs are used to tailor Radiation Design Margins (RDM) and initiate trade-offs for technology selection.

Preliminary radiation environment modeling tools such as SPENVIS or OMERE are employed to generate estimates of dose and particle flux. These values guide early subsystem and component evaluations. This phase also defines key orbital parameters, including altitude and inclination, which affect the intensity and variability of the radiation environment.

## 6.4 Phase B: Preliminary Definition

In Phase B, the radiation environment is finalized and the mission-level RHA requirements are translated into subsystem and component requirements. Spacecraft layout is frozen, enabling more accurate internal shielding modeling. Component-level characterization begins and candidate EEE parts are screened based on prior test data and radiation tolerance.

The RHA activities during Phase B support the System Requirements Review (SRR) and include initial shielding design and definition of SEE test campaigns. Flux maps and dose estimates are refined using sector analysis or Monte Carlo-based methods, incorporating early models of internal geometry and material distribution.

## 6.5 Phase C: Detailed Definition

During Phase C, extensive RHA implementation occurs. This includes:

- **Radiation characterization tests:** TID tests using gamma or X-ray sources, DDD tests via proton or neutron beams and SEE testing using heavy ions or protons.
- **Shielding optimization:** sector-based modeling and full 3D simulations to minimize dose while managing mass constraints.
- **Worst-Case Analysis (WCA):** evaluation of system performance degradation under accumulated dose and transient upset conditions.

These activities culminate in Equipment CDRs, where detailed radiation analysis and test results are formally reviewed. The impact of SEE is assessed using the Failure Mode, Effects and Criticality Analysis (FMECA) methodology.

## 6.6 The NASA Programmatic Approach

NASA's approach to Radiation Hardness Assurance, [28],[29] and [53], emphasizes a structured, programmatic methodology tailored to support a wide array of spaceflight missions, especially those incorporating commercial off-the-shelf (COTS) and emerging technologies.

NASA's systems-level approach to RHA unfolds through a sequence of interrelated tasks:

- Define the hazard
- Evaluate the hazard

- Define requirements
- Evaluate device usage
- Engineer with designers
- Iterate the process

### **6.6.1 Defining the Radiation Hazard**

At the onset of a program, often during proposal development, a preliminary radiation environment is defined based on initial mission characteristics. These include orbital parameters, anticipated mission duration, scheduled launch date and assumptions on spacecraft shielding, typically expressed as an equivalent aluminum thickness.

The environment definition accounts for multiple radiation sources:

- Trapped electrons and protons (e.g., from the Van Allen belts),
- Galactic cosmic ray heavy ions,
- Solar energetic particles (protons and ions from solar flares and CMEs).

Specific outputs of this phase include:

- External particle fluxes for evaluating material degradation and surface charging,
- Internal particle levels behind nominal shielding to assess DDD and SEE risk,
- LET spectra of shielded environments for SEE calculations,
- Dose-depth curves to estimate TID using simplified geometric models.

To ensure robustness in SEE analysis, both nominal and peak radiation levels are defined (e.g. during South Atlantic anomaly transit or extreme solar events). As mission parameters evolve, radiation profiles must be revised. Even modest changes in orbit or launch timing can affect exposure due to variations in geomagnetic shielding and solar cycle intensity. Advanced models like CREME96 enable recalibration of environment definitions accordingly.

## **6.6.2 Evaluating the Hazard**

Once the radiation environment has been characterized, the next essential step is to assess its potential effects on the spacecraft's electronic systems. Key concerns include long-term degradation from TID, structural damage from Displacement Damage Dose (DDD) and transient disruptions caused by SEEs.

Using the top-level environment definition, engineers assess whether proposed components, particularly commercial or emerging technologies, can tolerate the expected radiation levels. For missions with high predicted doses, commercial-grade parts may not be suitable, especially for critical systems.

At this stage, aligning radiation analysis with system design decisions is essential to ensure that risks associated with radiation-sensitive technologies are identified early and mitigation strategies are realistically planned. This collaboration helps address issues such as:

- Emerging challenges with newer or radiation-sensitive technologies,
- The necessity for conservative design margins and part derating,
- Scheduling and planning for part-level radiation testing,
- The importance of updating radiation models when mission parameters change.

It's also essential to offer realistic mitigation strategies. A common misconception is that localized shielding, a spot shielding, can solve all radiation problems. In practice, this approach is often ineffective for SEEs and displacement damage due to protons. Failure to address these limitations early can result in costly rework and delays.

Performing a thorough evaluation at this point not only improves technical understanding but also ensures better-informed design decisions, ultimately enhancing the system's resilience and mission reliability.

## **6.6.3 Defining Mission Requirements from the Hazard**

Once the hazard is understood, the next task is to derive mission-specific radiation requirements. In the early design stages, when full geometry details may be unavailable, estimates typically assume a generic geometry, such as a solid aluminum sphere and nominal shielding thicknesses.

Radiation effects engineers must establish performance thresholds for key radiation-induced effects:

- **TID:** apply a Radiation Design Margin (RDM) of at least 2 to accommodate uncertainties in radiation modeling and inherent part variability. For low dose rate-sensitive technologies, ELDR, higher margins may be appropriate.

- **Displacement Damage:** requirements may be specified as total proton fluence above a certain energy threshold, for instance  $E > X$  MeV. Proton energy spectra must be weighted according to Non-Ionizing Energy Loss (NIEL) functions. For Silicon, results are often normalized to 1-MeV neutron equivalent fluences; for GaAs, 50 MeV protons are commonly used due to their representativeness and test availability.
- **SEE:** due to system variability, SEE requirements are tailored to mission-criticality. Event rate thresholds can be derived using GSFC guidelines or SEECA (Single Event Effect Criticality Analysis).

These requirements must account for both nominal and peak exposure conditions. For example, if scientific payloads must remain active during solar particle events, designs should tolerate peak flux environments; otherwise, safhold operation during such periods may be acceptable.

#### 6.6.4 Evaluating Device Usage

Determining the suitability of specific electronic components involves a structured, multi-step process:

##### 1. Parts List Screening

After compiling the list of candidate components, each item is checked against established radiation data repositories such as RADATA, ESARAD and GSFC databases. If relevant data are missing or the manufacturer does not guarantee compliance with mission-specific radiation levels, engineers must either initiate dedicated radiation testing or seek alternative devices with similar electrical characteristics.

Key rules for determining archival data usability include:

- Data are invalid if the foundry or manufacturing process has changed.
- A different lot date code (LDC) typically warrants new testing unless supported by detailed process similarity.
- Testing conducted at non-representative dose rates or lacking high-LET data may be inadequate.
- Devices that barely meet requirements may still need mitigation or further evaluation.



## 2. Radiation Testing

Devices are categorized into three risk levels:

- **High-risk:** devices with no known radiation data or a history of sensitivity, for example to latch-up or TID.
- **Medium-risk:** components with partial test data or similar devices on the same process showing manageable issues.
- **Low-risk:** well-characterized parts.

Radiation testing typically involves:

- Co-60 gamma irradiation for TID,
- Proton or neutron beams for DDD,
- Heavy ions or high-energy protons for SEE.

## 3. Performance Assessment

Once test data are available, their relevance to the spacecraft context must be analyzed. Examples include:

- Estimating SEE event rates,
- Evaluating degradation effects, such as reduced current transfer ratio (CTR) in optocouplers,
- Assessing the system-level impact of TID-induced parameter shifts.

A test result alone is insufficient without understanding how the part behaves within the full system. This emphasizes a shift from pure risk avoidance to informed risk management. In practice, it may be more effective to mitigate an SEE-prone device at the system level than to discard it entirely, especially when performance or availability constraints exist.

### 6.6.5 Engineering Collaboration and Design Iteration

After evaluating component suitability, radiation effects engineers work closely with spacecraft designers and systems engineers to ensure that the selected technologies meet mission-specific requirements. If a component does not meet the radiation tolerance criteria, the team searches for alternative parts that meet functional needs and exhibit acceptable risk profiles based on existing test data.

When such alternatives are unavailable, the focus shifts to mitigation strategies, which may include:

- Reassessing the radiation hazard using spacecraft-specific dose-depth analyses,
- Designing targeted shielding configurations for sensitive components,
- Relocating components within the spacecraft to take advantage of naturally shielded zones.

Advanced three-dimensional modeling tools based on sectoring and ray-tracing techniques allow engineers to simulate and estimate radiation doses and particle fluence behind the shielding. These models are refined in an iterative manner:

- Start with focused models around critical subsystems,
- Expand to include spacecraft structures and generic enclosures,
- Introduce fine-grain detail only where radiation margins remain insufficient.

Once deemed prohibitively expensive, this modeling approach has become increasingly practical due to the shrinking availability of rad-hard components. It enables a precise definition of local environments, supports data-driven mitigation planning and informs trade-offs between shielding mass and system protection.

Although such models are predominantly used for Total Ionizing Dose (TID) assessments, studies show that proton-induced Single Event Effects (SEE) can vary by a factor of two depending on component location. This is especially relevant for high-altitude or deep-space missions where the flux of very energetic particles is more intense and variable.

Because spacecraft designs are dynamic, RHA activities must be adaptable. Common changes that may trigger reevaluation include:

- Updates to the parts list,
- Modifications in mechanical layout,
- Altered mission duration or operational modes,
- Knowledge and discovery of failure mechanisms.

## **6.7 Risk Assessment in Radiation Hardness Assurance**

Radiation Hardness Assurance (RHA) revolves around the core concept of risk: its acceptability, quantification and mitigation. Effective risk management underpins all phases of the RHA, from the selection of components to the integration of the

final system, particularly in an era increasingly reliant on COTS and emerging technologies with uncertain radiation behavior.

Older devices such as discrete transistors offered gradual, predictable degradation under radiation. In contrast, modern integrated circuits consist of complex, proprietary internal structures that may respond unpredictably to radiation, introducing failure modes such as latch-up. Since internal design details are often undisclosed, engineers must rely on limited test data that may not fully capture the true behavior of a device.

### **Use and Limitations of Archival Data**

Archival data are an important resource for early screening. If existing data show strong performance margins, for example, survival at ten times expected dose, components may be accepted without further testing. However, this assumes that the data are applicable. In many cases, issues such as different fabrication processes, test conditions or omission of low-dose-rate and SEE effects can undermine relevance. Each factor must be carefully assessed.

To determine whether archival results are still valid, engineers should:

- Establish arbitrary time windows for applicability of older data (i.e., a fixed number of years),
- Assess data consistency across multiple historical samples,
- Compare current and older lots using photomicrographs or electrical profiling.

In some cases, data from one device are extrapolated to a similar one. Although total dose data may be extended within a product family, SEE data are much more layout sensitive. Extending results across manufacturers is particularly risky and generally discouraged.

### **Identifying Critical Components**

Not every component on a spacecraft must be built to survive the entire mission's radiation exposure. Some are only active during the early stages of the mission or others may play a minor role in mission success. Additionally, some systems include built-in redundancy or fallback operational modes that can tolerate isolated failures.

The real concern lies with components that are vital to mission operations and for which failure, especially one triggered by radiation, is either unmanageable or unpredictable. These mission-critical components must be identified early and treated with rigorous and careful study, as they carry both operational importance and elevated radiation risk.

## **Parts Control and Assurance Strategy**

Ideally, all components undergo robust test campaigns. In practice, constraints dictate a more pragmatic process:

- Check for radiation data,
- Verify manufacturing process compatibility,
- Ensure test methodology matches mission conditions,
- Apply margins of at least  $2\times$  (or higher for critical parts) and redundancy where direct assurance is lacking
- When dealing with newer technologies, especially those using highly scaled geometries, engineers should lean toward conservative assumptions and design safeguards, maintaining awareness of evolving technology risks and new radiation mechanisms.

High-risk devices such as microcontrollers, optocouplers and highly scaled nodes must be conservatively assessed. Marginal technologies, like those sensitive to latch-up, should be avoided unless robust mitigation is available.

## **6.8 Outlook and Transition to Radiation Effects Characterization**

As Radiation Hardness Assurance (RHA) evolves alongside advancements in micro-electronics and mission architectures, the focus must expand beyond mitigating existing risks to anticipating those posed by future technologies. The accelerated pace of space program development often limits the ability to thoroughly test and qualify new components prior to deployment. As such, forward-looking strategies must be embedded into the RHA methodology from the outset.

These strategies include early screening of emerging devices, proactive setup of dedicated test campaigns and collaborative partnerships with space agencies, academic institutions and industry stakeholders. Shared databases, coordinated testbeds and long-term technology monitoring will increasingly serve as critical tools in ensuring radiation assurance for next-generation missions.

This evolution, from a traditional risk avoidance posture to a dynamic, system-level risk management framework, necessitates a more profound understanding of the underlying physical mechanisms of radiation damage. To support this transition, the next chapters will explore the primary categories of radiation-induced effects in electronic systems:

- **Total Ionizing Dose (TID);**
- **Displacement Damage Dose (DDD);**
- **Single Event Effects (SEE).**

Each of these effects introduces distinct failure mechanisms and challenges. Understanding how they develop, how to simulate or measure their behavior and how to mitigate their consequences is essential for building resilient spacecraft systems. These foundational insights will guide designers in selecting appropriate technologies, tailoring radiation test plans and developing effective system-level safeguards.

# Chapter 7

## Total Ionizing Dose

### 7.1 Overview

Ionization induced in semiconductor material or associated insulators, such as silicon dioxide layers, can lead to charge trapping or the formation of interface states at the semiconductor–insulator boundary, affecting component behaviour or material properties. In MOS devices, the trapped charge can lead to a shift in the gate threshold voltage and for semiconductors in general, interface states can significantly increase device leakage currents. Materials such as polymers and glasses are also susceptible to Total Ionizing Dose (TID) effects and can suffer degradation in mechanical, electrical and optical properties.

The content of this chapter has been developed based primarily on two key technical references: the ESA handbook on radiation effects in electronics [2] and the Radiation Handbook published by Texas Instruments [6]. The ESA document was selected to ensure alignment with ECSS-compliant methodologies and space qualification practices, while the Texas Instruments handbook was chosen for its practical insights grounded in decades of experience in the design and testing of radiation-tolerant electronic components.

#### 7.1.1 Relevant Environment

TID effects shall be analysed for mission systems to be operated within any of the following radiation environments:

- Trapped proton and electron belts
- Solar protons
- Secondary particles such as bremsstrahlung from electrons

### **7.1.2 Technologies Sensitive to TID**

If one of the technologies identified in Table 7.1 is used, the potential TID level and effects shall be analysed.

**Table 7.1:** Technologies susceptible to TID effects

Technology Category	Sub Categories	Effects
MOS	NMOS, PMOS, CMOS, CMOS/SOS/SOI	Threshold voltage shift, decrease in drive current and switching speed, increased leakage current
BJT		hFE degradation, particularly for low-current conditions
JFET		Enhanced source-drain leakage current
Analogue microelectronics		Changes in offset voltage and offset current, changes in bias-current, gain degradation
Digital microelectronics		Enhanced transistor leakage, logic failure from: a) Reduced gain (BJT); b) Threshold voltage shift and reduced switching speeds (CMOS)
CCDs		Increased dark currents, effects on MOS transistor elements, some effects on CTE
APS		Changes to MOS-based circuitry of imager, including changes in pixel amplifier gain
MEMS		Shift in response due to the charge build-up in dielectric layers near to moving parts
Quartz resonant crystals		Frequency shift
Optical materials	Cover glasses, fibre optics, optical components, coatings, instruments, scintillators	Increased absorption, variation in absorption spectrum (coloration)
Polymeric surfaces		Mechanical degradation (radiolysis), changes to dielectric properties



### 7.1.3 Impacts on Technology

Bipolar devices experience more degradation at low dose rates (LDR), typical in space environments, compared to high dose rates (HDR). This phenomenon, known as ELDRS (enhanced low-dose rate susceptibility), does not usually affect MOSFETs.

HDR-only tests on ELDRS-prone devices underestimate TID sensitivity, leading to premature failures in space.

- At HDRs, higher carrier density enhances recombination, reducing trapped holes and released protons, which mitigates damage.
- At LDRs, lower recombination rates allow more trapped holes and protons to reach the oxide interface, increasing degradation.

Due to self-annealing effects, CMOS devices demonstrate greater TID tolerance at low dose rates compared to high dose rates.

For example, the Texas Instruments DAC121S101QML-SP space-grade precision digital-to-analog converter [6] fails below 30 krad(Si) at a high dose rate of over 50 rad(Si)/s but can endure doses exceeding 100 krad(Si) at a lower dose rate of 0.01 rad(Si)/s.

The bias voltage applied to a device during irradiation significantly affects CMOS sensitivity to ionizing radiation. Higher bias voltages result in greater charge buildup in the oxides.

Analog CMOS devices with wide operating voltage ranges typically withstand higher TID levels when operating at lower voltages during irradiation. For instance, the DAC121S101QML-SP [6] fails at TID levels below 30 krad(Si) when biased at 5.5 V during high-dose-rate irradiation, but can tolerate over 100 krad(Si) when biased at 3.3 V, regardless of dose rate.

For linear bipolar devices, irradiating the device in an unbiased state can represent the worst-case scenario, particularly at LDRs. For instance:

- A device may experience greater parameter shifts, such as voltage reference drift, when irradiated without power.
- Output voltages can behave differently depending on biasing conditions.

The operational state of a device during radiation exposure is therefore critical. Devices that are powered during irradiation can often withstand significantly higher TID levels compared to when they are in standby or unbiased conditions. This is why ELDRS testing includes scenarios where devices are irradiated while unpowered.

As feature sizes decrease, gate voltages in digital devices also reduce, resulting in lower supply voltages and improved TID survivability.

The TID survivability of classic bipolar analog products ranges from 1 to 100 krad(Si). TID performance can depend on the bipolar process, the function of the device, transistor layout and metal routing.

For example, adding a silicon nitride layer as a moisture barrier significantly improved product reliability but also degraded TID performance of many bipolar products.

#### **7.1.4 TID Requirements**

In the context of space missions, radiation can have significant long-term effects on electronic systems. One of the most critical concerns is the Total Ionizing Dose (TID), which refers to the cumulative energy deposited by ionizing particles over time. If left unaddressed, this effect can degrade the functionality of electronic components or lead to outright failure. To avoid such outcomes, a systematic assessment of TID sensitivity must be performed for all critical components. The evaluation presented in this section is based on the methodology defined in the ECSS standard [4] and its subsequent revision [30], which provide updated criteria and procedures for Total Ionizing Dose analysis in space systems.

Once the severity of the radiation environment is defined, typically during early project phases, a Mission Radiation Environment Specification is developed, in accordance with ECSS-E-ST-10-04 [3]. This specification serves as the baseline for evaluating component exposure and includes detailed TID level predictions (TIDL), obtained using validated tools such as 3D Monte Carlo simulations or ray-tracing models, as defined in ECSS-E-ST-10-12 [1]. TIDL reflects the total accumulated dose a component will experience, considering shielding, material properties and placement within the system.

To assess whether a given component is suitable for the mission, its TIDL must be compared with its Total Ionizing Dose Sensitivity (TIDS). TIDS is defined as the dose threshold beyond which a device can no longer satisfy its parametric or functional requirements. It is typically determined through a combination of manufacturer specifications and radiation testing data. In some cases, mission-specific criteria may be used to define the maximum tolerable parameter drift, ensuring compliance with system-level requirements throughout the equipment lifetime.

The test data used to determine TIDS must meet several conditions to be deemed acceptable:

- Tests must conform to ESCC 22900, MIL-STD-883 method 1019 or MIL-STD-750 method 1019;
- Devices containing bipolar transistors must be tested at dose rates below 360 rad/h;

- Tested devices must be manufactured using the same process, diffusion masks and wafer fabrication facilities as the flight parts;
- Bias conditions during the test must be equivalent to or more severe than those in the actual application.

Furthermore, component TIDS shall be calculated using a statistical approach based on the one-sided tolerance limit method as described in MIL-HDBK-814. This ensures a minimum probability of survival ( $P_s \geq 90\%$ ) with a confidence level of at least 90%.

The results of the radiation analysis thus yield both TIDL and TIDS. As a general rule, the desired condition is:

$$TIDL < TIDS$$

If this criterion is not satisfied, mitigation actions or additional testing are necessary. Table 7.2 presents the typical TID susceptibility thresholds for various EEE part families.

**Table 7.2:** EEE part families potentially sensitive to TID (adapted from ECSS-Q-ST-60-15C) [30]

EEE Part Family	Sub Family	TIDL (krad-Si eq)
Diodes	High accuracy (<1%) Zener (voltage reference)	If TIDL > 100
	Temp-compensated Zener (<2%)	If TIDL > 100
	Other Zener	If TIDL > 300
	Switching, rectifier, Schottky	If TIDL > 300
	Microwave	If TIDL > 300
Thyristors	All	All
Integrated Circuits	All	All
MMICs	GaAs, GaN	If TIDL > 300
	SiGe	If TIDL > 100
Oscillators (hybrids)	All	All
Image Sensors	CCD, CIS, others	All
Optoelectronics	Photodiodes, LEDs, Phototransistors, Optocouplers, Laser Diodes	All
PICs	All	All
Transistors	BJT, MOS (Si, SiC), Power	All
	GaN, IGBTs	
	GaAs, GaN HEMTs	If TIDL > 300
	SiGe HBTs	If TIDL > 100
Hybrids with Active Parts	All	All

Components are then categorized according to the following logic:

- **Group 1.** If  $\text{Maximum RDM} \times TIDL < TIDS$ , no additional action is required.
- **Group 2.** If  $\text{Minimum RDM} \times TIDL < TIDS < \text{Maximum RDM} \times TIDL$ , Radiation Verification Testing (RVT) must be performed.
- **Group 3.** If  $TIDS < \text{Minimum RDM} \times TIDL$ , the component is not acceptable for use in the application.

The Minimum Radiation Design Margin (MRDM) typically assumed for TID assessments is 1.2. This value addresses uncertainties related exclusively to EEE parts, including sample variation and test reproducibility. Uncertainties in the environmental model are covered separately in the mission environment specification.

If the flight model uses components from a different diffusion lot than those used in the original tests, Radiation Verification Testing must be performed under the following conditions:

- For all optoelectronic parts: every lot must be tested;
- For all other parts: testing is required if TID MAXimum RDM is less than 2.

Ultimately, the objective of TID assessment is to ensure long-term performance and reliability of electronic systems exposed to ionizing radiation. By establishing clear thresholds (TIDL and TIDS), applying robust analysis methodologies and enforcing verification testing where needed, mission designers can ensure that all hardware remains functional throughout the radiation design lifetime—even in the harshest orbital environments.

### 7.1.5 Material Selection and Shielding Configuration Strategies

When microelectronics must function in a space environment and where the mission dictates time and radiation environment, the only recourse to mitigate or reduce the exposure levels is to shield the electronics. The type of shielding depends on the type of radiation to be shielded and its energy. Shielding can help reduce the amount of radiation reaching the microelectronics and thus reduce the severity of radiation effects. Radiation-shielding properties of matter are based on the material's attenuation of the specific radiation of concern. Attenuation is a measure of the reduction in radiation intensity as a function of the thickness of the shielding material. Shielding materials are selected based on maximizing attenuation while minimizing the required mass of the shield (or its thickness). Additionally, shielding materials should not generate a high flux of secondary particles when exposed to environmental radiation [2] and [26]. Shielding reduces the incident flux of radiation on microelectronics and thus impacts both dose and SEEs.

The actual impact of shielding depends not only on the shield material and thickness, but also on the type and energy spectrum of the radiation being shielded against. As an example, electrons are shielded relatively easily by thin metal shields, while neutrons require meters of shield material to reduce their numbers. Space radiation extends to extremely high energies, so shielding is never completely effective [2].

Another severe constraint in spacecraft is the mass and size of the final payload or vehicle. Large, heavy shielding is often not a viable option due to mass/space constraints. In typical spacecraft applications, the shield material is usually aluminum, with thicknesses of 100–300 mils (2.5–7.6 mm). Aluminum shielding does attenuate low-energy ions and electrons, but has a minimal effect on high-energy radiation from galactic/solar cosmic rays [2] and [26].

Aluminum thicknesses in excess of 50 mils absorb the majority of incident electrons. However, increasing the shielding thickness beyond that renders diminishing returns. If we consider the TID curve as a function of aluminum shield thickness for three space radiation sources (electrons, protons and Bremsstrahlung radiation), it can be seen a saturation in the curve that means that adding additional shielding thickness is of limited effectiveness in further reducing TID. The saturation occurs because a large fraction of the incident proton radiation is of such high energy that several millimeters of aluminum are insufficient to significantly reduce their numbers [2].

Satellite microelectronics, subjected to the radiation environment, often must be radiation hardened to meet their performance requirements. The use of commercial, unhardened parts for satellite missions has several advantages over the use of radiation-hardened parts: lower cost, wider selection and state-of-the-art capability. However, the radiation hardness of commercial electronics parts is not well known. Part requirements, including design margins, are often introduced to bound the variability and significant radiation shielding may be required to protect these parts. Due to severe weight restrictions, however, it is important to avoid over-shielding [6].

The point is that the optimal shield design depends on both the intensity and the energy distribution of the radiation. Because of the complicated interplay of the various processes involved in electron/proton slowing down, it is not obvious which shield materials are the most effective for a given orbit [27].

For a preliminary analysis, it seems advantageous to design a layered shield for the protection against electrons, to take advantage of the large elastic scattering cross section of high-Z materials and the low bremsstrahlung emission from low-Z materials. A low-Z material (aluminum) effectively shields the primary electrons due to its relatively large stopping power for electrons. This outer aluminum may be the module skin itself. Next is a layer of high-Z material (tantalum), which effectively scatters electrons and absorbs the secondary bremsstrahlung photons. Finally, a thin layer of low-Z material is located between the high-Z material and the microelectronics to suppress photo-electron emission [2] and [26].

The multilayer configuration leverages the combined advantages of these materials: tantalum provides a high cross-section for elastic scattering (reducing electron penetration), while aluminum minimizes bremsstrahlung emission and the effect of secondary electrons. This synergy maximizes the overall shielding efficiency.

In contrast, the lower-Z materials are more effective proton shields. A low-Z material such as polypropylene or polyethylene. For protons, instead, the stopping power is higher in low-Z shields: the main mechanism of energy dissipation for protons and heavy ions are inelastic collisions with atomic electrons. Being heavier particles, these are not subjected to the range of scattering experienced by electrons, in fact due to the smaller scattering the low-Z materials provide more mass-efficient

shields. In addition to interaction with electrons, there is however a small, but not negligible, chance of protons or other ions interacting with atomic nuclei, causing excitation and fragmentation of the nucleus or the emission of secondary neutrons, protons, alpha particles and other light nuclear fragments, as well as gamma rays. The fragments and secondaries produced are hazards for applications sensitive to single event effect process. In addition to being more efficient at slowing down ions through ionization, low-Z materials produce fewer secondary products [25].

TID effects in semiconductor devices depend on the creation of electron-hole pairs within dielectric layers, by the incident radiation and subsequent generation of:

- Traps at or near the interface with the semiconductor
- Trapped charge in the dielectric

This can produce a variety of device effects such as flatband and threshold voltage shifts, surface leakage currents and noise.

For dose behind a shield, the increased scattering in high-Z materials reduces the dose more for thin high-Z shields than for thin low-Z shields. For thicker shields the bremsstrahlung becomes important and low-Z shielding is more efficient than high-Z. An optimum shield employs a low-Z layer followed by a high-Z layer, so such graded shield against electrons can give weight or dose advantages [27].

It is important to realise that simply adding more shielding does not always lead to reduced dose at the sensitive target. There are cases where this can lead to more secondary particles or to undesirable changes in the incident particle energy spectrum, hence actually enhancing the dose. In particular, the high-energy cosmic rays are difficult to shield against and nuclear interactions in the shield give rise to a significant multiplicity of secondary particles, the lower-energy charged particles producing more ionisation than the original cosmic rays. Additionally, dose enhancement can be seen at boundaries between high-Z and low-Z materials [2].

The point is to ensure that the dose is tolerable, in particular with COTS, where it is necessary providing radiation tolerance of specific parts at the level required for the mission to improve reliability. Most commercial components, according to [34], are radiation tolerant to 5 krad. Many are radiation tolerant to 20 krad or more. Some will fail before 1 krad. Without testing it is impossible to predict which category a part will fail into. At this stage of analysis, the design practice to use “built-in” shielding is not considered such that the need for add-on shielding is maximized [6].

The first solution can be to add some “add-on”, in terms of layers of specific material.

Tools such as **MULASSIS**, [31] and [32], can be employed to determine shielding characteristics for any shield material to assess the capability of a certain thickness

of material to absorb energy of the incident flux of particles. Simulations were performed to obtain numerical values and compare the different shielding capabilities of materials under specific conditions.

The orbit under consideration was at 3000 km altitude and protons were used as the source of radiation. Three materials were analyzed: aluminum, polyethylene and polypropylene. For each material, two different thicknesses, 5 mm and 10 mm, were evaluated under the assumption of a spherical geometry.

The outputs of the simulations included the energy deposition and pulse height distribution within a defined layer of the shield. These metrics were used to compare the performance of the materials in terms of their ability to mitigate proton-induced energy deposition and provide insight into the relative effectiveness of each material and thickness in the given radiation environment.

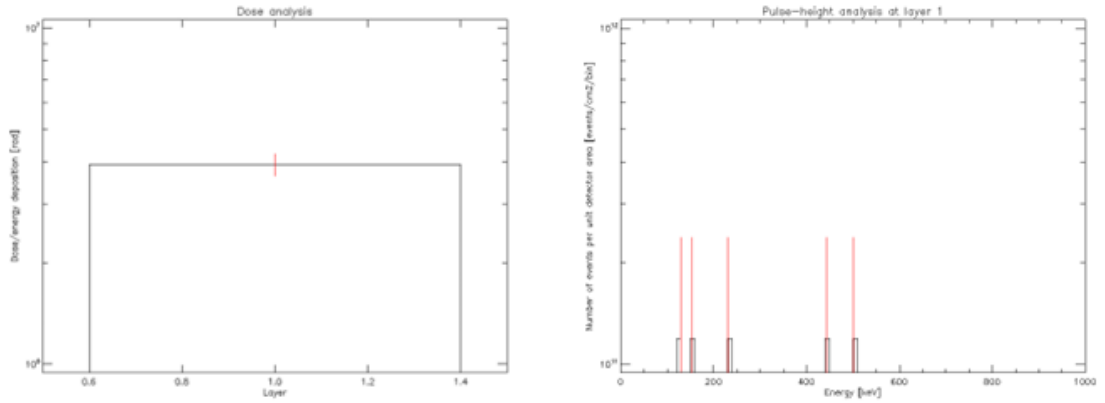


**Figure 7.1:** Energy deposition and pulse-height analysis for 5 mm layer of Aluminum

The outcomes presented in the figures are consolidated and reported in Table 7.3 for comparison in terms of dose accumulated in the specific layer under exam.

**Table 7.3:** Energy deposition values under proton radiation at 3000 km altitude

Thickness	Aluminum [rad]	Polyethylene [rad]	Polypropylene [rad]
5 mm	$3.9 \times 10^6$	$9.2 \times 10^6$	$9.9 \times 10^6$
10 mm	$1.9 \times 10^6$	$5.8 \times 10^6$	$5.8 \times 10^6$

Based on the interpretation of energy deposition as the energy absorbed within the shielding layer itself, the analysis of the results can be reformulated as follows:

- Aluminum exhibits significantly lower energy deposition compared to polyethylene and polypropylene for both 5 mm and 10 mm thicknesses. This indicates



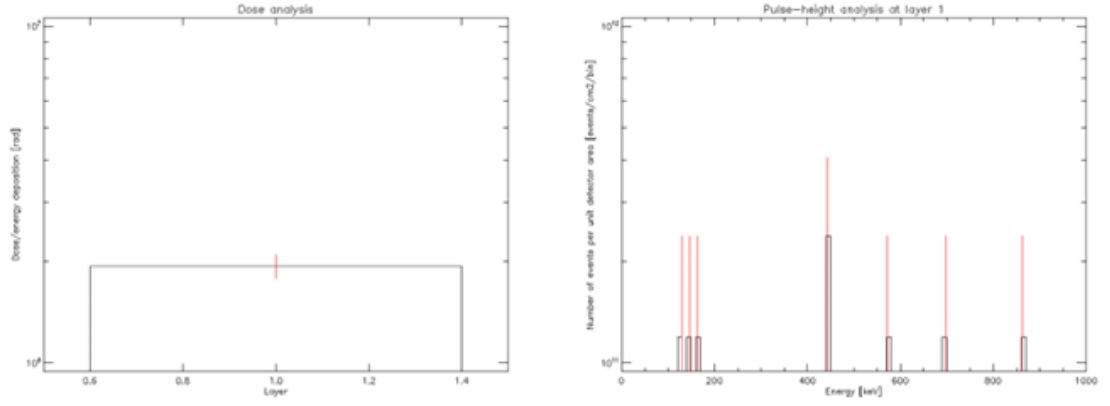


**Figure 7.2:** Energy deposition and pulse-height analysis for 10 mm layer of Aluminum

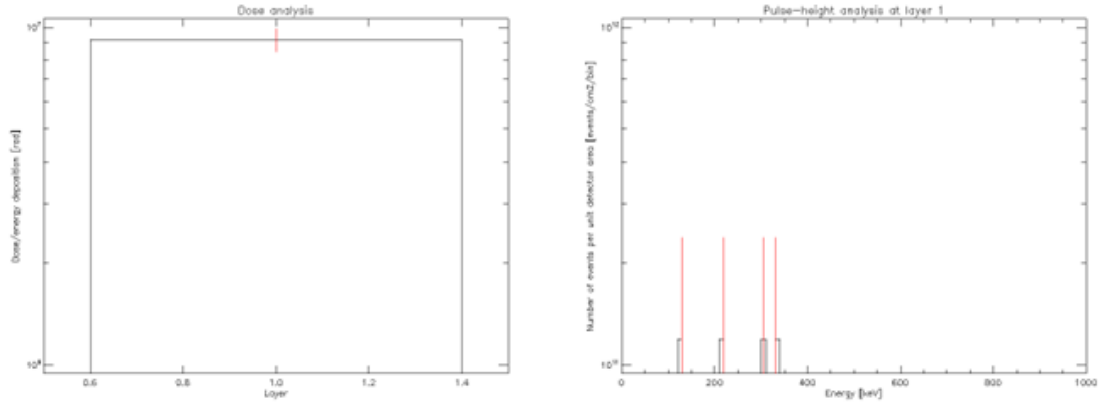


**Figure 7.3:** Energy deposition and pulse-height analysis for 5 mm layer of Polyethylene

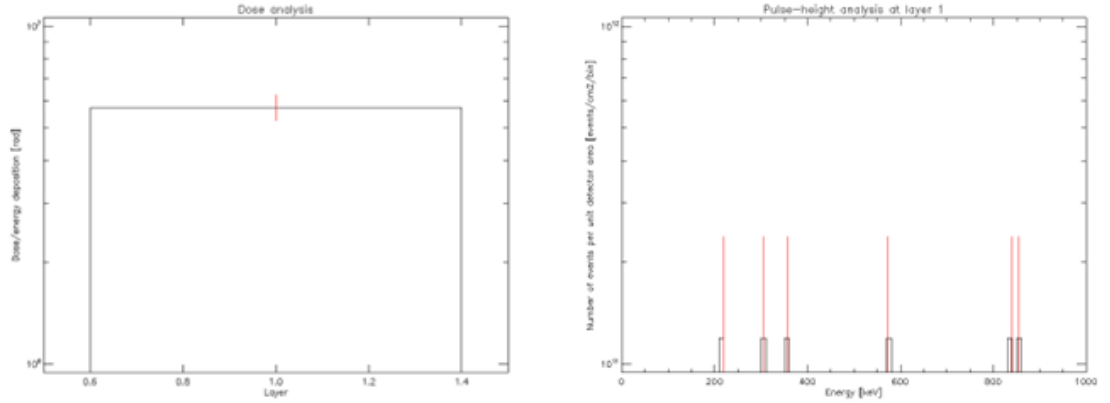


**Figure 7.4:** Energy deposition and pulse-height analysis for 10 mm layer of Polyethylene

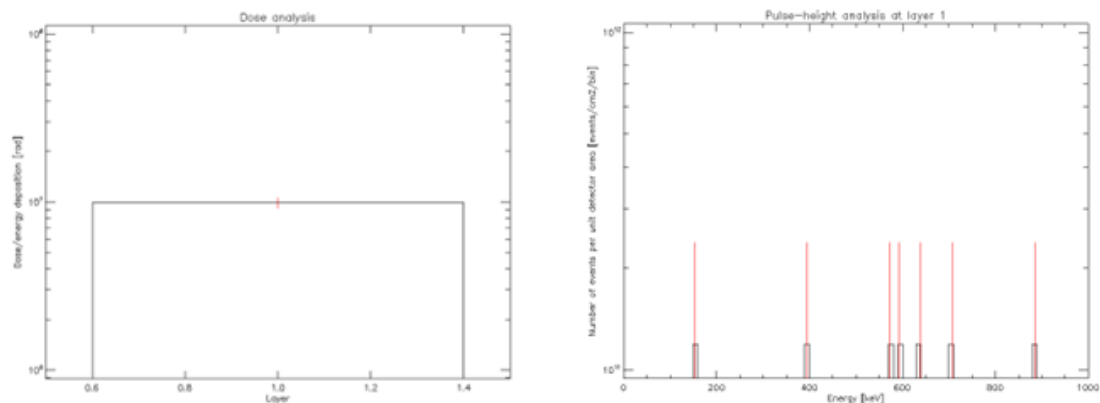


**Figure 7.5:** Energy deposition and pulse-height analysis for 5 mm layer of Polypropylene

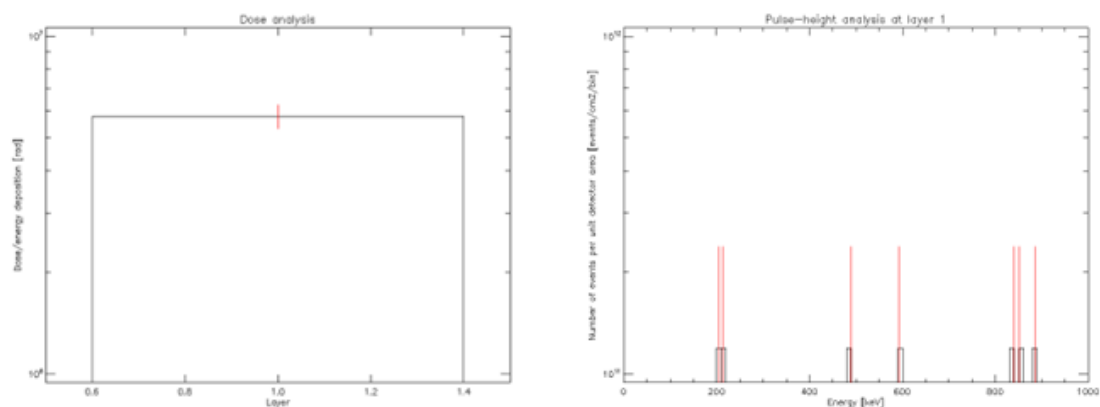


**Figure 7.6:** Energy deposition and pulse-height analysis for 10 mm layer of Polypropylene

that aluminum absorbs less of the incident proton energy within the shielding material itself, likely due to its higher density.

- Polyethylene and polypropylene show much higher energy deposition values at both thicknesses. This suggests that these hydrogen-rich materials absorb a greater proportion of the proton energy.
- Increasing the shielding thickness from 5 mm to 10 mm results in a notable reduction in energy deposition for all materials. For aluminum, the reduction is approximately 51%; for polyethylene and polypropylene, the reduction is around 37%.

Polyethylene and polypropylene, while showing higher energy deposition, tend to be more efficient materials in this scenario, so their choice may still be advantageous in environments dominated by high concentrations of protons.

### **7.1.6 Radiation-Hardened and Radiation-Tolerant Component Options: The Case of Texas Instruments**

Following the analysis of shielding techniques to reduce the Total Ionizing Dose (TID) in space environments, the next consideration in radiation mitigation involves the selection of electronic components based on their inherent resistance to radiation. Among the various industry suppliers, Texas Instruments (TI), [33], offers a robust portfolio of devices targeted for space applications.

TI has a long-standing history in this domain, providing semiconductor devices for space missions since 1958. Its portfolio includes both radiation-hardened (rad-hard) space-grade components and radiation-tolerant components. While both categories are intended for operation in harsh environments, they differ in terms of radiation resilience, testing standards and cost.

In addition to TI's comprehensive line of rad-hard QML-V products, suitable for normal and high-risk missions, the company has developed the Space Enhanced Plastic (Space EP) product family. These devices, delivered in plastic encapsulated microcircuit (PEM) packaging, are derived from commercial off-the-shelf (COTS) components and enhanced to meet space reliability needs, as described in [35], [36] and [37].

Space EP devices address the growing demand for cost-effective, lightweight and compact alternatives to ceramic-packaged space-qualified parts. Key features of the Space EP line include:

- **Process Control.** Manufactured with tighter tolerances and monitoring than standard COTS components.

- **Enhanced Qualification.** Subjected to rigorous testing protocols beyond commercial standards.
- **Extended Reliability.** Improved tolerance to thermal and radiation-induced stresses.
- **Intermediate Positioning.** Designed to fill the gap between standard COTS and fully rad-hard devices.

Plastic packaging, while not hermetic, enables reduced volume and mass, which is particularly beneficial for NewSpace missions. To further improve robustness, TI incorporates gold bond wires (avoiding copper-related failure mechanisms) and reduces tin content to mitigate the formation of tin whiskers.

The introduction of Space EP products enables a hybrid strategy: rad-hard components may be selected for critical functions in severe radiation environments, while radiation-tolerant parts, validated through process control and testing, can be used in less exposed areas of the spacecraft.

In the following section, a comparison of TID ratings for TI's space-grade components is presented. Devices with the suffix **-SP** indicate radiation-hardened QML-V components, while **-SEP** denotes the Space Enhanced Plastic product family. This classification assists in selecting components based on mission radiation profile, duration and criticality of function.

**Table 7.4:** TID ratings for selected TI space components [35]

Family	Product	Part Number	Rad-Hard	Rad-Tolerant
Power Mgmt	DC/DC Conv.	TPS7H4001-SP, TPS7H4003-SEP	100 krad	50 krad
	PWM Ctrl	TPS7H5001-SP, TPS7H5005-SEP	100 krad	50 krad
Interface	Transceiver	SN55HVD2331- SP/-SEP	50 krad	30 krad
	Gigabit PHY	DP83561-SP	300 krad	n.a.
Converters	LVDS	DS90C031QML-SP	100 krad	n.a.
	24-bit ADC	ADS1278-SP	75 krad	n.a.
	18-bit ADC	ADC3683-SP/- SEP	300 krad	30 krad
Amplifiers	GBW 850 MHz	LMH5485-SP/- SEP	100 krad	30 krad
Clocks	PLL Synth.	LMX2615-SP, LMX2694-SEP	100 krad	30 krad
Microcontrollers	Ultra-LP MCU	MSP430FR5969- SP	75/50 krad	n.a.
	ARM Cortex MCU	TMS570LC4357- SEP	n.a.	30 krad

It is important to underline that in Table 7.4, “not available” refers to cases where sufficient information could not be found in the reference datasheets.

In general, the Space Enhanced Plastic (Space EP) line is designed for emerging NewSpace and LEO commercial missions. These products offer a cost-effective, radiation-tolerant solution for shorter-duration and high-volume space applications, while maintaining the following technical advantages:

- **ELDRS-free operation:** rated to 30–50 krad(Si), with each bipolar and BiCMOS device characterized at low dose rate (10 mrad(Si)/s) [37].
- **Radiation Lot Acceptance Testing (RLAT):** all wafer lots are tested and qualified to 20 krad(Si), with test reports available. Devices rated at higher TID levels typically conform to the same RLAT standard [37].

As an alternative to space-grade components, a method referred to as *Careful COTS* [34] has gained traction. This strategy involves:

- Validating the radiation tolerance of commercial parts through targeted testing;
- Implementing rigorous screening and control processes to enhance component reliability;
- Leveraging radiation test databases to assess part behaviour under TID exposure.

Resources such as the NASA GSFC Radiation Database [38], ESA ESCIES [39], CERN Radiation Test Database [40] and DOEET [41] are invaluable for evaluating and qualifying COTS parts for flight. These tools also highlight the importance of application-specific testing, as components are often used in novel ways that require detailed validation to meet mission requirements.

### 7.1.7 Assessment of Shielding Strategies and Component Survivability

Building on the definition of radiation-tolerant component classes, it is essential to consider how the expected Total Ionizing Dose (TID) in orbit affects the selection and screening of such technologies.

The evaluation of TID in space radiation environments is essential for the selection of Electronic, Electrical and Electromechanical (EEE) parts in space missions. Based on the radiation environment analysis, it was determined that in the presence of aluminum shielding, the dominant contribution to TID originates from the incident proton flux. To mitigate TID effects, the objective is to absorb as much energy as possible within the shielding material, thereby reducing the energy deposited via ionization in semiconductors or insulating materials.

For a conservative assessment, we assume that the device lacks intrinsic protective measures and that its sensitive region is located immediately after the shielding layer. The selection criterion for TID sensitivity must therefore account for shielding effectiveness and material properties. Using MULASSIS simulations, we determined that by employing lightweight hydrogen-rich materials such as polypropylene, the energy absorption efficiency of aluminum is reduced by 67.24% for a 10 mm thickness compared to polypropylene.

The calculated TID values obtained via SPENVIS for different orbits assuming 10 mm of aluminum shielding are:

- LEO Max Envelope:  $4.55 \times 10^3$  rad
- 3000 km Altitude:  $5.32 \times 10^5$  rad
- 17000 km Altitude:  $1.37 \times 10^4$  rad
- GEO:  $5.13 \times 10^3$  rad
- Molniya:  $1.58 \times 10^4$  rad
- Synthetic Orbit:  $5.32 \times 10^5$  rad

To obtain a more detailed and statistically reliable assessment of the TID reduction strategy, a refined simulation was conducted with 10,000 primary incident protons at 3000 km altitude, where proton radiation is dominant. The shielding configuration implemented in the model was as follows:

- A 10 mm outer layer of Polypropylene, selected for its hydrogen-rich composition that enhances proton energy absorption.
- A 150 mm Silicon target layer, representing the sensitive electronics, to collect sufficient statistical data within a spherical geometry configuration. This choice was based on recommendations and discussions found in the official SPENVIS user forum, where such parameters are commonly adopted for conservative and representative shielding evaluations.

The simulation yielded the following energy deposition results, as illustrated in Figure 7.7:

- Polypropylene layer:  $2.29 \times 10^6$  rad (error:  $2.04 \times 10^4$  rad)
- Silicon target layer:  $1.18 \times 10^5$  rad (error:  $5.31 \times 10^3$  rad)

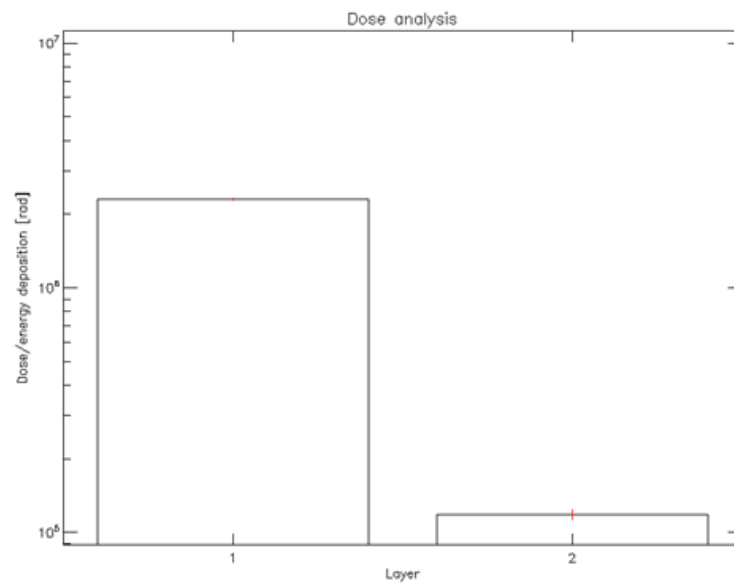


**Figure 7.7:** MULASSIS - Results for 10 mm Polyethylene layer + 150 mm Silicon layer in a spherical geometry

Compared to the TID for 10 mm of aluminum shielding previously evaluated, the addition of the polypropylene layer resulted in an approximate TID reduction of 78%. This highlights the significance of shielding material selection and confirms the viability of polymeric shielding for extending the operational envelope of standard or radiation-tolerant components in space missions. This reduction in TID demonstrates the effectiveness of hydrogen-rich materials like polypropylene in mitigating proton-induced ionization damage. Given this attenuation factor, the selection of radiation-tolerant EEE parts should consider this reduced TID when assessing component survivability.

Applying the 80% TID reduction factor due to the implementation of polymeric shielding, we observe a significant expansion of the operational envelope for electronic components. This level of mitigation allows for extended operations even within the central region of the inner radiation belt, where radiation levels are typically prohibitive for standard electronics. Nominally, the mission is planned for five years in LEO, but with this enhanced shielding capability, it becomes feasible to consider capture operations even within the central regions of the Van Allen belts. In this scenario, radiation-tolerant standard components could be utilized instead of fully rad-hard parts, provided they are effectively shielded. However, to ensure long-term reliability, it is essential to continuously monitor these components and impose constraints on their remaining operational lifetime under these more degrading conditions.

Since proton shielding requires hydrogen-rich materials, while electron shielding is efficiently handled by aluminum, the approach should include a hybrid shielding structure. Specifically:

- A polymeric matrix layer for proton attenuation.
- An aluminum skin of TBD mm to shield against electron radiation.
- Additional layers of high-Z materials (such as tungsten or tantalum) to further reduce TID.

This analysis provides a structured method for preliminary selection of EEE parts based on TID sensitivity. By incorporating hydrogen-rich shielding materials, a significant reduction in TID exposure is achievable, influencing component selection criteria. Rad-hard components remain the most reliable option for high-radiation orbits, especially at the centre of the inner belt (about 3000 km altitude), while rad-tolerant parts can be viable alternatives for the other studied scenarios. Future efforts should focus on reducing the required shielding thickness and further optimization of shielding materials, by:

- Implementing a hybrid shielding strategy that optimizes proton and electron attenuation by combining hydrogen-rich polymers, aluminum and high-Z materials.



- Cross-referencing TID qualification levels of Rad-Hard, Rad-Tolerant SEP and COTS components with the mission-specific shielding conditions.
- Selecting the most suitable components by ensuring that the characteristic TID of the chosen EEE parts exceeds the expected TID under optimized shielding conditions.

However, as the analysis extends to high-radiation environments such as the synthetic orbit, it becomes evident that maintaining system compatibility with COTS components presents significant challenges. In such worst-case scenarios, the accumulated TID can exceed 300 krad(Si), a value at which only radiation-hardened components remain reliably operational. This imposes a stringent requirement on the design of the ARCap module, as achieving TID resilience in this context would demand either:

- A highly specialized and mass-intensive shielding strategy, potentially exceeding 25–30 mm of aluminum equivalent or
- A complete migration to radiation-hardened parts, with substantial impact on cost, supply chain flexibility and design freedom.

Given that the ARCap system is currently in Phase 0/A, the priority is to define a conceptual architecture that enables a path toward Engineering Model (EM) validation using standard components (e.g., COTS or rad-tolerant SEP devices). This goal should be achieved without major alterations to the mechanical or functional design during later phases.

To that end, defining a radiation requirement that balances mission assurance and design feasibility is crucial. An imposed upper limit of 300 krad(Si) for the 5-year mission was initially adopted to screen and exclude overly sensitive sensors. However, this threshold remains too high for most COTS components, limiting their qualification without extensive shielding or full RHA campaigns.

A revised approach proposes reducing the system-level TID requirement to 50 krad(Si). This value offers several advantages:

- It enables the use of more accessible COTS components.
- It still ensures compatibility with a wide range of orbital environments if exposure is properly time-constrained.
- It reduces the need for excessive shielding and associated mass penalties.

This redefinition aligns with the CONOPS: ARCap remains dormant in LEO for most of the mission and is only exposed to elevated radiation levels during brief proximity operations. Therefore, the radiation requirement can be decoupled from

the absolute worst-case dose scenario and instead be interpreted as a controlled, integrated dose over time.

**Mitigation Strategy Summary:**

1. **Constrain exposure time** in synthetic orbits to minimize cumulative TID.
2. **Adopt a hybrid shielding approach:** aluminum skin + hydrogen-rich polymeric layer.
3. **Tailor the RDM** based on shielding model uncertainties.
4. **Qualify selected COTS via ground testing** up to 50 krad(Si).
5. **Maintain mechanical and electrical continuity** between EM and flight models.

In summary, while the synthetic orbit imposes severe radiation constraints, careful operational planning and shielding design allow the use of standard parts under controlled exposure conditions. The revised 50 krad(Si) requirement supports the development of a cost-effective, flexible ARCap architecture capable of operating across multiple orbital regimes.

### 7.1.8 Advanced Modelling of Shielding for the Synthetic Orbit

However, since the synthetic orbit represents the most critical scenario for AR-Cap's survivability, a more detailed radiation transport analysis was performed to better assess and refine the shielding requirements, especially considering realistic geometric constraints and material models.

This additional MULASSIS simulation focused on the 3000 km equatorial orbit, evaluating radiation dose deposition over a 5-year period. The sensitive volume was modeled as a 10 micron spherical silicon shell surrounding an inner vacuum sphere whose radius is set to 10% of the outer radius, to reflect a more realistic distribution of sensitive electronics. In order to achieve a statistically robust characterization of particle-matter interactions, the simulation was initially performed using a 150 mm-thick silicon layer. This configuration ensured that the full range of physical interactions, such as ionization, scattering and nuclear reactions, could be sampled with high statistical significance, regardless of the particle energy or type. This step allowed for the accurate validation of interaction models and energy deposition profiles across the entire spectrum of events relevant to the mission environment.

Once the physical processes were well understood and validated under these extended conditions, the model was refined by reducing the silicon thickness to 10  $\mu\text{m}$ , corresponding to a more realistic sensitive volume in advanced microelectronic

devices. This thinner geometry reflects the actual dimensions of the charge collection region, where the interest lies in energy deposited within a limited volume capable of triggering a circuit-level response. A first simulation was performed with 20 mm of aluminum shielding. Figure 7.8 shows the configuration used to define the simulation environment and results are summarized in Table 7.5.

Layer number	Material	Thickness (unit)	Visualisation colour
Layer 1	G4_Al	20 mm	yellow
Layer 2	G4_Si	10E-6 m	white
Layer 3	Vacuum	2 mm	white

**Figure 7.8:** MULASSIS - Configuration of particle environment and geometry


**Table 7.5:** Dose deposition in silicon for 20 mm aluminum shielding (3000 km orbit)

Layer	Thickness	Density (g/cm <sup>3</sup> )	Dose (rad)	Error (rad)
1	2.0 cm	2.699	$1.18 \times 10^6$	$3.15 \times 10^4$
2	10 $\mu$ m	2.33	$3.13 \times 10^5$	$7.06 \times 10^4$

Two additional configurations were tested using a hybrid shield composed of 10 mm of aluminum followed by either 5 mm or 3 mm of polypropylene (PP), combined with the same internal silicon shell and maintaining the same particle environment and modeling. These hybrid configurations aimed to assess the benefit of using hydrogen-rich materials for improved dose reduction and mass savings. Configuration of geometry and dose results are shown in Figure 7.9 and Table 7.7 and 7.6.

**Table 7.6:** Dose results for 10 mm aluminum + 5 mm polypropylene configuration

Layer	Thickness	Density (g/cm <sup>3</sup> )	Dose (rad)	Error (rad)
1	1.0 cm	2.699	$1.55 \times 10^6$	$4.48 \times 10^4$
2	0.5 cm	0.9	$5.46 \times 10^5$	$9.52 \times 10^3$
3	10 $\mu$ m	2.33	$2.97 \times 10^5$	$3.93 \times 10^4$

Geometry: User defined ▾			
Shape: sphere ▾		Number of layers: 4 ▾	
Layer number	Material 	Thickness (unit)	Visualisation colour
Layer 1	G4_Al ▾	10 mm ▾	yellow ▾
Layer 2	G4_POLYPROPYLENE ▾	5 mm ▾	white ▾
Layer 3	G4_Si ▾	10E-6 m ▾	white ▾
Layer 4	Vacuum ▾	1.5 mm ▾	white ▾
Visualisation			
Format: Virtual Reality Modelling Language (VRML) ▾			
Particle tracks: Do not display ▾			

**Figure 7.9:** MULASSIS - Shielding geometry with a hybrid configuration

**Table 7.7:** Dose results for 10 mm aluminum + 3 mm polypropylene configuration

Layer	Thickness	Density (g/cm <sup>3</sup> )	Dose (rad)	Error (rad)
1	1.0 cm	2.699	$1.75 \times 10^6$	$5.21 \times 10^4$
2	0.3 cm	0.9	$5.58 \times 10^5$	$1.29 \times 10^4$
3	10 $\mu\text{m}$	2.33	$2.74 \times 10^5$	$2.94 \times 10^4$

**Comparative Evaluation:**

The simulation demonstrates that adding a polymeric layer, even with a reduced aluminum thickness, provides substantial advantages in terms of dose reduction and shielding mass. Key findings include:

- The 10 mm Al + 5 mm PP configuration reduced the absorbed silicon dose by 4.8% compared to the 20 mm Al configuration.
- The 10 mm Al + 3 mm PP configuration yielded a 12.4% reduction.
- Both configurations resulted in significant mass savings due to the low density of polypropylene, with the 3 mm PP case offering up to 45% less total shielding mass.

These results confirm the effectiveness of integrating polymeric materials into multilayer shielding strategies, especially for short exposure durations in high-radiation orbits. They also support the selection of a shielding baseline that prioritizes mass efficiency without compromising dose resilience, critical for the constrained envelope and architecture of the ARCap module.

### 7.1.9 Conclusion: Defining a Feasible TID Requirement for the Synthetic Orbit

The overall objective of this study has been to evaluate the feasibility of operating the ARCap module in high-radiation environments, particularly the synthetic orbit, while minimizing the reliance on fully radiation-hardened components and maintaining a viable development path from conceptual design to flight.

Throughout the analysis, two Total Ionizing Dose (TID) thresholds have been considered:

- A **300 krad(Si)** threshold, reflecting a conservative upper bound tolerable by certain rad-tolerant components. This threshold, while feasible with heavy shielding, would severely restrict the use of standard electronics and impose substantial cost, qualification and mass penalties.

- A **50 krad(Si)** target, proposed not as a direct match for COTS capability, but as a realistic design goal that could be met through a combination of shielding, mitigation strategies and careful component selection or qualification.

COTS components are typically limited to below 20 krad(Si) and using them in the synthetic orbit is unrealistic without additional qualification or mitigation. However, by screening components, referencing radiation test databases (such as NASA GSFC, ESA ESCIES and DOEEET) and identifying rad-tolerant alternatives, it may be possible to qualify a subset of devices to withstand up to 50 krad(Si) with acceptable confidence.

Supporting this, simulations with MULASSIS demonstrated that multilayer shielding (e.g., aluminum and polypropylene) can significantly reduce dose and mass. For example:

- A 10 mm Al + 3–5 mm PP configuration yielded a 4.8–12.4% dose reduction in silicon compared to 20 mm Al alone.
- The same configurations reduced total shielding mass by up to 45%.

These results confirm the feasibility of targeting 50 krad(Si) as a qualified system-level dose, achievable by:

- Limiting exposure time in high-radiation orbits.
- Implementing hybrid shielding.
- Selecting components with proven tolerance in the 30–50 krad range.
- Applying conservative Radiation Design Margins (RDM).

In conclusion, a 50 krad(Si) requirement provides a technically grounded, cost-aware compromise. It is not inherently compatible with most COTS devices but becomes viable through targeted qualification and smart shielding design. This enables ARCap to operate robustly across multiple orbital environments while maintaining alignment with the project’s conceptual and budgetary constraints.

## Chapter 8

# Displacement Damage

This section provides an overview of displacement damage (DD), also referred to as non-ionizing energy loss (NIEL) and highlights the types of technologies and electronic components that are particularly vulnerable to this effect. Displacement damage is a cumulative phenomenon that arises when high-energy particles, such as protons, electrons, neutrons or heavy ions, interact with a crystalline material and physically knock atoms out of their original lattice positions.

The content of this chapter is primarily informed by two foundational references: the ESA handbook on radiation effects [2], which formally defines the DDD concept within the ECSS framework and the Texas Instruments Radiation Handbook [6], which provides an application-oriented perspective on how displacement damage impacts electronic components. Additionally, references [42], [43] and [44] serve as the theoretical and computational basis for the physical modeling of displacement damage phenomena. These works underpin the NIEL formalism adopted in tools such as SPENVIS and OMERE and are essential for interpreting the quantitative outputs derived from those platforms.

When such a collision occurs, it creates what are known as *point defects* in the material's structure: *vacancies*, where atoms have been removed and *interstitials*, where displaced atoms occupy normally unoccupied positions in the lattice, as shown in Figure 8.1. These defects are not static; they can migrate through the material, combine to form complex clusters or interact with impurities, resulting in the formation of stable defect centers.

In semiconductor devices, especially bipolar technologies, optoelectronic components and solar cells, the primary consequence of DD is a reduction in the minority carrier lifetime, which directly impacts device efficiency and performance. In crystalline optical materials, displacement damage can also cause increased light absorption and noticeable discoloration.

The atom initially displaced is referred to as the *Primary Knock-on Atom* (PKA). If the transferred kinetic energy exceeds a material-specific threshold, the

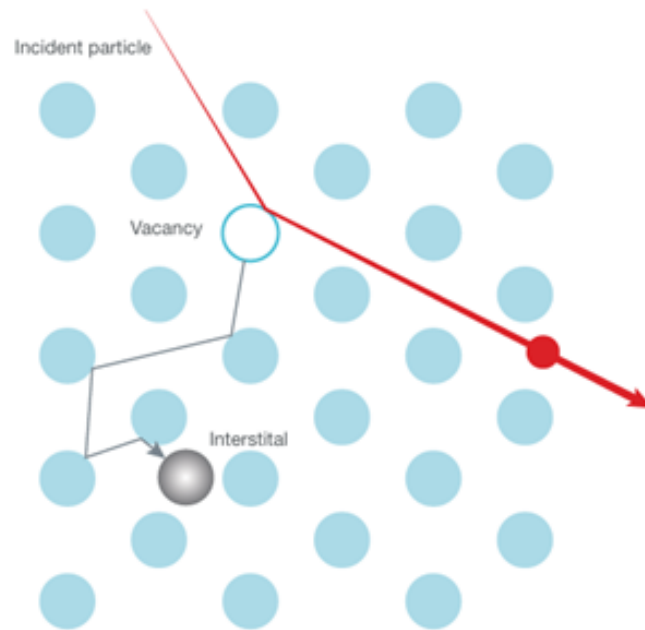


**Figure 8.1:** Schematic illustration of a vacancy (light gray) and an interstitial atom (dark gray) formed in a silicon lattice after an energetic particle strike [6].

PKA may itself go on to displace additional atoms, initiating a cascade of atomic displacements. The end result is a network of defects that alter the physical and electrical properties of the material over time.

Displacement damage is commonly quantified in terms of the degradation in component performance as a function of particle fluence and spectrum — for example, given in units of protons/cm<sup>2</sup> or electrons/cm<sup>2</sup>. It is fundamentally distinct from ionizing radiation effects, as the damage here is mechanical in nature rather than electrical. Nonetheless, both mechanisms contribute to long-term degradation in spaceborne electronics and must be carefully evaluated when designing systems for operation in radiation-rich environments.

### 8.0.1 Relevant Environment

Displacement damage effects must be carefully evaluated for systems operating in space environments where significant exposure to energetic particles occurs. The following sources are typically considered relevant for this type of non-ionizing damage:

- Trapped protons in the Earth’s radiation belts
- Solar energetic protons (SEPs)



- Trapped electrons
- Secondary protons and neutrons produced by particle interactions within the spacecraft or shielding materials

In contrast, displacement damage caused by primary and secondary galactic cosmic rays (GCRs) is generally excluded from standard microelectronics analysis, unless explicitly requested by the end user or customer. Although heavy ions present in the GCR flux are indeed capable of inducing displacement effects due to their higher non-ionizing energy loss (NIEL), their fluence is extremely low. As a result, their contribution to total non-ionizing dose (TNID) is typically negligible in practical mission scenarios.

It should be noted, however, that even high-energy photons, such as gamma rays or X-rays in the MeV range, may indirectly contribute to displacement damage. This occurs when such photons generate secondary electrons with enough kinetic energy to displace atoms from their lattice positions.

To clarify terminology:

- The **NIEL dose** refers to the total energy deposited in a material due to displacement effects, normalized per unit mass.
- The **NIEL** (or NIEL rate/coefficient) characterizes the energy lost by an incident particle per unit distance traveled in the target material, specifically due to atomic displacements.

The total displacement damage energy deposited per unit mass is obtained by multiplying the NIEL coefficient by the particle fluence (i.e., the time-integrated particle flux). In this sense, NIEL serves an analogous role to stopping power in ionization processes, just as stopping power determines the Total Ionizing Dose (TID), NIEL defines the cumulative displacement damage.

## 8.0.2 Technologies Susceptible to Displacement Damage

When evaluating the impact of displacement damage dose (DDD) on spaceborne systems, it is essential to consider the vulnerability of the specific technologies employed. If any of the component categories listed in Table 8.1 are part of the mission architecture, a dedicated assessment of their susceptibility to Total Non-Ionizing Dose (TNID) must be performed [2] and [4].

**Table 8.1:** Typical Displacement Damage Effects by Technology

Technology Category	Sub-category	Observed Effects
Bipolar Devices	BJT	Gain degradation ( $h_{FE}$ ), especially under low-current operation. PNP devices are typically more sensitive than NPN.
	Diodes	Increased leakage current, forward voltage shift
Electro-Optic Sensors	CCDs	CTE degradation, elevated dark current, appearance of hot pixels and bright columns, random telegraph noise
	APS	Elevated dark current, hot spots, reduced responsivity, temporal noise
	Photodiodes	Reduced photocurrent, increased dark current
	Phototransistors	$h_{FE}$ degradation, reduced responsivity, elevated dark current
Light-Emitting Devices	LEDs	Decline in optical power output
	Laser Diodes	Reduced output, higher threshold current
Optocouplers	–	Lower current transfer ratio
Optical Materials	Alkali halides, silica	Reduced light transmission due to structural damage

### Parameter-Specific Manifestations of DD

Displacement damage introduces point defects that compromise device operation in several characteristic ways. Key parameters and behaviors affected include:

- **Charge-Transfer Efficiency (CTE):** in CCDs, defect states act as traps, reducing pixel charge transfer and creating smearing artifacts.
- **Dark Current:** radiation-induced defects generate spurious charges in optical sensors, leading to elevated background signal.

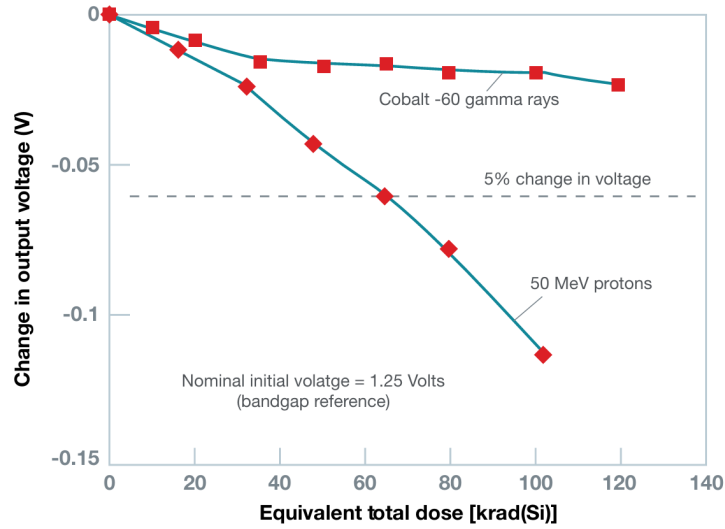


**Figure 8.2:** Voltage response of a PNP transistor to gamma-ray exposure (TID) vs. proton-induced displacement damage [6].

- **Hot Spots:** specific pixels may show abnormal brightness due to localized charge generation, often flagged as “bad pixels.”
- **Random Telegraph Signal (RTS):** temporal fluctuations between discrete dark current states due to charge trapping and release.
- **Bright Columns:** saturation in a pixel may propagate to downstream pixels during read-out, obscuring data.
- **Reduced Responsivity:** trapping reduces minority carrier lifetime, decreasing the effectiveness of photodetection or light emission.
- **Optical Output Degradation:** light-emitting components lose efficiency due to non-radiative recombination at defect sites.
- **Transistor Gain ( $h_{FE}$ ):** bipolar devices exhibit lowered gain due to increased recombination in the base region.

In bipolar junction transistors (BJTs), current amplification depends on the transport of minority carriers through the base. Displacement-induced traps increase recombination rates, requiring higher base currents to maintain performance, ultimately reducing gain. Devices with larger base regions, such as lateral BJTs, are especially vulnerable. Furthermore, PNP BJTs tend to suffer more from DD due to their typically lower base doping levels compared to NPN types.

As illustrated in Figure 8.2, PNP devices may exhibit minor degradation from ionizing radiation (TID), but significantly worse shifts under proton irradiation — underscoring the importance of including DD effects in total performance assessments.

### MOSFETs: More Resilient to DD

In contrast to bipolar and optical technologies, MOSFETs generally exhibit strong resilience to displacement damage. This robustness stems from two main factors:

- **Majority Carrier Operation:** because they rely primarily on majority carriers, defects affecting minority lifetimes have a limited impact.
- **Small Active Volume:** the conductive channel in a MOSFET is extremely thin, limiting the volume susceptible to damage and reducing the interaction cross-section for displacements.

Nonetheless, in extreme environments or long-duration missions, even MOSFETs may accumulate non-negligible damage, particularly in analog applications or where ultra-low leakage currents are required.

## 8.0.3 10.3 Displacement Damage: Phenomenology and Observation

A fundamental consequence of the interaction between radiation and matter is the transfer of energy from the incident particle to the medium. This energy can result in ionization, generating excess charge that contributes to Total Ionizing Dose (TID) and Single Event Effects (SEE) or in physical damage to the material's structure, known as displacement damage (DD), quantified through the Non-Ionizing Energy Loss (NIEL).

Displacement damage refers to the cumulative disruption of a semiconductor's crystalline lattice due to energetic particle impacts. While TID primarily affects surfaces and interfaces through trapped charges and oxide degradation, DD manifests as volumetric damage across the silicon bulk, gradually altering the material's electrical and optical properties.

Silicon wafers used in microelectronics are manufactured from high-purity, single-crystal material with minimal defect density. However, each incident high-energy particle capable of transferring energy above the atomic binding threshold can displace a silicon atom from its lattice site. This displacement produces a vacancy (a missing atom) and a corresponding interstitial defect (the displaced atom situated in a non-lattice position). These point defects can act as charge carrier traps and

over time, their accumulation can significantly affect carrier mobility, recombination lifetime and the overall performance of the device.

For instance, in bipolar junction transistors (BJTs), recombination centers introduced in the base reduce the minority carrier lifetime, increasing the base current required for a given collector current and degrading current gain. Although MOSFETs are generally more tolerant to DD, sufficiently high displacement doses can still lead to reduced drive strength and slower switching speeds due to reduced mobility and carrier density.

The extent and characteristics of DD depend on several factors: the particle type and energy, the radiation angle of incidence and the material properties of the target. As particles travel through matter, they lose energy via two primary mechanisms: ionization (charge generation) and non-ionizing interactions (atomic displacements). While the ionized charge typically recombines over short timescales, DD introduces persistent defects that remain embedded within the structure.

Unlike ionizing events, which occur with large cross-sections and lower energy thresholds (e.g., 3.6 eV in silicon to create an electron-hole pair), displacement events require higher energies, typically on the order of 15–25 eV, to create a stable vacancy. According to Seitz’s model, referenced in [2], the threshold for lattice displacement is estimated as four times the sublimation energy, though measured values carry significant uncertainty. This uncertainty directly impacts NIEL-based damage predictions.

Displacement damage is particularly concerning because the entire device volume can be affected, not just surface layers. While the energy lost to displacement events is only a small fraction of the total energy (usually 0.1% of ionizing energy loss), its long-lasting nature makes it critical for mission reliability.

## 8.0.4 10.4 Non-Ionizing Energy Loss (NIEL) Mechanisms

NIEL mechanisms describe how particles interact with atoms to create structural defects. Four principal mechanisms contribute to displacement damage in semiconductors:

1. **Coulomb Scattering (Low-Energy, Charged Particles Only):** at lower energies, charged particles like protons interact with atomic nuclei via electrostatic repulsion. If sufficient energy is transferred, the nucleus is displaced. This mechanism diminishes as particle energy increases.
2. **Elastic Nuclear Collisions:** incident particles, including neutrons and protons, may undergo elastic interactions with atomic nuclei, similar to billiard ball collisions. Momentum is conserved and the recoil nucleus may be displaced from the lattice, creating both vacancies and interstitials.

3. **Inelastic Nuclear Reactions:** in this process, the particle transfers energy to the nucleus, exciting it to a higher state. The nucleus may decay by emitting nucleons or nuclear fragments, each capable of causing further displacements as secondary particles.
4. **Energy Dissipation via Phonons:** as the primary and secondary particles slow down, they interact more effectively with the lattice vibrations (phonons), causing localized heating and enhanced atomic motion.

Coulomb scattering dominates at lower particle energies, while nuclear interactions become increasingly significant above 10 MeV. Neutrons primarily displace atoms through elastic scattering below 20 MeV, with inelastic processes dominating at higher energies. Electrons, due to their low mass, are less effective at generating displacements per fluence unit. Similarly, gamma rays induce displacements indirectly via secondary electrons, but the resulting DD is typically negligible and not representative of actual DD sensitivity.

The number of atomic displacements can be estimated using TNID, which represents the average non-ionizing energy deposited per unit mass of material. The widely used Kinchin–Pease model (referenced in ECSS-E-HB-10-12A) approximates the number of displacements based on the energy imparted to a recoil atom.

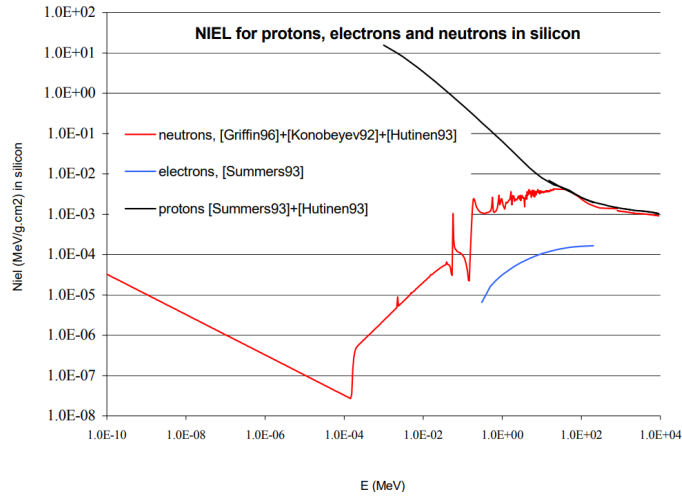


**Figure 8.3:** NIEL rate in silicon for protons, electrons and neutrons as a function of particle energy [2].

As shown in Figure 8.3, the NIEL rate for protons decreases at high energies due to the reduced elastic scattering cross-section, while electron-induced NIEL increases at low energies. Protons generally produce more displacements than neutrons at

low energies due to enhanced Coulomb scattering, while at high energies, both become comparable.

### 8.0.5 Impact of DD on Electrical Properties

The introduction of lattice defects creates localized energy states within the semiconductor bandgap. These defect states can influence device behavior in several ways, depending on operating temperature, material doping and device structure:

- **Thermal Generation:** traps can promote thermally generated electron-hole pairs, contributing to increased dark current in detectors.
- **Carrier Recombination:** traps act as recombination centers, reducing minority carrier lifetime, with critical effects in LEDs and laser diodes.
- **Carrier Trapping:** in CCDs and other imaging devices, trapped carriers can reduce charge transfer efficiency and mobility.
- **Donor/Acceptor Compensation:** displacement of atoms can neutralize dopants, altering carrier concentration and increasing resistance, e.g., in the collector of BJTs.
- **Tunneling and Leakage:** defect states near junctions enhance tunneling probability, increasing leakage currents in reverse-biased diodes, especially in small bandgap materials.

### 8.0.6 Radiation Damage Evaluation Strategy

Since DD severity depends strongly on particle type and energy, radiation environments are typically translated into equivalent mono-energetic fluences, commonly using 10 MeV protons or 1 MeV electrons, based on material-specific NIEL values. This approach simplifies component characterization and enables the use of standard test protocols.

Equivalent fluences are derived from mission-specific particle spectra (e.g., trapped protons, solar protons) and shielding configurations. Once the Displacement Damage Equivalent Fluence (DDEF) is known, irradiation tests are conducted using representative particle species and energies.

Testing should consider:

- Use of mono-energetic beams when a direct correlation between degradation and NIEL has been established.
- Energy selection ensuring penetration to the device's sensitive volume.

- Worst-case or representative degradation profiles when multi-energetic testing is not feasible.

Devices tested should be fabricated using the same process as the flight models. They should either:

- Be no more than 4 years older than the final radiation analysis date or
- Belong to the same diffusion lot as the FM components.

Bias conditions during irradiation must match or exceed worst-case operating scenarios to ensure representativity of results.

### **8.0.7 TNID Hardness Assurance Strategy**

Ensuring component robustness against displacement damage dose (DDD) begins with an accurate definition of the mission's radiation environment. This includes contributions from trapped and solar protons, electrons and secondary neutrons, evaluated according to [1] and [3].

As described in [4] and [30], once the environmental profile is established, the assessment of Total Non-Ionizing Dose (TNID) effects on the system and its components can be initiated. The fundamental requirement is that no radiation-induced displacement damage shall lead to permanent degradation, failure or performance drift outside defined specifications during the system's radiation design lifetime.



**Table 8.2:** Component families potentially sensitive to TNID [30]

Component Family	Sub-Family	TNIDL Threshold
Image Sensors	CCD, APS, CIS, others	All
Optoelectronics	Photodiodes, Phototransistors, LEDs, Optocouplers, Laser Diodes	All
PICs	All	All
Integrated Circuits	Bipolar / BiCMOS	$> 2 \times 10^{11}$ p/cm <sup>2</sup>
Diodes	Zener (Voltage reference)	$> 2 \times 10^{11}$ p/cm <sup>2</sup>
Transistors	BJT, IGBT	$> 2 \times 10^{11}$ p/cm <sup>2</sup>
Thyristors	All	$> 2 \times 10^{11}$ p/cm <sup>2</sup>

According to [4] and [30], each component must be evaluated for sensitivity to TNID, defining a TNID Hardness Assurance, as reported in ECSS-Q-ST-60-15C. The Total Non-Ionizing Dose Sensitivity (TNIDS) is the maximum dose a device can withstand without parametric or functional degradation exceeding mission specifications. TNIDS may be derived by:

- Identifying the threshold dose at which the worst-case part from the worst-case lot exceeds its limits (worst-case method) or
- Calculating the dose at which the one-sided tolerance limit, per MIL-HDBK-814, surpasses acceptable degradation thresholds with 90% confidence.

Acceptable TNID test data must satisfy the following:

- Testing must use protons or neutrons at energy levels representative of the space environment.
- Devices must be fabricated using the same technology and process as the flight models.
- Methods must comply with ESCC 22500 or appropriate MIL-STD-750 / MIL-STD-883 standards.

In the absence of legacy data, dedicated ground testing is required. Test plans must be submitted for approval and when possible, should use multi-energy proton irradiation to capture energy dependence of damage. Combined TID and TNID testing is acceptable if appropriately justified.

Component classification for test requirements is based on the ratio of TNIDS to TNIDL, as follows:

- **TNIDS > Maximum RDM × TNIDL:** No testing required.
- **Minimum RDM × TNIDL < TNIDS < Maximum RDM × TNIDL:** Qualification testing required.
- **TNIDS < Minimum RDM × TNIDL:** Use prohibited due to insufficient radiation tolerance.

For devices subject to displacement degradation, a Worst Case Analysis (WCA) must be conducted in line with ECSS-Q-ST-30 to ensure compliance at End of Life (EOL). The combined effects of TNID and TID must be used to define acceptable parameter drift margins.

TNIDL values shall be calculated using 3D Monte Carlo or ray-tracing techniques as specified in [1].

If the tested lot differs from the flight lot, Radiation Verification Testing (RVT) must be conducted. RVT is mandatory for:

- All lots of non-Silicon optoelectronics and image sensors,
- Any part where  $TNID\_RDM < \text{Maximum RDM}$ .

### 8.0.8 Displacement Damage Assurance Strategy for ARCap

For the ARCap module operating over a five-year mission lifetime, the effects of displacement damage (DDD) must be addressed through a tailored strategy. While much of the standard TNID evaluation process has been covered, additional considerations emerge when applying these principles to COTS-based systems and radiation-sensitive subsystems such as optoelectronics.

#### Environmental Modeling and NIEL Scaling

Displacement damage is primarily driven by trapped protons, solar proton events and secondary neutrons, particularly during passages through regions such as the South Atlantic Anomaly. The mission TNID environment shall be quantified using NIEL-weighted integration across the incident spectra and shielding configurations, following [1] recommendations.

Although damage is commonly expressed as an equivalent fluence of 50 MeV protons or 1 MeV neutrons, this NIEL-scaling assumption is only valid for conventional silicon-based devices. For technologies based on other semiconductors, additional testing is required to validate NIEL proportionality, as scaling errors may arise for non-standard materials.

### **Test Strategy and COTS Component Handling**

For ARCap, where the overarching goal is to adopt a sensor architecture leveraging COTS-based components, a rigorous displacement damage dose (DDD) test methodology remains essential. Multi-energy proton irradiation is particularly recommended to fully capture the energy dependence of displacement effects, ranging from isolated point defects to complex defect cluster formation. This approach is especially relevant for optoelectronic components, photodiodes, image sensors and discrete transistors.

However, for imaging systems, the architecture will rely on space-grade components, such as radiation-hardened CMOS image sensors, optical lenses, filters and mechanical housings, rather than commercial COTS modules. This decision stems from several constraints. First, we lack the in-house facilities and expertise required for the radiation-hardening of image sensors and cleanroom integration processes that COTS optical systems would demand to achieve space qualification. Secondly, using off-the-shelf space-qualified imaging modules ensures faster integration and validation, minimizing the technical and programmatic risks associated with custom camera development. As a result, while the majority of the ARCap sensor suite embraces a COTS-oriented philosophy, the imaging payload follows a more conservative approach to guarantee operational robustness in the harsh space environment.

Monoenergetic proton testing is allowed only if:

- A consistent correlation between NIEL and degradation is proven or
- The selected energy produces the worst-case degradation for the device under test.

### **TNID Limits and Data Interpretation**

TNID susceptibility shall be characterized through one of two approaches:

- Worst-case method: defining TNIDS as the threshold at which device parameters exceed specification limits.
- Statistical method: using the one-sided tolerance limit (e.g., per MIL-HDBK-814) to ensure at least 90% survival with 90% confidence.

Combined TID and TNID effects must be carefully deconvolved in test campaigns, ideally through separate gamma-only TID exposures.

### Radiation Design Margin and Protection Measures

TNID Radiation Design Margin (RDM) for ARCap shall be no less than 1.2. Where possible, uncertainty quantification using Monte Carlo simulation should support margin analysis. Any displacement damage analysis shall be supported by Worst Case Analysis (WCA), incorporating both TNID- and TID-induced parameter drifts.

For critical parts or those lacking heritage data, a risk-based approach should guide qualification testing. Radiation verification testing (RVT) shall be performed if the flight lot differs from the tested lot and when  $TNID\_RDM < 2$ .

### ARCap Strategy Summary

Displacement Damage Assurance Approach for ARCap:

1. **Define Environment.** Model the NIEL spectrum using ECSS-compliant tools and shielding profiles.
2. **Screen Components.** Identify minority-carrier and optoelectronic parts for DDD risk.
3. **Test and Validate.** Execute proton irradiation at multiple energies or validate monoenergetic worst-case correlation.
4. **Mitigate.** Use shielding, redundancy or conservative margining to protect sensitive functions.
5. **Analyze.** Perform WCA combining TNID and TID, applying RDM to all relevant parameters.
6. **Document.** Include TNID and RVT results in Radiation Analysis Reports for CDR.

Through this structured approach, the ARCap system can achieve mission assurance against displacement damage, ensuring robust subsystem functionality in the space environment over the full five-year mission lifetime.

# Chapter 9

## Single Event Effects

### 9.1 Introduction

Single Event Effects (SEEs) are physical phenomena caused by the charge deposited by a single energetic particle as it traverses a sensitive region within a device. The critical charge is defined as the minimum collected charge necessary to induce a SEE. SEEs can be caused by direct ionization from heavy ions or by nuclear reactions triggered by protons and neutrons. In the latter case, the incident nucleon transfers energy to a recoil atom through elastic, inelastic or spallation reactions. Although the cross-section for such reactions is low (around  $10^{-5}$  for most devices), high proton fluxes, particularly within the inner proton belt or during solar events, can make these mechanisms dominant in modern, low-LET threshold devices. Recoil nuclei from these interactions behave like heavy ions, with high localized energy deposition but short ranges.

SEEs can be broadly categorized as follows:

- **Destructive events:** Single Event Latch-up (SEL), Single Event Snapback (SESB), Single Event Dielectric Rupture (SEDR), Single Event Gate Rupture (SEGR), Single Event Breakdown (SEB).
- **Non-destructive events:** Single Event Transient (SET), Single Event Disturb (SED), Single Event Upset (SEU), Multiple-Cell Upset (MCU), Single-Word Multiple-Bit Upset (SMU), Single Event Functional Interrupt (SEFI), Single Event Hard Error (SEHE).

The information and content presented in this chapter have been reinterpreted and consolidated from sources [2], [6] and [45] with the objective of providing a unified and comprehensive overview of the problem.

### 9.1.1 Linear Energy Transfer (LET)

LET represents the energy deposited per unit path length by an ionizing particle, typically expressed in  $\text{MeV} \cdot \text{cm}^2/\text{mg}$ . It is a function of the target material's density, the particle's type and energy and the path length:

$$\text{LET}(x) \approx \frac{1}{\rho} \frac{dE}{dx}(x)$$

LET is not a monotonic function of energy or range; the maximum occurs at the Bragg peak. For heavy ions with energy above the threshold for  $e^- - h^+$  pair generation, an electron cascade is initiated. The charge generation is proportional to LET, with heavier ions (higher charge) creating more direct ionization. For a LET of  $97 \text{ MeV} \cdot \text{cm}^2/\text{mg}$ , about  $1 \text{ pC}/\mu\text{m}$  of charge is deposited in silicon. The deposited energy can be approximated by:

$$E_{\text{dep}} = \text{LET} \cdot d \cdot \rho$$

### 9.1.2 Cross Section

The SEE cross section quantifies the likelihood of an event and is defined as:

$$\sigma = \frac{\text{Number of SEEs}}{\text{Particle fluence}}$$

For heavy ions, the cross section depends on LET; for protons and neutrons, on energy. It is also sensitive to the incidence angle. In nuclear-interaction-induced SEEs, the cross section includes both the cross section incorporates the probability of a nucleon-nuclear interaction and the probability that the nuclear recoil and other recoil and other fragments results in sufficient charge density in the “correct” place of the semiconductor to induce an event. A representative curve showing the variation of the cross section as a function of the Linear Energy Transfer (LET) is presented in Figure 9.1. The curve highlights two key parameters: the saturation cross section ( $\sigma_{\text{sat}}$ ), which represents the maximum value the cross section can reach at high LET and the threshold LET ( $\text{LET}_{\text{th}}$ ), which defines the minimum LET required to trigger a single event effect.

### 9.1.3 Sensitive Volume

The sensitive volume (SV) or node is the region where charge collection may trigger a SEE. It is often modeled as a parallelepiped. The lateral size can be derived from the saturation cross section, while the vertical dimension is typically assumed to be around  $2 \times 10^{-6} \text{ m}$ . For advanced technologies, actual geometries can be obtained through dedicated experimental characterization methods.

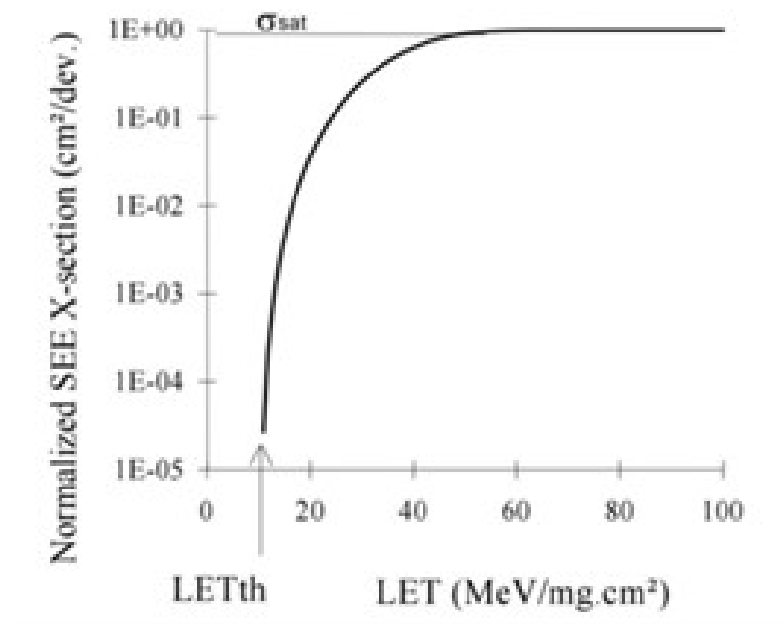


**Figure 9.1:** SEE cross section versus LET [2].

## 9.2 Destructive and Non-Destructive Single-Event Effects

Non-destructive SEEs manifest as transient disturbances or data corruption without causing permanent damage to the affected components. In combinational logic or analog circuits lacking memory, these disturbances are self-recovering; the circuit resumes normal operation after the excess charge dissipates. No external intervention is needed to restore the state once the nonequilibrium charge recombines or is transported away.

In systems with memory, such as sequential digital logic or analog components with memory elements, the radiation-induced charge can alter the stored data. Although overwriting the incorrect value will restore the device, the erroneous state can propagate and lead to malfunctions. These are referred to as soft errors since no physical damage occurs.

Certain low-current latch-up conditions and multiple-bit upsets also fall under non-destructive SEEs, provided they do not degrade device performance over time.

Destructive SEEs, in contrast, physically damage the device. They result in hard errors that are not recoverable by software or system-level interventions. Power electronic devices are especially vulnerable to:

- **Single Event Latch-up (SEL)**
- **Single Event Gate Rupture (SEGR)**
- **Single Event Burnout (SEB)**

In such cases, the device experiences catastrophic failure due to high voltage/current operation combined with the radiation-induced charge injection.

Shielding has a complex effect on SEE rates: while low-energy particles are attenuated, secondary particles generated within the shield by higher energy particles can increase SEE rates. For planetary missions, avionics systems must endure peak flux conditions and operate through radiation events, which often involve solar flares. Therefore, eliminating destructive failure modes is critical.

**SEE hardening** at the device level involves:

- Modifying chip layout (e.g., guard rings, insulating substrates)
- Increasing LET thresholds

**SEE mitigation** at higher levels includes:

- Error detection and correction
- Watchdog timers



- Triple Modular Redundancy (TMR)

A combination of device-level hardening, shielding and system-level fault tolerance is essential for ensuring reliability across all mission phases.

### 9.3 Energy Deposition and Charge Transport Mechanisms

SEEs primarily result from ionization, either directly (heavy ions, protons) or indirectly (neutrons via nuclear interactions), as illustrated in Figure 9.2. Heavy ions typically induce SEEs via direct ionization, while protons contribute through both direct and indirect mechanisms. Figure 9.2 illustrates these processes.

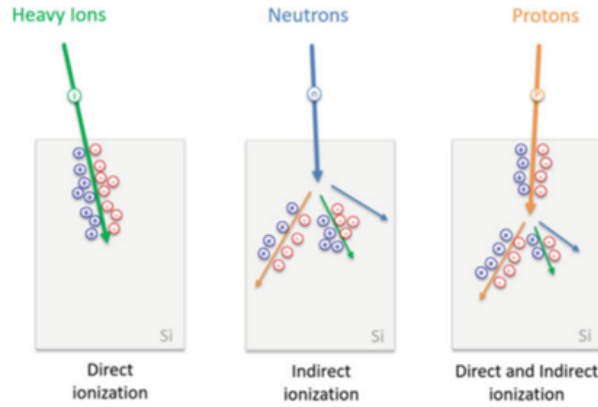


**Figure 9.2:** Direct and indirect ionization mechanisms for heavy ions, protons and neutrons [2].

Traditionally, only high-energy protons ( $E > 20$  MeV) were considered hazardous. However, in highly scaled technologies, even low-energy protons ( $E < 3$  MeV) have been shown to induce SEEs.

The energy loss per unit path length is described by stopping power  $S$ , which becomes independent of material phase when normalized by mass density:

$$\text{Mass stopping power} = \frac{S}{\rho}$$

LET, which represents the energy deposited in the material, is closely related but differs slightly from stopping power, particularly for particles where radiative losses are negligible.

Stopping power increases with energy up to the Bragg peak, after which it declines. Heavier ions have higher peaks due to stronger Coulomb interactions. Energy deposition results from:

- **Ionization:** Excitation of electrons across the bandgap
- **Nuclear interactions:** Causing lattice displacement or spallation

The range  $R$  of a particle is given by:

$$R = \int_{E_{\text{in}}}^0 \frac{1}{-\frac{dE}{dx}} dx$$

In silicon, the average energy to generate an electron-hole pair is approximately 3.6 eV, given by:

$$E_{\text{ehp}} \approx 2.73E_g + 0.55$$

where  $E_g = 1.11$  eV for silicon.

The deposited charge  $Q_D$  is expressed as:

$$Q_D = \frac{q \cdot S \cdot \rho \cdot l}{E_{\text{ehp}}}$$

where  $q$  is the elementary charge,  $l$  is the ionization path length within the sensitive volume and  $S$  is the surface mass stopping power. This charge must exceed the critical charge  $Q_{\text{crit}}$  to trigger a SEE.

Charge transport within the semiconductor occurs via:

- **Drift:** in high-field regions like reverse-biased p-n junctions
- **Diffusion:** driven by carrier concentration gradients

If the ion strike is close to the depletion region, funneling increases collection efficiency. Drift and funneling dominate initial charge collection, while diffusion contributes slower components and recombination losses.

## 9.4 Relevant Environment

SEE analysis must be conducted for systems operating in any of the following radiation environments:

- Trapped proton belts
- Solar protons and heavier ions
- Galactic cosmic-ray protons and heavier ions
- Secondary protons and neutrons (in special circumstances)

## 9.5 Technologies Susceptible to Single Event Effects

Many modern technologies are susceptible to SEEs. A summary of susceptibility is shown in Figure 9.3.

Component type	Technology	Family	Function	SEL	SESB	SEGR	SEB	SEU	MCU/SMU	SEDR	SEHE	SEFI	SET	SED
Transistors	Power MOS					X	X							
ICs	CMOS or BiCMOS or SOI	Digital	SRAM	X*				X	X		X			
			DRAM/SDRAM	X*	X			X	X		X	X		
			FPGA	X*				X		X		X		X
			EEPROM/Flash EEPROM	X*						X		X		X
			µP/µcontroller	X				X			X	X		X
		Mixed	ADC	X*				X				X	X	X
		Signal	DAC	X*				X				X	X	X
		Linear		X*						X			X	
	Bipolar	Digital						X					X	
		Linear						X					X	
Opto-electronics			Opto-couplers										X	
			CCD										X	
			APS (CMOS)	X								X	X	
*except SOI														

**Figure 9.3:** SEE susceptibility as a function of component technology and device family [2].

*Note: This chart is not exhaustive. Use of a listed technology warrants detailed SEE risk assessment.*

### Single Event Latch-up (SEL)

SEL occurs when a parasitic PNP thyristor structure is triggered, leading to excessive current and potential device destruction unless power is quickly removed. Bias and temperature affect susceptibility. Testing is typically done under maximum expected supply voltage and temperature.

### Single Event Snapback (SESB)

SESB is a localized high-current event, often indistinguishable from SEL but with key differences:

- SESB draws less current (localized effect)
- SESB is temperature independent
- SESB can often be cleared without full power-down

### Single Event Gate Rupture (SEGR) and Dielectric Rupture (SEDR)

SEGR involves high electric fields causing permanent damage to gate oxides. SEDR affects other dielectric structures, such as antifuses. Devices at risk include:

- Power MOSFETs (N- and P-channel)
- High-density ICs
- Capacitors with ultra-thin oxide layers

### Single Event Burnout (SEB)

SEB is a catastrophic failure mode where a vertical transistor in OFF-state is turned ON by a heavy ion, causing uncontrolled high current. Affected devices include:

- BJTs
- N-channel MOSFETs
- IGBTs

### Single Event Upset (SEU)

SEUs are non-destructive bit flips due to deposited charge exceeding  $Q_{\text{crit}} \sim 2V_{DD}C$ . The error can be corrected by rewriting. Affected technologies include:

- CMOS (bulk and SOI)
- Bipolar
- GaAs

### **Multiple Cell Upsets (MCUs)**

MCUs involve simultaneous upsets in adjacent or logically linked bits. Mechanisms include charge sharing, diffusion and direct ionization tracks. Sensitive circuits include DRAM and SDRAM.

### **Single Event Functional Interrupt (SEFI)**

SEFIs disrupt system function without causing bit errors or high current. Affected devices include:

- FPGAs
- DRAM/SDRAM
- Flash memory
- ADCs and DSPs

### **Single Event Hard Error (SEHE)**

SEHEs are irreversible failures such as “stuck bits” caused by oxide charging and leakage. Observed in:

- SRAMs (resistive load)
- DRAMs (with retention degradation)

Testing involves SEU-like methods but focuses on persistent errors and considers dose effects.

### **Single Event Transient (SET)**

SETs are short voltage pulses in analog or combinational digital circuits. If latched, they become SEUs. SET propagation is influenced by:

- Logical masking
- Electrical masking
- Latching window (temporal masking)

## 9.6 Prediction and Analysis of Single Event Effects in Electronic Components for Space Applications

This section details the methodology for predicting SEE rates, according [1] and [2], focusing on heavy-ion, proton and neutron interactions, while considering Total Ionizing Dose (TID) synergies and angle-of-incidence effects.

SEE rates must be assessed based on environmental conditions and using standardized prediction methodologies. The total ionizing dose accumulated in semiconductors can increase their susceptibility to SEE. In certain cases, this synergy must be evaluated to accurately estimate SEE rates in an operational environment. Experimental data from proton and ion beam irradiation tests may be used to assess SEE/TID interactions.

Shielding modifies the primary radiation spectrum and attenuates radiation flux. Component packaging may also influence shielding effectiveness and must be accounted for in the analysis. To obtain the predicted SEE rate of a component in space, it is necessary to perform four key points of Radiation Hardness Assurance (RHA):

- **Radiation environment models:** the mission radiation environment has to be calculated from radiation environments models defined in the ECSS-E-ST-10-04 standard.
- **Transport through shielding models:** since the EEE devices are not directly exposed to outer space, the radiation environment has to be transferred to component level via transport through shielding.
- **SEE component testing:** radiation sensitivity of each device has to be evaluated via radiation ground tests.
- **SEE rate prediction models:** once both the radiation environment and the device sensitivity are known, they can be fed into an SEE rate prediction model to obtain the predicted SEE rate of the component in space.

The method used to analyze the need for SEE (Single Event Effects) risk reduction depends on the possibility of calculating a SEE rate. When it is technically possible to determine the SEE error rate, for example, in the case of single event upset (SEU), single event transient (SET) or single event latch-up, the approach involves combining an experimental sensitivity curve with the appropriate environmental parameters to estimate the rate of errors.

When an energetic ion traverses a device, it deposits energy along its path by creating a dense plasma of electron–hole pairs. If these charges are generated near

a sensitive node, such as a p–n junction within a transistor, they can be collected and if their magnitude exceeds a certain threshold, a soft error (like an upset) can occur. The rate at which these upsets happen depends on the available charge collection paths within the sensitive volume of the device. In most analyses, this sensitive volume is initially assumed to be a rectangular parallelepiped (RPP). This leads to two distinct methods for calculating SEE rates: one based on the conventional RPP model and another based on an integrated RPP (IRPP) model.

In the basic RPP model, the energy deposited  $E_{\text{dep}}$  by an incident ion in the sensitive volume is estimated by the relation:

$$E_{\text{dep}} = \rho \cdot d \cdot \text{LET}$$

where  $\rho$  is the density of the material,  $d$  is the effective thickness of the sensitive volume and LET (Linear Energy Transfer) represents the energy deposition per unit path length. As the name suggests, the RPP model assumes that the sensitive volume is a rectangular parallelepiped with the top surface area  $S = X \times Y$  equal to the saturation cross-section  $\sigma_{\text{sat}}$  determined by heavy ion ground tests. In reality, the saturation cross-section  $\sigma_{\text{sat}}$  may actually not be squared, but assuming a ratio of one between the two area dimensions is standard practice because it leads to the highest SEE rate, i.e., worst-case scenario. The thickness  $Z$ , also referred to as sensitive volume thickness  $SV_t$ , is much harder to determine. It depends on the device technology and is often the least known parameter. An upset is assumed to occur when the deposited energy exceeds a threshold value, which is related to a threshold LET ( $\text{LET}_{\text{th}}$ ).

To calculate the upset rate, the LET spectrum of the incident particles is evaluated. In the [1] standard, three recommended RPP formulations are provided: the Bradford formula, the Pickel formula and the Blandford-Adams formula. One widely used expression is given by Bradford's formula, where the upset rate  $N$  is calculated as:

$$N = \frac{A}{4} \int_{\text{LET}_{\text{min}}}^{\text{LET}_{\text{max}}} \frac{d\phi}{d(\text{LET})}(\text{LET}) \cdot P_{\text{cl}}(> D(\text{LET})) d(\text{LET})$$

where  $\frac{d\phi}{d(\text{LET})}$  is the differential ion flux spectrum integrated over  $4\pi$  steradians,  $\text{LET}_{\text{min}}$  is the minimum LET required to upset the cell,  $\text{LET}_{\text{max}}$  is the maximum LET of the incident distribution and  $P_{\text{cl}}(> D(\text{LET}))$  is the integral chord length distribution.

This chord length distribution gives the probability that a particle travels through the sensitive volume with a pathlength greater than  $D(\text{LET})$ , considering that GCRs in space have an omnidirectional flux. A simplified version of the equation can be written in terms of the dimensions of the sensitive volume (length  $l$ , width  $w$  and height  $h$ ) and its total surface area  $A$ .

These RPP models assume a constant critical LET value, which is a simplification. In reality, the critical LETs form a distribution, often modeled using a Weibull function. This motivates the use of the Integrated RPP (IRPP) model, where the upset rate is:

$$N_{\text{IRPP}} = \frac{1}{\sigma_{\text{sat}}} \int_{\text{LET}_{i,\text{min}}}^{\text{LET}_{i,\text{max}}} \frac{d\sigma_{\text{ion}}}{d\text{LET}}(\text{LET}_i) \cdot N_{\text{RPP}}(\text{LET}_i) d\text{LET}_i$$

where  $\sigma_{\text{sat}}$  is the saturation cross-section and  $\frac{d\sigma_{\text{ion}}}{d\text{LET}}$  is the differential cross-section.

For proton and neutron interactions, SEE rates must be computed differently due to indirect ionization. The rate is expressed as:

$$N = \int_{E_{\text{min}}}^{E_{\text{max}}} \frac{d\phi}{dE}(E) \cdot \sigma_{\text{nucleon}}(E) dE$$

where  $\frac{d\phi}{dE}$  is the omnidirectional proton or neutron flux and  $\sigma_{\text{nucleon}}(E)$  is the SEE cross-section as a function of energy. An alternative approach involves simulating energy deposition spectra  $\frac{dP}{d\epsilon}(E, \epsilon)$ , with an upset assumed if  $\epsilon > \epsilon_C$ , but this is typically less accurate than direct cross-section integration.

Commonly used prediction tools include CREME, SPENVIS, OMERE, Geant4, FLUKA and MCNPX. These models often assume identical parallelepiped sensitive volumes and LET tracks smaller than minimum feature sizes, which is no longer true in modern nanometer-scale technologies. Sensitive volume thickness  $SV_t$  is often fixed (e.g., 2  $\mu\text{m}$ ) without experimental validation. One objective of radiation assurance is verifying if such assumptions are transferable between different missions.

Additionally, for effects such as SEGR or SEB where a rate is hard to quantify, derating and mitigation techniques are applied as per ECSS-Q-ST-60-15C [4] and [30]. For complex effects like SET or SED, where test results are strongly dependent on circuit conditions (e.g., supply voltage, frequency), simulation-based analyses are used. These simulate perturbation signals through the final design to evaluate vulnerabilities and system-level impact.

In summary, SEE rate prediction integrates experimental cross-sections with mission-specific radiation spectra, considering geometry, physical modeling and statistical uncertainties. Combined with derating and mitigation strategies, this framework supports the reliable design of radiation-hardened space electronics.

## 9.7 SEE Hardness Assurance

Single Event Effects (SEEs) must be carefully characterized, as described in [4] and [30], to ensure that they do not cause permanent damage to any system or subsystem, nor should they lead to performance anomalies or outages that conflict with mission requirements.



According to [5] and [30], SEE test data must meet specific validation criteria. Power MOSFETs should be tested in accordance with MIL-STD-750, Method 1080. All other components must follow the ESCC 25100 standard.

To ensure technology consistency, tested components must be fabricated using the same process and diffusion mask as the flight hardware. Furthermore, test conditions must be equivalent to or more severe than those expected during the mission. If no acceptable test data is available, heavy-ion ground testing must be conducted to evaluate SEE susceptibility.

Proton testing for SEE analysis should be conducted based on the Linear Energy Transfer threshold ( $LET_{th}$ ) of the candidate device. If  $LET_{th} > 60 \text{ MeV} \cdot \text{cm}^2/\text{mg}$ , no further analysis is required, as the component is generally considered immune to SEE in space. For devices with lower thresholds, additional assessment must be carried out as specified in Table 9.1.

**Table 9.1:** Radiation environment to be assessed based on  $LET_{th}$  [4]

$LET_{th}$ ( $\text{MeV} \cdot \text{cm}^2/\text{mg}$ )	Environments to be considered
$< 15$	Heavy ions (Galactic Cosmic Rays, solar event ions), protons (trapped protons, solar event protons)
$15 - 60$	Heavy ions (Galactic Cosmic Rays, solar event ions)
$> 60$	No further analysis required

For devices with  $LET_{th} < 60 \text{ MeV} \cdot \text{cm}^2/\text{mg}$ , SEE analysis must be performed. If  $LET_{th} < 15 \text{ MeV} \cdot \text{cm}^2/\text{mg}$ , an additional sensitivity analysis for proton-induced effects must be included. This applies even to components that are specifically designed to be SEE-hardened. In particular, high-Z materials near the sensitive volume may lead to the generation of secondary particles with LET values exceeding  $15 \text{ MeV} \cdot \text{cm}^2/\text{mg}$  and must therefore be considered.

For devices manufactured from materials other than silicon (e.g., GaAs), LET threshold values must be recalculated appropriately. Additionally, any proton SEE test data must meet the applicable validation criteria. If such data is not available, dedicated proton ground testing must be conducted.

The use of simulation tools to derive proton SEU cross-section curves from heavy-ion data must be approved by the customer.

For any component that is not immune to destructive SEEs, it must be demonstrated that the probability of occurrence in the mission environment is at least one order of magnitude lower than the intrinsic failure rate of the component. Destructive SEE mechanisms to be considered include:

- Single Event Latch-up (SEL)
- Single Event Burnout (SEB)

- Single Event Gate Rupture (SEGR)
- Single Event Dielectric Rupture (SEDR)

In the specific case of SEB or SEGR susceptibility in power MOSFETs, one of the following two methods must be adopted:

1. Estimation of failure rate from SEB/SEGR cross-section vs. equivalent LET curves.
2. Derating of maximum drain-source ( $V_{DS,max}$ ) and gate-source off-state voltages ( $V_{GS,off\ max}$ ) according to the Safe Operating Area (SOA).

Due to the deep sensitive volume in power MOSFETs, LET values may vary significantly along the ion path and this must be taken into account in the analysis.

For non-destructive SEE mechanisms such as SEU, SET, MCU and SEFI, the criticality of the component in its application must be analyzed, taking into account the possible impact at subsystem and system level. In the specific case of SETs in analog ICs, the selected analysis method, whether based on circuit simulations or physical injection, must be submitted for customer approval.

If a SEE is considered critical or potentially critical for a specific component or application, the mission event rate must be calculated both for the mission background environment and for a solar event environment, according to the radiation environment specification defined in [1]. A Radiation Design Margin (RDM) must be applied:

- An RDM of 10 should be used when the proton error rate is derived from heavy-ion simulation data.
- No RDM is applied when the rate is based on actual proton test data.

**Table 9.2:** SEE types to be considered in accordance with ECSS-Q-ST-60-15C [4] and [30]

Non-destructive SEEs	Destructive SEEs
SEU, SET, MCU, SEFI	SEL, SEB, SEGR, SEDR

The final calculated SEE rates must ensure that the application satisfies the required availability, performance and reliability criteria.

If these requirements are not met, the following actions must be taken:

- For any component not immune to destructive SEE, the probability of occurrence in the mission environment must be shown to be more than ten times lower than the intrinsic failure rate.

- The calculated SEE event rates must ensure compliance with overall mission performance and reliability requirements.

When these conditions are not satisfied, mitigation techniques must be implemented to eliminate the risk of damage or degradation outside specification limits. These techniques must be validated by analysis or by testing.

## Chapter 10

# Design Trade-offs and Evolution of Radiation Requirements

### 10.1 From Ambition to Realism: Refocusing on a LEO Mission Profile

The initial scope of the ARCap module aimed to deliver a sensor and robotic suite qualified for operation across any Earth orbit, including the most severe radiation environments. This universal ambition was driven by the desire to ensure compatibility with a wide range of future orbital servicing missions. To this end, a synthetic “worst-case” orbit was constructed by combining cumulative fluxes from the most aggressive trapped radiation belts, galactic cosmic rays (GCRs) and solar energetic particle events (SEPs). However, as the project matured, both technical constraints and business considerations necessitated a strategic revision of this objective.

During the development process, it became evident that the ARCap concept, comprising a modular array of vision systems, radar and robotic manipulators, many inspired by or derived from automotive and industrial-grade technologies, cannot be designed from the ground up for extreme radiation resilience. The platform relies heavily on COTS components for cost and development velocity, which fundamentally limit its suitability for environments characterized by high linear energy transfer (LET) particles and prolonged total ionizing dose (TID) accumulation.

A significant turning point occurred during the design phase A, when the initial objective of qualifying the module for an abstract worst-case orbit was reconsidered.

Faced with emerging technical and economic constraints, the development team shifted focus toward defining a more practical and market-aligned mission profile, tailored to realistic deployment scenarios. The team identified Low Earth Orbit (LEO) as the most commercially viable environment for ARCap’s initial deployment. This decision was based on three major factors:

1. **Technical Feasibility with COTS:** the synthetic worst-case environment proved incompatible with the endurance limits of COTS electronics. Even with aggressive shielding estimates, survivability for a 5-year mission could not be guaranteed without resorting to full radiation-hardened redesigns, an undertaking both cost-prohibitive and incompatible with a startup’s agility.
2. **Avoiding Over-engineering:** designing for extreme radiation conditions would have imposed significant penalties in terms of mass, volume and power. Excessive shielding or redundant architectural choices, while theoretically viable, would violate the design-to-cost and rapid time-to-market principles foundational to the ARCap roadmap.
3. **Market-Driven Alignment:** analysis of public and private servicing initiatives indicated that the majority of near-term commercial missions are constrained to LEO. By tailoring ARCap’s qualification strategy around a 5-year LEO mission, the design aligns with actual customer needs while reducing both technical and financial risk.

This reframing of requirements does not dilute the robustness of the design; rather, it introduces a clear scope boundary that enhances traceability and engineering rigor. The current baseline assumes operations in LEO under geomagnetic shielding, where trapped electron and proton fluxes dominate the radiation profile and GCRs and SEPs are significantly attenuated. This allows for controlled radiation design margin (RDM) allocation and realistic mitigation strategies without compromising ARCap’s functionality or economics.

This iterative approach, starting from a broad, exploratory objective and narrowing down to a focused, feasible path, reflects the adaptive nature of early-phase system engineering within a resource-constrained context.

## 10.2 Radiation Environment Requirements for a 5-Year LEO Mission

### 10.2.1 Component Radiation Requirements and Selection Strategy

This section outlines the key drivers governing the selection of radiation-tolerant or radiation-hardened (rad-hard) components for the 5-year Low Earth Orbit (LEO) mission. Central to this analysis is the rigorous requirement of a 5-year mission lifetime, which directly informs the Total Ionizing Dose (TID) tolerance criteria, a fundamental specification for components operating in radiation-intensive environments.

The TID threshold was derived by extrapolating dose depth curves under the assumption of 5 mm aluminum shielding (Table 10.1), followed by the application of a Radiation Design Margin (RDM) of 2.5 to ensure operational reliability. Components exceeding the calculated threshold of TIDL, as  $RDM \times TIDL$  at 5 mm Al, are deemed compliant without further testing. Conversely, components with TID-S/TIDL ratings below 2.5 but above a minimum RDM necessitate additional validation through targeted analysis and testing.

### 10.2.2 Total Ionizing Dose (TID) Requirements

**Table 10.1:** Total ionizing dose versus aluminum thickness for a 5-year LEO mission

Shielding [mm]	OMERE [rad]	SPENVIS [rad]	Worst-case [rad]
0.5	$2.74 \times 10^5$	$3.11 \times 10^5$	$3.11 \times 10^5$
1.0	$9.21 \times 10^4$	$9.56 \times 10^4$	$9.56 \times 10^4$
2.0	$3.47 \times 10^4$	$3.49 \times 10^4$	$3.49 \times 10^4$
5.0	$7.86 \times 10^3$	$7.79 \times 10^3$	$7.86 \times 10^3$

According to Table 10.1, the TID requirements for compliant components are as follow:

- **GENERAL REQUIREMENT:**  $TIDS \geq 20 \text{ krad(Si)}$ 
  - **REQ.1:**  $TIDS \geq 20 \text{ krad(Si)}$

If this requirement is satisfied, the component is accepted without further testing.

- **REQ.2:**  $12.3 \text{ krad(Si)} \leq \text{TIDS} < 20 \text{ krad(Si)}$

If this condition holds, Radiation Verification Testing (RVT) on the flight lot is required.

- **REQ.3:**  $\text{TIDS} < 12.3 \text{ krad(Si)}$

If this condition applies, the use of the component is prohibited

The Minimum Radiation Design Margin (MRDM) is computed by multiplying two independent margins:

$$\text{MRDM} = \text{RDM}_1 \times \text{RDM}_2 = 1.2 \times 1.3 = 1.56 \quad (10.1)$$

where:

- $\text{RDM}_1 = 1.2$ : linked to test uncertainties (ECSS-Q-ST-60-15C-Rev1)
- $\text{RDM}_2 = 1.3$ : linked to simulation/modeling uncertainties

The maximum acceptable RDM threshold, beyond which no additional testing on the component lot is required, is fixed to 2.5. This corresponds to the condition:

$$\frac{\text{TIDS}}{\text{TIDL}} > 2.5 \quad (10.2)$$

where TIDL is the dose level at the end of mission, i.e. the environmental dose estimated under 5 mm Al shielding, equal to 7.86 krad(Si). The minimum threshold, below which the component is deemed non-compliant with the environment and must be discarded, is defined as:

$$\frac{\text{TIDS}}{\text{TIDL}} < 1.56 \quad (10.3)$$

For clarity, the following thresholds are used in the component qualification process:

- Minimum threshold:  $\text{MRDM} \times \text{TIDL}$  of 7.86 krad(Si) = 12.3 krad (Si)
- Nominal threshold:  $\text{RDM} \times \text{TIDL}$  of 7.86 krad(Si) = 20 krad (Si)

If no acceptable TID test data or datasheets exist for a component, ground testing shall be performed in conformance with ESCC 22900 [47]. If the diffusion lot number of the flight model part differs from that of the tested part, RVT must be performed under the following conditions:

- For optoelectronic parts: all lots

- For all other parts: if TID RDM  $< 2.5$

Acceptable TID test data must comply with the following rules:

- Tests must follow ESCC 22900 [47], MIL-STD-883L method 1019 or MIL-STD-750E method 1019
- Bipolar devices must be tested at dose rates below 360 rad/h
- Tested devices must share identical technology, diffusion mask and wafer fabrication process with flight parts
- Test bias conditions must be worse or equivalent to operational use

### 10.2.3 Driven Screening Philosophy

While TNID and SEE susceptibility are assessed via vendor test reports and existing databases, TID remains the primary filter for component selection. This is because TID represents the cumulative degradation a component experiences over time and serves as a conservative indicator of compatibility with the space radiation environment. In both screening workflows and qualification testing, TID is typically the first parameter evaluated: if a component fails to withstand the expected accumulated dose, it is generally excluded from further consideration. Moreover, limited TID tolerance often correlates with increased susceptibility to SEE, as accumulated damage can lower the threshold for transient failures. For these reasons, TID acts as both a quantitative qualification threshold and a practical, early-stage selection criterion. Once TID compliance is verified, TNID and SEE considerations are used to refine the assessment.

The LEO environment, though more benign than GEO or interplanetary settings, still necessitates strict adherence to the TID threshold due to the use of commercial-grade components. Screening ensures compliance, while future work will consider potential reduction in the compounded RDM based on increasing confidence in modeling tools and test repeatability. A rational reduction to  $\sim 1.8$  could lower the threshold without compromising reliability, enabling broader use of COTS components.

The urgency to reach space as quickly as possible is more pressing than ever, driven by the need to meet increasingly demanding operational requirements with reliable technology.

In this space race, characterized by tighter time and budget constraints, the use of COTS components is becoming increasingly common as an alternative to traditional space-grade components. While COTS offer advantages in terms of cost and availability, their resistance to radiation is often lower, requiring careful selection and appropriate mitigation strategies.

Mainly, the use of commercial parts must be able to ensure:



1. **Assured Operational Lifetime:** ensuring that space systems remain functional throughout their intended mission duration is a critical challenge. Satellites must withstand the harsh space environment, including radiation, thermal extremes and mechanical stress, without performance degradation. Reliability is key, requiring rigorous component selection, testing and radiation-hardening strategies to mitigate risks and extend operational lifetime.
2. **Rapid Development on a Moderate Budget:** the growing demand for space capabilities has accelerated development timelines while imposing tighter budget constraints. This has led to an increased reliance on COTS components, which offer cost and availability advantages. However, using COTS in space introduces challenges, particularly in radiation resilience, necessitating strategic engineering solutions to balance performance, cost and mission success.
3. **Performance-Driven Necessity in the Absence of Rad-Hard Equivalents:** in many cases, the desired performance or advanced functionality required for modern space missions cannot be achieved using radiation-hardened components. This drives the adoption of COTS components, which incorporate cutting-edge advancements in processing speed, power efficiency or miniaturization unavailable in traditional rad-hard offerings.

According to [34], there are three different approaches to spacecraft parts selection: radiation hardened/space grade, buy-and-fly and a middle path called “Careful COTS”. These require system-level strategies, rigorous screening processes and controlled manufacturing oversight. One critical aspect is **Lot Control**, as radiation tolerance can vary significantly across different production batches due to fabrication process changes. Maintaining traceability is therefore essential to ensure that the flight hardware precisely matches the lot that was tested. **Burn-in and Screening** procedures are equally important, as most early-life failures occur shortly after deployment. Subjecting components to burn-in and radiation testing helps identify and select parts with acceptable reliability for integration into the Flight Model. Finally, **Subsystem Qualification** presents greater challenges compared to individual components. The probability of survival decreases rapidly when multiple components are combined. For instance, the probability of 10 components each with 90% radiation tolerance surviving as a system is only 35% ( $0.9^{10}$ ).

## Radiation Testing Techniques

Radiation testing ensures survivability in orbit and is categorized, as described in [34] and [46], into:

- **Cobalt-60 (Gamma Ray):** deep penetration; TID-focused; should be the worst case for space applications; no SEEs.
- **Proton Testing:** balanced and preferred for SEU/SEFI characterization and SEL/SEB/SEGRA susceptibility screening; enables also TID testing. In particular, low-energy protons have high LET but low range, so their penetration allows to produce high-LET recoils (up to 25 MeV cm<sup>2</sup>/mg) in materials like Al or Cu.
- **Heavy Ion Testing:** for highly sensitive SEE studies; costly and less accessible.

## 10.3 Comparison of Gamma and X-Ray Sources for TID Testing

### 10.3.1 Gamma Rays vs. X-Rays

According to [47], gamma rays from isotopes like Cobalt-60 (60-Co) have long been the reference for Total Ionizing Dose (TID) testing due to their deep penetration and well-understood interaction physics, mainly Compton scattering. However, they present logistical and safety challenges: they require shielding, controlled environments and handling of radioactive materials, as described in [48] and [49].

X-ray generators, on the other hand, are electrically powered, switchable, safer to operate and allow for quicker turnarounds. They can achieve high dose rates and are suitable for fast screening, though they typically produce photons with lower energy spectra compared to 60-Co.

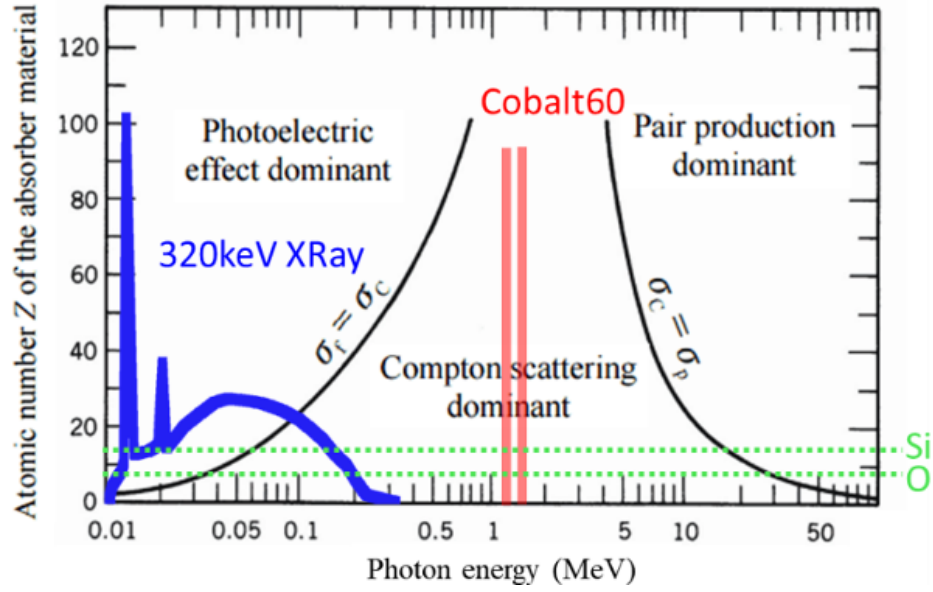


**Figure 10.1:** Comparison of the photon spectrum of the used X-ray generator and 60-Co source with the relative importance of the photoelectric effect, Compton scattering and pair production [49].

A representation of both the photon spectrum of the used X-ray generator and the 60-Co source is shown in Figure 10.1, highlighting the dominant interaction processes. As reported in [49], while 60-Co emissions are centered at 1.17 and 1.33 MeV and interact mainly through Compton scattering, X-ray generators emit broader spectra. Low-energy photons tend to dominate the photoelectric effect, leading to shallow penetration and higher dose enhancement in high-Z materials.

These characteristics make low-energy X-ray generators unsuitable for system-level testing. Their penetration is insufficient for fully packaged devices unless delidded and their results often exhibit strong dependence on atomic number due to variability in mass energy-absorption coefficients.

### 10.3.2 Low-Energy X-Rays vs. High-Energy X-Rays

High-energy X-rays up to 320 keV, as demonstrated in [49], provide deeper penetration and more uniform energy deposition. When filtered (e.g., with Pb and Al), low-energy photon components are suppressed, reducing the photoelectric effect and mimicking the behavior of gamma rays in terms of dominant Compton interactions.

This spectral shaping significantly improves the reliability of TID results for packaged components, enabling system-level screening in a safer and more flexible way than traditional gamma sources.

The study [49] demonstrates that using a filtered high-energy X-ray generator can produce TID degradation results comparable to those from Co-60 irradiation. Key findings include:

- Pb filters significantly reduce low-energy photons, minimizing dose enhancement and matching Co-60 profiles.
- MOSFET and bipolar transistor tests showed that degradation with high-energy filtered X-rays approached within 10–15% of Co-60.
- The difference in degradation between Al and Al+Pb filters confirms that filtering is essential to approximate real orbital radiation effects.
- Annealing effects were minimal, validating the robustness of test results.

High-energy X-ray generators offer a flexible and widely accessible platform for preliminary TID testing, particularly valuable when evaluating COTS components. These systems, traditionally employed in the space sector for non-destructive tomographic inspections following mechanical tests, can also be repurposed as irradiation sources. This dual-use potential represents a significant advantage, allowing facilities already equipped with such systems to support early-phase radiation evaluation without the need for specialized gamma sources.

X-ray generators are capable of delivering high dose rates and are compatible with packaged devices, making them suitable for iterative testing during the initial screening of candidate components. The following practices are recommended in [49] to optimize the irradiation conditions:

- Use of lead (Pb) filters to suppress low-energy photon components that may lead to non-uniform or excessive surface dose;
- Operating the generator at maximum voltage to enhance the dominance of Compton scattering over the photoelectric effect, improving dose deposition uniformity in silicon.

Despite these advantages, several limitations must be considered. Unlike gamma-ray sources such as Co-60, where the irradiation setup (e.g., pool configurations) provides a quasi-uniform and isotropic dose distribution around the device under test (DUT), X-ray generators produce highly directional beams. In this case, the dose received by the DUT depends significantly on both radial distance from the source and lateral positioning within the beam profile. As a result, when testing multiple components simultaneously, a circumferential arrangement is often required to ensure dose uniformity. Components positioned closer to the source or directly in the beam axis will inherently receive a higher dose rate compared to those placed peripherally or further away.

Moreover, X-ray systems typically operate with fixed dosimetry settings, limiting the flexibility to fine-tune irradiation parameters for different technologies or degradation models, practical examples are in the order of 1 krad/h. This is in contrast to gamma-based platforms, where exposure conditions can be adapted more precisely to match test specifications.

Additionally, contrary to some assumptions, X-ray-based testing is not inherently more cost-effective. Facilities using these generators are often optimized for short-duration diagnostic use, for instance, 1–2 hours for tomography. When repurposed for long-duration irradiations (several hours or more), rental costs can increase significantly, especially if service providers do not differentiate between diagnostic imaging and sustained radiation testing in their pricing structures.

### 10.3.3 Test Outcome Classification

The interpretation of radiation test results is essential to establishing a component's suitability for space applications. As reported in [34], results are typically classified into one of three categories: *unqualified success*, *marginal success* or *failure*.

**Unqualified Success:** a test is considered an unqualified success if all of the following conditions are satisfied:

- No destructive single-event effects (SEE) were observed. This indicates that the component did not experience any irreversible or catastrophic damage during testing.
- The single-event upset (SEU) rate is manageable within the context of the system. SEUs may occur but are correctable through software or hardware mitigation without compromising system-level functionality.
- The component remains functional up to the minimum threshold of mission dose, in our case 12.3 krad. This means the component retains its performance across the total dose expected in the mission.
- The component is functional after annealing at the nominal threshold, in our case 20 krad, showing resilience and excess margin. This demonstrates that even under accumulated stress and partial recovery, performance remains acceptable.

Meeting all these criteria qualifies the component as radiation-tolerant for the intended mission without further modifications.

**Marginal Success:** a result is deemed a marginal success if:

- No destructive SEE was observed;
- SEU rates are still manageable;
- The unit remains functional after annealing following the expected minimum threshold of mission dose.

This outcome suggests potential for qualification, though some mitigation strategies may be needed:

- *Reducing mission duration* to limit exposure;
- *Applying additional shielding*, locally or globally, to reduce the accumulated dose.

These compensatory actions may allow the use of the component without further testing.

**Failure:** a failure is declared when any of the following occurs:

- Destructive SEE was observed, such as latch-up or burnout leading to permanent failure;
- The SEU rate is unmanageable and impairs system reliability;
- The device fails to function after annealing to the minimum threshold of mission dose.

In such cases, the component must be excluded from flight hardware. If no viable alternative exists, design changes or system-level redundancies may be required, followed by a new round of testing.

#### 10.3.4 Final Technical Considerations for SEE Risk Assessment and Mitigation in COTS-Based ARCap Subsystems

Designing spaceborne electronics for ARCap necessitates a robust radiation assurance strategy, particularly in the realm of Single Event Effects (SEEs). While prior sections of this thesis have elaborated on SEE phenomenology and prediction models, this final section consolidates engineering-oriented guidance tailored to ARCap’s architectural and programmatic realities. Drawing from NASA’s SEECA framework [28] and informed by contemporary failure-mode and effects analysis (FMECA) practices, this synthesis provides a structured pathway to navigating

SEE-induced vulnerabilities when relying on commercial-off-the-shelf (COTS) components. More broadly, the methodological foundations adopted throughout this thesis, particularly the logic of identifying failure mechanisms, evaluating their criticality and acting either upstream through design or downstream via mitigation, are consistently inspired by four core references [28], [51], [52] and [53]. These documents served not only as technical guidance for Single Event Effects analysis, but also as a conceptual framework underpinning the system-level approach to risk assessment, decision-making and radiation hardness assurance as a whole.

COTS components present an appealing cost-performance tradeoff, but they introduce a significant risk in radiation-rich environments due to their undocumented susceptibility to SEEs and the lack of design margin transparency. In particular, advanced digital SoCs, high-speed ADCs, power MOSFETs and dense memory architectures are all prone to functional interruption or even destruction when exposed to high-energy particles. These risks are exacerbated by short production lifecycles and poor traceability in silicon process or mask-set changes, making mission-long reliability assurance complex. Mitigation begins with a structured approach to Radiation Hardness Assurance (RHA), as defined in the SEECA methodology.

The SEECA framework embeds RHA throughout the mission lifecycle. It requires early functional analysis that maps subsystem criticality across the Mission, Environment, Application and Lifetime (MEAL) context. This means not just modeling the expected fluxes in LEO but correlating them with phase-specific availability constraints: an ADC driving real-time robotic feedback in docking operations must meet zero-interruption guarantees during transient-rich radiation events like solar particle episodes. Therefore, system-level criticality analysis must inform part selection, testing and mitigation efforts from the earliest design phase.

Failure mode, effects and criticality analysis (FMECA) complements SEECA by categorizing functional units according to fault impact and severity. A SEE may lead to a fault condition such as reset, data corruption or functional block disablement. These must be traced through the system architecture to identify their propagation path and potential mitigation points. The ARCap SEE mitigation process must follow FMECA logic: each component's SEE failure modes must be mapped to functional effects, ranked by severity (from negligible to catastrophic) and matched with mitigation or design isolation layers.

NASA's SEECA guidelines [51] recommend criticality classification into three levels:

- **Error-Critical:** SEEs in these functions result in unrecoverable mission impact or permanent loss. These are the highest priority for part hardening or architectural redundancy.
- **Error-Vulnerable:** SEEs can lead to degraded but recoverable performance;

these functions require mitigation like watchdog resets or error-correcting protocols.

- **Error-Functional:** these tolerate some SEE-induced faults without violating system performance or availability margins. Typical examples include buffered telemetry or logging systems.

For ARCap, critical functions include robotic arm control, sensor timing chains and power management. Any destructive SEE like SEL in these blocks must trigger a protection protocol such as current limiting and autonomous power cycling. Power MOSFETs, particularly in high-current drive circuits, must be validated against SEGR/SEB under worst-case drain and gate voltage configurations. Whenever possible, operating voltages should be derated below safe operating area (SOA) limits established by heavy-ion test data.

SEUs and SETs in memory or logic domains should be mitigated by a layered approach combining EDAC, periodic memory scrubbing and architectural redundancy such as triple modular redundancy (TMR) in critical control loops. SET signature analysis, pulse duration, amplitude and frequency, must be carried out under representative test conditions, as ARCap relies heavily on analog front-ends where transient filtering is paramount. Systems must be tolerant to the broad range of SET pulse widths, which, for op-amps, can span up to 200  $\mu$ s, necessitating robust analog filtering strategies.

Moreover, functional interrupts (SEFI) triggered by SEEs in complex devices like FPGAs or ADCs must be countered through hardware and firmware watchdogs that can autonomously reinitialize subsystems without ground intervention. For deterministic control cycles in proximity operations, these recovery times must fall within strict latency envelopes.

SEECA underscores the importance of understanding the complete system context. For instance, a functional reset in the robotics controller during a quiescent phase might be acceptable, while the same event during capture would violate availability constraints. Therefore, SEE rate predictions must be phase-specific and weighted by operational criticality, a task that simulation tools like CREME and SPENVIS can facilitate, provided the input Weibull parameters accurately reflect tested part behavior under representative LET spectra.

Proton and neutron-induced SEEs require particular caution due to their complex interaction mechanisms and the limitations of LET-based extrapolations. For devices with LET thresholds below 15 MeV $\cdot$ cm<sup>2</sup>/mg, proton testing or simulation becomes essential, especially in high-Z process nodes where secondary particle generation can mimic heavy-ion effects. When test data are unavailable, a conservative radiation design margin (RDM) of 10 $\times$  should be applied, particularly if extrapolated from heavy-ion-only datasets.

To complete the assurance framework, a full SEECA process must include



mapping of subsystem functions to radiation environment phases, classification of each function’s SEE sensitivity and criticality, definition of validation methods including heavy-ion and proton testing plans, documentation of SEE mitigations and fallback logic per criticality tier and incorporation of SEECA outcomes into the broader system FMECA and requirements verification matrix.

NASA’s experience, as summarized in SEECA, also highlights the importance of documenting assumptions and test limitations. For COTS components, testing constraints like limited die access, variability across packaging revisions and unknown process changes must be explicitly captured. Any use of archival data must include traceability to lot number, process node and testing parameters, ideally verified via destructive physical analysis (DPA) or reverse engineering when high criticality is involved.

In conclusion, applying the SEECA methodology to ARCap provides a structured, risk-informed framework that enables the safe use of COTS in a 5-year LEO mission. The approach prioritizes critical functions, integrates component- and system-level mitigation, leverages both empirical and modeled data and supports a lifecycle-driven verification process. While technical uncertainties remain inherent in radiation effects prediction, particularly for commercial technologies not characterized for space, the disciplined use of SEECA allows mission designers to balance affordability, time constraints and mission reliability in a manner consistent with best practices in the aerospace industry.

### **Example: SEU Rate Budget for the Robotic Arm Controllers**

Building on the methodology and criticality mapping described above, a quantitative assessment was conducted to determine the acceptable Single Event Upset (SEU) rate for the digital controllers of the robotic arms in the ARCap module. These controllers are responsible for operating BLDC motors with encoder feedback and are a central component of the proximity operation and capture logic. Given their role in real-time control, even temporary disruptions due to SEUs could compromise mission phases that are safety- or availability-critical.

The analysis focused on a specific operational scenario in which the service satellite slowly approaches a target with a linear velocity of  $v = 1$  cm/s, beginning from a deployment distance of  $d = 15$  to  $20$  m, distance in which the control of robotic arms is active. This conservative speed selection was intentional: the low approach velocity maximizes the time window in which the arm is active and exposed to potential upsets, thereby constructing a worst-case condition. For instance, a  $20$  m approach at  $1$  cm/s results in an active duration of:

$$\Delta t = \frac{2000 \text{ cm}}{1 \text{ cm/s}} = 2000 \text{ s} \approx 33 \text{ minutes}$$

This time window serves as the basis for determining the maximum allowable SEU rate, under the constraint that no upsets should occur with a specified confidence level.

The assumption that Single Event Upsets (SEUs) follow a Poisson process is well supported in the space radiation effects community. SEUs are discrete, independent events caused by individual high-energy particles and their occurrence in time or particle fluence is stochastic and memoryless. Therefore, the number of SEUs observed in a given time or under a given fluence can be modeled using the Poisson distribution:

$$P(k) = \frac{\lambda^k e^{-\lambda}}{k!}$$

where  $\lambda$  represents the expected number of SEUs and  $k$  is the observed number of events. This probabilistic model is consistently applied in radiation hardness assurance literature. For instance, the SEECA framework published by NASA explicitly models SEE occurrences using a Poisson process and explains that the mean time between failures (MTBF) corresponds to a 63% cumulative probability of experiencing at least one event [28]. Similarly, [53] adopt Poisson statistics when computing SEU probabilities and estimating upper bounds for rare-event environments. Finally, system-level testing procedures for radiation hardness assurance also rely on Poisson-based confidence intervals for the extraction of cross-sections from empirical SEE data [52].

These references collectively validate the use of the Poisson distribution as a robust and widely accepted method for estimating SEU rates in the context of spaceborne electronics exposed to radiation.

To ensure that no SEUs ( $k = 0$ ) occur within the 33-minute window with 99% probability, the following inequality must hold:

$$P(0) = e^{-\lambda} \geq 0.99 \Rightarrow \lambda \leq -\ln(0.99) \approx 0.01005 \text{ events/33 min}$$

For a more conservative constraint, with 99.9% confidence, the acceptable rate becomes:

$$\lambda \leq -\ln(0.999) \approx 0.001 \text{ events/33 min}$$

To translate these values into a daily rate for comparison with system-level reliability requirements, the number of 33-minute windows in a day (1440 minutes) is calculated:

$$\frac{1440 \text{ min/day}}{33 \text{ min}} \approx 43.64 \text{ intervals/day}$$

Thus, the expected number of SEUs per day is:

$$\text{If } \lambda = 0.01 \Rightarrow \text{SEU/day} \approx 0.01 \times 43.64 = 0.436$$

$$\text{If } \lambda = 0.001 \Rightarrow \text{SEU/day} \approx 0.001 \times 43.64 = 0.0436$$

This analytical framework enables direct comparison with estimated SEU rates derived from radiation environment models and component cross-sections, allowing for system-specific constraints to be integrated into the design process. Components predicted to exceed these rates in LEO must be addressed via one or more mitigation strategies: bit-level redundancy, voting logic, watchdog resets or hardened part selection. This example demonstrates how SEECA and Poisson-based probabilistic analysis can be applied to practical mission operations to derive quantitative SEE tolerance budgets for critical subsystems like the robotic arm controllers in ARCap. The conservative selection of a low approach speed (1 cm/s) and correspondingly long operational exposure window ensures that the SEU requirement reflects a worst-case, yet plausible, mission scenario. To satisfy the system-level requirement of limiting the SEU rate to no more than 0.4 event per day with 99% confidence level for the deployment-capture phase, several actions must be undertaken at both the architectural and component level. First, at the requirements definition phase, the mission shall impose quantitative SEE rate thresholds on critical subsystems as part of the overall fault tolerance and availability budget. These requirements must flow down into lower-level design constraints, including maximum allowable SEU cross-section values for digital devices and maximum acceptable LET thresholds for candidate components.

At the component selection and screening stage, COTS parts must either be supported by existing SEE test data consistent with mission environments or be subjected to targeted heavy-ion and proton testing to characterize their upset behavior. Components that exceed the defined rate limits must be excluded, derated or protected using architectural mitigation techniques such as redundancy, voting logic or watchdog resets. Preference should be given to devices with low cross-sections, high LET thresholds or documented flight heritage.

Ultimately, achieving the system-level SEU tolerance objective requires an integrated assurance approach involving system-level reliability allocation, component-level screening and qualification and design-level mitigation strategies. The results of this analysis confirm that the selected controller architecture satisfies these criteria within the defined probability margin, thereby ensuring compliance with mission reliability expectations during critical operations

## Chapter 11

# Design-Centered Radiation Hardness Assurance Strategy

### 11.1 Radiation-Tolerant Design Flow Embedded in Conceptual Design

The methodology presented here draws its foundations from the strategy developed at CERN [54], [55] and [56] for the design of the radiation-tolerant embedded computers called Function Generator/Controllers (FGCs), directly installed in the power converter within the Large Hadron Collider (LHC) tunnel. The LHC environment, although terrestrial, exhibits radiation characteristics, high-energy hadron flux, long-term dose accumulation and SEE exposure, that are in many respects analogous to those encountered in space systems. Notably, these systems are also based on Commercial-Off-The-Shelf (COTS) components and demand high operational reliability.

The design flow adopted by CERN, ranging from specification through industrialization and installation, was developed to prevent radiation-induced failures that could compromise mission availability. This same principle is directly transferable to the development of spacecraft subsystems like the ARCap sensor suite. In this context, the CERN-derived RHA strategy was applied, not to a collider infrastructure, but to the qualification and prototyping of a spaceborne X-band radar on its path toward a flight-ready engineering model.

### **11.1.1 Designing to Preserve the Conceptual Architecture**

In space missions, the cost of post-design changes is extraordinarily high. A non-compliant component detected late in the process often leads to:

- Procurement of replacement components with long lead times;
- Architectural redesigns, impacting performance and interfaces;
- Recalculation of power, thermal and structural constraints;
- System requalification and extended program delays.

Therefore, in ARCap, radiation-aware design choices were embedded into the conceptual phase. The Bill of Materials (BoM) is formed using components with proven flight heritage in LEO or predictable behavior based on authoritative radiation databases (ESA, NASA). This ensures that early prototypes already reflect a realistic system and do not require disruptive redesign once tested.

### **11.1.2 C0/C1/C2 Classification: A Guiding Framework**

To implement this approach, the component classification system established at CERN [54], [55] and [56] was adopted:

- **C0**: components generally resistant to radiation with low criticality and easily replaceable in the design.
- **C1**: potentially susceptible components not on the critical path.
- **C2**: radiation-sensitive components integral to system functionality. These require comprehensive testing, including also proton and heavy ion campaigns.

The classification is based on three key criteria:

- a) Known susceptibility to radiation;
- b) Located in a design critical position for the proper functioning of the overall system.;
- c) Availability of commercial alternatives.

This structure allows prioritization of test resources and ensures that the failure of a C2 component never occurs during late-stage testing, which would mandate a full conceptual redesign.

### **11.1.3 Radiation Testing as a Filter, Not a Detonator**

Type testing is not used to discover flaws, it is used to confirm assumptions. In the ARCap development flow:

- C2 components are type-tested and validated early;
- C1 components are tested where needed with a built-in margin of safety (e.g., energy scaling, SEE cross-section conservatism);
- C0 components are monitored statistically or tested at board level.

In the case where a lot non-conformity is discovered, alternate pre-validated parts or technologies must be available. This flexibility must be planned from the beginning to ensure uninterrupted progress.

### **11.1.4 Lessons from CERN's Radiation-Tolerant Developments**

The design flow followed by the FGClite project illustrates the consequences of integrating RHA from the start. Components were selected with risk classification, tested in parallel with design and characterized using a mix of mixed-field, proton and heavy-ion facilities. Importantly, lot acceptance testing and early prioritization of high-risk components (C2) prevented the need to backtrack once integration began.

This methodology aligns with ECSS-Q-ST-60-15C [4] and [30] and provides a realistic roadmap for implementing space-grade reliability using mostly COTS.

## **11.2 Risk Assessment of Radar Front-End Components**

As part of the development of the X-band radar system for far-range operations, particular attention has been given to the qualification of components against radiation effects. In the antenna design phase, the methodology introduced in the previous section was adopted to ensure that the system architecture accounts for the risks associated with the space radiation environment. This risk-aware design approach enables the identification of critical components early in the development process and supports the implementation of appropriate mitigation strategies to meet reliability requirements throughout the mission duration.

The risk assessment of the radar front-end system involves a multi-layered analysis that integrates both functional and design-based criticality levels. The classification of components into categories C0, C1 and C2 provides a structural

basis for understanding each component's integration level within the system. Simultaneously, the risk levels R0, R1 and R2 classify the consequences of component failures in terms of operational impact during the mission.

### 11.2.1 Risk Assessment Methodology: DC, FC and RDM

The proposed risk methodology is structured around the definition of risk as the product of **probability** and **impact**.

- **Design Criticality (DC)** quantifies the likelihood (C0, C1, C2) that a component will fail qualification testing due to insufficient radiation tolerance. It reflects the component's position within the system, so the consequences of a test failure on the design architecture and the inherent susceptibility of the component to the radiation effects. The C0 index means low design criticality.
- **Functional Criticality (FC)** quantifies the impact (R0, R1, R2) of an in-orbit failure, i.e., the operational consequence of a malfunction during the mission. The R0 index means low functional criticality.

The evaluation process begins by identifying the **component family**, leveraging supplier databases, published test reports, previous flight heritage or performing preliminary tests to estimate baseline radiation tolerance and characterization to radiation effects. Based on this and component function, DC and FC are assigned.

Components with high DC are tightly coupled to the architecture and their failure may compromise or require redesign of the system.

To mitigate the risk associated with qualification failure, a **Radiation Design Margin (RDM)** is applied. RDM is used to ensure that the tested radiation tolerance of a component, defined as  $S = \text{RDM} \times L$ , exceeds the expected mission dose  $L$ .

According to this approach, mitigation begins already at the conceptual design phase. For components with high Design Criticality (DC), either because they occupy a critical architectural path or because they are intrinsically sensitive to radiation, it is required flight-proven components or, at minimum, well-documented radiation tolerance from the supplier. If the component is a COTS part, particularly from the automotive domain, early radiation testing is essential. This ensures that you will not encounter failures or requalification needs during later phases, when architectural modifications are much more costly or infeasible.

In this framework, DC depends on two aspects: the component's sensitivity to radiation and its role in the design. Highly sensitive components may require dose mitigation strategies (e.g., shielding), while components central to the system's architecture must be selected and tested with confidence early in the design.

Waiting to characterize such components late in the development cycle introduces unacceptable risk.

A successful qualification test, conducted early, allows to quantify the radiation tolerance and define the associated RDM as the margin between the qualified level and the simulated end-of-life dose. Adjusting the RDM effectively reduces the component's DC by lowering the likelihood of failure, either through dose reduction or through the selection of a more tolerant component. In this way, the RDM becomes a key lever for risk reduction, guiding both component selection and the system architecture definition, quantifying the required mitigation.

This approach sees:

- **High DC Components (C2):** these components are both highly susceptible to radiation and occupy critical positions in the system. Treating their DC as a high probability of failure ensures sufficient resources are allocated (e.g., higher RDM, rigorous testing).
- **Medium DC Components (C1):** moderately susceptible components in less critical positions. Their medium failure probability requires balanced mitigation, like moderate RDM and standard testing.
- **Low DC Components (C0):** inherently radiation-tolerant and non-critical components. They need minimal mitigation.

By linking DC to probability, you will ensure that the design process explicitly considers the risk associated with each component. This allows to:

- Focus resources on critical components: high DC components receive focused attention.
- Apply appropriate RDM: ensuring critical components have adequate safety margins.
- Freeze the design with confidence: increasing the RDM reduces overall risk by lowering the probability of failure. This can be achieved either by decreasing the radiation threat (e.g., adding shielding) or by selecting components with greater intrinsic tolerance. In both cases, risk is mitigated because the component is better able to survive the expected environment and qualification success becomes more likely only if the susceptibility of the component is proven.

However, applying a high RDM without knowledge of actual radiation tolerance may be ineffective: if the component lacks heritage or is poorly characterized, it may still fail qualification. This is particularly critical for high-DC components. Therefore, the selection process must favor components with **proven flight heritage** or well-established radiation data or, in addition, if these data are unavailable



it is recommended to perform initial tests on COTS components to characterize their electrical performance and susceptibility under specified radiation condition. This ensures the design remains stable through qualification and avoids late-stage architectural redesign.

**Key Insight:** *The purpose of the RDM is to reduce the likelihood of component failure, by enhancing component tolerance above the expected threat level and mitigating through the careful selection of components with proven flight heritage compatible with the mission's environmental and functional requirements. These requirements are defined at the system design level, where, based on the estimated end-of-life radiation dose, an appropriate RDM is applied according to the component's criticality in the overall architecture.*

**Application of the Risk-Driven Flow** This methodology ensures that both design-phase criticality and mission-phase criticality are systematically addressed. It reinforces the importance of early selection of radiation-tolerant components, especially those in high-DC positions, with sufficient margin and pedigree to guarantee mission success without compromising system architecture. For example, a beamformer (C2) is critical both in terms of design, its failure during qualification testing would require a complete redesign and function, its failure during the mission would disrupt the radar's beamforming capability. Similarly, a decoupling capacitor (C0) is non-critical in both design (easily replaceable) and function (its failure has minimal impact on system performance). This alignment between design and functional criticality allows to use DC as a proxy for the probability of failure, as critical components are more likely to cause system-level issues if they fail.

Each component belongs to a specific family (e.g., MOSFETs, operational amplifiers, resistors) and each family has a characteristic level of radiation tolerance. For example, MOSFETs are generally more susceptible to Single Event Effects (SEE) than ceramic capacitors. This susceptibility is a fixed attribute of the component family and directly influences the likelihood of failure.

Based on susceptibility and component position in the design, three classes (C0, C1, C2) are defined, that correspond to different levels of testing required to meet the system's radiation specifications. The purpose of these tests, in the early phase of design, is to freeze the component selection and ensure robustness against radiation-induced failures during testing campaigns and mission.

Once components that satisfy the radiation requirements are selected, the design is effectively frozen. In this way, by interpreting DC as the probability of failure, linked to inherent radiation tolerance and criticality in the design, and FC as the consequence of mission failure, this framework aligns component selection, qualification and mitigation strategies with actual risk. Critical components receive enhanced scrutiny and margin; heritage and testing reduce uncertainty; and the system is designed to be robust, maintainable and radiation-thought by construction.

In Table 11.1, a set of representative components forming the radar antenna and its associated power and control circuitry are listed along with their assigned Functional and Design Criticality levels. This classification serves as a guiding framework for the electrical and RF design of the antenna, while simultaneously informing the radiation qualification strategy.

Component	Subfamily	Family	DC	FC	Risk Analysis and Mitigation
MOSFET P-CH 60V 3A/8A	MOSFET P-CH	Power Devices	C1	R2	Critical for power management and RF switch control. Sensitive to radiation but easily replaceable without structural impacts.
MOSFET 2-NCH 60V 0.115A	MOSFET N-CH	Power Devices	C1	R2	Essential for RF signal switching. High sensitivity to SEE, mitigated by circuit-level redundancy.
IC GATE DRVR LOW-SIDE	Gate Driver	Control Circuits	C1	R1	Drives MOSFETs. Failure impacts system functionality but is easily replaceable.
IC OP AMP GP 2 CIRCUIT	Operational Amplifier	Analog Circuits	C0	R1	Supports signal management with limited risk due to high tolerance components.
IC SWITCH SPDT	Analog Switch	Control Circuits	C1	R1	Controls RF signal routing. Radiation-sensitive but easily replaced.
CAP CER 10UF 50V X7S	Ceramic Capacitor	Passive Components	C0	R1	Low criticality. Easily replaced with equivalent parts.
RES SMD 220K OHM	SMD Resistor	Passive Components	C0	R0	Minimal risk due to low criticality.
DIODE STANDARD 75V 500MA	Protection Diode	Electrical Protection	C0	R1	Protects from over-voltage. Failure affects protection, but design is unchanged.
RF FRONT-END MODULE	RF Module	RF Front-end	C2	R2	High-criticality module. Failure necessitates redesign and severely impacts radar function.
QUAD BEAM-FORMER	Beamforming	RF Front-end	C2	R2	Critical for radar directionality. Highly sensitive to SEE; redundancy recommended.

**Table 11.1:** Component Classification with Design & Functional Criticality

# Conclusion

This thesis has presented the full conceptualization, design evolution and qualification strategy of the ARCap sensor suite, a space-oriented payload aimed at enabling advanced on-orbit servicing through precision sensing and autonomy. ARCap includes complex subsystems such as X-band radar, W-band radar, LiDAR, stereo vision and robotic manipulators, all of which must operate reliably in the challenging radiation environment of Low Earth Orbit (LEO).

Initially, the project aimed at achieving universal radiation compliance across all orbital regimes by constructing a synthetic worst-case environment. However, this approach proved technically and economically unfeasible for a startup context due to the constraints of COTS components and mass/power budgets. The strategy was thus refocused to support a 5-year LEO mission, representative of the most commercially viable application segment, where radiation effects are significant but manageable.

From here, a tailored radiation hardness assurance (RHA) plan was developed. Key contributors to this process included modeling tools like OMERE and SPEN-VIS for dose prediction and industry standards (MIL, ESA, ECSS) for defining acceptable qualification thresholds. Particular attention was placed on Total Ionizing Dose (TID), which was established as the primary driver for component screening. TID limits were derived with appropriate Radiation Design Margins (RDM) and a structured decision matrix was defined based on the TID resilience of each candidate component.

The thesis further explored practical radiation test strategies, including Co-60 gamma sources, proton accelerators and high-energy filtered X-ray generators, each chosen based on the testing depth, penetration and relevance to the operational environment. An emphasis was placed on high-fidelity component screening using real-world flight data and SEE characterization techniques.

The most critical contribution of this work lies in the architectural integration of radiation tolerance. Drawing directly from CERN's FGClite methodology, a class-based risk framework (C0/C1/C2) was adopted to guide component selection and testing. This system balances the need for reliability with design flexibility and is compatible with ECSS-Q-ST-60-15C guidance.

The core principle behind ARCap's development flow is that Radiation Hardness Assurance must be co-designed with the architecture. When C2 components fail late, it is not a technical error, it is a system failure. Therefore, all radiation constraints, mitigation strategies and test validations are introduced from the earliest conceptual phase.

By grounding design choices in proven component behavior and structured classification, ARCap achieves a practical path toward a radiation-tolerant engineering model, without undermining performance or introducing disruptive redesign cycles. Radiation resilience is not retrofitted. It is designed in.



# Bibliography

- [1] European Cooperation for Space Standardization, *ECSS-E-ST-10-12C Rev.1: Space engineering – Methods for the calculation of radiation received and its effects and a policy for design margins*, ESA-ESTEC, 15 November 2008, with Corrigendum 1 (22 February 2017).
- [2] European Cooperation for Space Standardization, *ECSS-E-HB-10-12A: Space engineering – Radiation received and its effects and margin policy handbook*, ESA-ESTEC, 17 December 2010.
- [3] European Cooperation for Space Standardization, *ECSS-E-ST-10-04C: Space engineering – Space environment*, ESA-ESTEC, 15 November 2008.
- [4] European Cooperation for Space Standardization, *ECSS-Q-ST-60-15C: Space product assurance – Radiation hardness assurance – EEE components*, ESA-ESTEC, 1 October 2012.
- [5] J. Guild, B. P. Decosse, D. Flanigan, J. Mazur, C. Stauffer and J. Petrovic, *Best Practices for Development of Radiation Analysis for Space Systems*, Aerospace Corporation, Technical Report TOR-2022-00016, Dec. 31, 2021.
- [6] Texas Instruments, *Radiation Handbook for Electronics for Space Applications*, Application Report SLVAE85, October 2022.
- [7] TRAD Tests & Radiations, *OMERE: Radiation Environment and Effects Engineering Tool*, TRAD, 2023. Freeware developed with CNES support. Available: <https://www.trad.fr/en/space/omere-software/>
- [8] European Space Agency (ESA), *SPENVIS User Manual*, ESA, 2022. Accessed: 2025-06-04. Available: <https://www.spenvis.oma.be/help/system/toc.html>
- [9] A. C. Tribble, *The Space Environment: Implications for Spacecraft Design – Revised and Expanded Edition*, Princeton University Press, 2003.
- [10] M. Xapsos, T. Jordan and E. Stassinopoulos, *The Radiation Environment for the Next Generation Space Telescope*, NASA Goddard Space Flight Center, Technical Report GSFC-RPT-2000-0002, 2000.
- [11] V. U. J. Nwankwo, N. N. Jibiri and M. T. Kio, *The Impact of Space Radiation Environment on Satellites Operation in Near-Earth Space*, in *Ionospheric and Atmospheric Threats for GNSS and Satellite Telecommunications*, IntechOpen, June 2020.

- [12] V. A. Pinto, P. O'Brien, D. N. Baker and I. R. Mann, *Characteristics and occurrence patterns of the transient third radiation belt*, Geophysical Research Letters, vol. 45, no. 23, Dec. 2018.
- [13] Y. Hao, Q. Schiller, M. G. Henderson, J. R. Wygant and C. A. Kletzing, *A short-lived three-belt structure for the outer radiation belt electrons*, Journal of Geophysical Research: Space Physics, vol. 125, no. 4, Apr. 2020.
- [14] D. N. Baker, *Wave-particle interaction effects in the Van Allen belts*, Earth, Planets and Space, vol. 73, no. 189, 2021.
- [15] L. Olifer, I. R. Mann, S. G. Claudepierre, D. N. Baker, H. E. Spence and L. G. Ozeke, *A natural limit to the spectral hardness of worst case electron radiation in the terrestrial Van Allen belt*, Journal of Geophysical Research: Space Physics, vol. 127, no. 8, e2022JA030506, 2022.
- [16] Y. Mei, Y. Ge, A. Du, X. Gu, D. Summers, X. Li, S. Fu and Z. Xiang, *Energy-dependent boundaries of Earth's radiation belt electron slot region*, The Astrophysical Journal, vol. 922, no. 246, Dec. 2021.
- [17] S. A. Saikin, D. N. Baker, H. Zhao, M. G. Henderson, R. M. Skoug, R. J. Redmon and D. J. McComas, *Reconstruction of the Radiation Belt Content During Solar Cycle 24 Using a Multi-Source Data Assimilation Approach*, Space Weather, vol. 19, no. 10, e2021SW002792, Oct. 2021.
- [18] X. Shi, J. Ren and Q. G. Zong, *The dynamics of the inner boundary of the outer radiation belt during geomagnetic storms*, Journal of Geophysical Research: Space Physics, vol. 125, no. 5, e2019JA027309, 2020.
- [19] Y. Miyoshi, K. Miyamoto, T. Obara and A. Morioka, *Long-term modulation of proton fluxes in the inner radiation belt observed by the Akebono satellite*, Journal of Atmospheric and Solar-Terrestrial Physics, vol. 62, no. 11, pp. 873–880, 2000.
- [20] N. Tomassetti, A. Oliva, R. Battiston and E. Fiandrini, *Evidence for a time lag in solar modulation of galactic cosmic rays*, Advances in Space Research, vol. 60, no. 4, pp. 815–825, 2017.
- [21] W. N. Spjeldvik and T. A. Fritz, *Energetic particle pitch angle distributions and lifetimes in the radiation belts: CRAND and diffuse loss*, Journal of Geophysical Research: Space Physics, vol. 83, 1978.
- [22] D. L. Turner, Y. Shprits, M. Hartinger and V. Angelopoulos, *Explaining sudden losses of outer radiation belt electrons during geomagnetic storms*, Nature Physics, vol. 8, 2012.
- [23] M. S. Gussenhoven, E. G. Mullen and D. H. Brautigam, *Improved Understanding of the Earth's Radiation Belts from the CRRES Satellite*, IEEE Transactions on Nuclear Science, vol. 43, pp. 353–368, 1996.
- [24] NOAA Space Weather Prediction Center (SWPC), *Solar Cycle Progression*, National Oceanic and Atmospheric Administration. Available at: <https://www.swpc.noaa.gov/products/solar-cycle-progression>.
- [25] M. P. Petrucci, C. Testa and A. Nascetti, *Advances in Polymeric Materials*



for *Radiation Shielding in Aerospace Applications*, Polymers, vol. 16, no. 3, Art. 382, 2024.

[26] C. L. Fan, C. R. Drumm, S. B. Raskey and G. J. Scrivner, *Shielding Considerations for Satellite Microelectronics*, IEEE Transactions on Nuclear Science, vol. 43, no. 6, pp. 2790–2795, Dec. 1996.

[27] A. Emmanuel, J. Raghavan, R. Harris and P. Ferguson, *A comparison of radiation shielding effectiveness of materials for highly elliptical orbits*, Advances in Space Research, vol. 53, no. 7, pp. 1143–1152, 2014.

[28] R. F. Hodson, J. A. Pellish, R. A. Austin, M. J. Campola, R. L. Ladbury, K. A. LaBel, G. R. Allen, R. Gaza and E. M. Willis, *Avionics Radiation Hardness Assurance (RHA) Guidelines*, NASA Technical Memorandum NASA/TM–20210018053, NESC-RP-19-01489, July 2021.

[29] K. A. LaBel, A. H. Johnston, J. L. Barth, R. A. Reed and C. E. Barnes, *Emerging radiation hardness assurance (RHA) issues: A NASA approach for space flight programs*, IEEE Transactions on Nuclear Science, vol. 46, no. 6, pp. 1697–1703, 1999.

[30] European Cooperation for Space Standardization (ECSS), *ECSS-Q-ST-60-15C Rev.1: Radiation Hardness Assurance – EEE Components*, ESA Requirements and Standards Division, March 2025.

[31] F. Lei, P. R. Truscott, C. S. Dyer, B. Quaghebeur, D. Heynderickx, P. Nieminen, H. Evans and E. Daly, *MULASSIS: A Geant4-based Multilayered Shielding Simulation Tool*, IEEE Transactions on Nuclear Science, vol. 49, no. 6, pp. 2788–2793, Dec. 2002.

[32] P. R. Truscott, F. Lei, C. S. Dyer, B. Quaghebeur, D. Heynderickx, P. Nieminen, H. Evans, E. Daly, A. Mohammadzadeh and G. Hopkinson, *MULASSIS – Monte Carlo Radiation Shielding Simulation for Space Applications Made Easy*, ESA TRP Report, QinetiQ and Belgian Institute for Space Aeronomy, 2003.

[33] Texas Instruments, *Official Website*, Available at: <https://www.ti.com/>

[34] D. Sinclair and J. Dyer, *Radiation Effects and COTS Parts in SmallSats*, Proc. of the 27th Annual AIAA/USU Conference on Small Satellites, SSC13-IV-3, 2013.

[35] Texas Instruments, *Radiation-hardened and radiation-tolerant products to help innovate your space designs*, SLYT532G and SLYT532J, Revisions G and J, 2022–2024. Available at: <https://www.ti.com/lit/an/slyt532g/slyt532g.pdf> and <https://www.ti.com/lit/an/slyt532j/slyt532j.pdf>

[36] Texas Instruments, *Beyond Quality – Assuring the Reliability of Plastic Encapsulated Integrated Circuits*, SBOA144A, Rev. A, July 2020. Available at: <https://www.ti.com/lit/an/sboa144a/sboa144a.pdf>

[37] Texas Instruments, *Reduce the Risk in Low-Earth Orbit Missions with Space Enhanced Plastic Products*, SBOA344A, Rev. A, November 2021. Available at: <https://www.ti.com/lit/an/sboa344a/sboa344a.pdf>

- [38] GSFC Radiation Data Base, *Radiation Effects Database*, Available at: <https://nepp.nasa.gov/radhome/RadDatabase/RadDataBase.html>
- [39] European Space Agency (ESA), *ESCC QPL: Qualified Parts List*, ESCIES Database. Available at: <https://escies.org/webdocument/showArticle?id=228&groupid=6>.
- [40] CERN – Radiation to Electronics (R2E) Project, *Radiation Testing*, Available at: <https://r2e.web.cern.ch/about-radiation/radiation-testing>.
- [41] *DoEEEt – Radiation and EEE Parts Database Platform*, Available at: <https://www.doeet.com/>.
- [42] A. Akkerman, J. Barak, M.B. Chadwick, J. Levinson, M. Murata and Y. Lifshitz, *Updated NIEL calculations for estimating the damage induced by particles and gamma-rays in Si and GaAs*, Radiation Physics and Chemistry, vol. 62, no. 4, pp. 301–310, 2001.
- [43] C. J. Dale, P. W. Marshall, B. Cummings, L. Shamey and A. Holland, *Displacement Damage Effects in Mixed Particle Environments for Shielded Spacecraft CCDs*, IEEE Transactions on Nuclear Science, vol. 40, no. 6, pp. 1628–1637, Dec. 1993.
- [44] I. Jun, M. A. Xapsos, S. R. Messenger, E. A. Burke, R. J. Walters, G. P. Summers and T. Jordan, *Proton Nonionizing Energy Loss (NIEL) for Device Applications*, IEEE Transactions on Nuclear Science, vol. 50, no. 6, pp. 1924–1928, Dec. 2003.
- [45] Y. Quadros de Aguiar, F. Wrobel, J.L. Autran, R. G. Alía, *Single-Event Effects, from Space to Accelerator Environments*, Springer, 2024.
- [46] F. Bezerra, *Radiation Test Standards for Space*, RADSAGA Training Workshop, CNES – Centre National d’Études Spatiales, Toulouse, France, March 2018.
- [47] European Space Agency (ESA), *ESCC Basic Specification No. 22900 – Total Dose Steady-State Irradiation Test Method*, Issue 5, June 2016.
- [48] Ó. Gutiérrez, M. Prieto, A. Sanchez-Reyes, Á. Perales-Eceiza, A. Ravanbakhsh, D. Guzmán, A. Gómez and G. Pennestri, *Electronic components TID radiation qualification for space applications using LINACs. Comparative analysis with <sup>60</sup>Co standard procedure*, Advances in Space Research, vol. 69, no. 11, pp. 4376–4390, 2022.
- [49] V. Girones, J. Boch, A. Carapelle, A. Chapon, T. Maraine, T. Labau, F. Saigné, Rubén García Alía, *The Use of High-Energy X-Ray Generators for TID Testing of Electronic Devices*, IEEE Transactions on Nuclear Science, vol. 69, no. 9, pp. 2217–2225, 2022.
- [50] J. Pritts, *Basic Mechanisms: Total Ionizing Dose*, LANL Radiation Effects Summer School, Los Alamos National Laboratory, LA-UR-19-25172, June 2019.
- [51] K. A. LaBel, *Radiation Requirements and Requirements Flowdown: Single Event Effects (SEEs) and Requirements*, presented at the HEART Short Course, Albuquerque, NM, March 12, 2003. NASA Goddard Space Flight Center.

- [52] A. Coronetti, R. García Alía, J. Budroweit, T. Rajkowski, I. Da Costa Lopes, K. Niskanen, D. Söderström, C. Cazzaniga, R. Ferraro, S. Danzeca, J. Mekki, F. Manni, D. Dangla, C. Virmontois, N. Kerboub, A. Koelpin, F. Saigné, P. Wang, V. Pouget, A. Touboul, A. Javanainen, H. Kettunen and R. Coq Germanicus, *Radiation Hardness Assurance Through System-Level Testing: Risk Acceptance, Facility Requirements, Test Methodology and Data Exploitation*, IEEE Transactions on Nuclear Science, vol. 68, no. 5, pp. 958–969, 2021.
- [53] C. Poivey, *Radiation Hardness Assurance for Space Systems*, Short Course Notes, IEEE Nuclear and Space Radiation Effects Conference (NSREC), Phoenix, AZ, July 2002. SGT Inc., NASA Goddard Space Flight Center.
- [54] B. Todd and S. Uznanski, *Radiation Risks and Mitigation in Electronic Systems*, in Proceedings of the CAS-CERN Accelerator School: Power Converters, Baden, Switzerland, 7–14 May 2014, edited by R. Bailey, CERN-2015-003, pp. 245–263, CERN, Geneva, 2015.
- [55] B. Todd, A. Dinius, Q. King and S. Uznanski, *Radiation tolerant power converter controls*, Journal of Instrumentation, vol. 7, no. 11, C11012, Nov. 2012.
- [57] S. Uznanski, B. Todd, A. Dinius, Q. King and M. Brugger, *Radiation Hardness Assurance Methodology of Radiation Tolerant Power Converter Controls for Large Hadron Collider*, IEEE Transactions on Nuclear Science, vol. 61, no. 6, pp. 3694–3700, Dec. 2014.